Pressure and Flow Wave Propagation in Patient-Specific Models of the Arterial Tree

THÈSE N^{O} 5029 (2011)

PRÉSENTÉE LE 10 JUIN 2011

À LA FACULTÉ SCIENCES DE LA VIE
LABORATOIRE D'HÉMODYNAMIQUE ET DE TECHNOLOGIE CARDIOVASCULAIRE (SV/STI)
PROGRAMME DOCTORAL EN BIOTECHNOLOGIE ET GÉNIE BIOLOGIQUE

ÉCOLE POLYTECHNIQUE FÉDÉRALE DE LAUSANNE

POUR L'OBTENTION DU GRADE DE DOCTEUR ÈS SCIENCES

PAR

Philippe REYMOND

acceptée sur proposition du jury:

Prof. M. Swartz, présidente du jury
Prof. N. Stergiopulos, directeur de thèse
Prof. J.-J. Meister, rapporteur
Prof. P. Segers, rapporteur
Prof. N. Westerhof, rapporteur

ÉCOLE POLYTECHNIQUE
FÉDÉRALE DE LAUSANNE
Suisse
2011

ACKNOWLEDGMENTS

This thesis would not have been possible without the help, support and friendship of my family, friends and colleagues.

Sincere thanks to Professor Nikos Stergiopulos, who gave me the opportunity to work in the cardiovascular field and to participate in many projects and collaboration with other groups in the academic and the clinical environments. He has always been closely involved in my thesis work, and I greatly appreciate his help, support and friendship.

I would like to warmly thank all of the former and present members of the Laboratory of Hemodynamic and Cardiovascular Technology (LHTC) who made the work place a friendly environment and who are now, more friends than colleagues:
to Luca Augsburger with whom we had a great collaboration, for his endless friendship; to Michel Bachmann with whom I shared the office during years for his endless good mood, kindness and all of the discussions we had; also to Stéphane Bigler for his kindness and all of the interesting technical discussions we had; to Rafaela Fernandes Da Silva for her kindness ; to Edouard Fonck who is always positive, nice and brought a great atmosphere to the lab; to Thiresia Giallourou for her kindness; to Veronica Gambillara for her kindness; to Bryn Martin who is always enthusiastic and motivated by new projects; to Vardoulis Orestis for his kindness; to Rana Saitta-Rezakhaniha who was always friendly and ready to help; to Sylvain Roy for his expertise in the clinical field and all of the discussions we had on different subjects and his friendly support; to Paolo Silacci for his kindness; to Tamina Sissoko for a her help; to Tyler Thacher for his endless friendship -- for always being so nice, ready to help and supportive and for all the nice moments we had; to Adan Villamarin for his good mood and friendship.

I began my PhD thesis under the EU project @neurIST and met many motivated scientists and medical doctors. I would like to thank Alberto Marzo at the Sheffield Hospital for this friendly collaboration.

Thanks also to the CMCS chair at EPFL, Paolo Crosetto, Simone Deparis and Alfio Quarteroni for their help and collaboration.

Many great collaborations in the clinical setting were possible during the project. To those who contributed, thank you. Special thanks go to Dr. Karim Bendjelid, Olivier Brina, Pascal Challande, Prof. Jean-Claude Chevrolet, Prof. Theodor Landis, Dr. François Lazeyras, Dr. Vittor Pereira, Dr. Fabienne Perren and Prof. Daniel Rüfenacht at the University Hospital of Geneva, all of whom gave me the chance to discover the clinical environment and freely shared with me their inestimable knowledge.

Sincere thanks to our friends in neighboring labs, to the Biomechanical Orthopedics Laboratory members, especially to Philippe Abdel-Sayed, Luc Blecha, Alireza Roshan Ghias, Miguel Gortchacow, Sandra Jaccoud, Xabier Larrea, Dominique Pioletti, Silvio Ramondetti, Patricia Scheuber, Alexandre Terrier and Arne Vogel; thanks also to Patrick Wenger, Pierre-Jean Wipff and Hicham Majd who were always enthusiastic, positive and friendly.

Further thanks to all of the students who did their master or semester project in the lab –Mustapha Al Kharfane, Thibo Billiet, Yvette Bohraus, Virginie Chenaux, Valentina Cortés-Gomez, Benjamin David, Anne-Lise Debeule, Reda Hasballa, Andreas Jauslin, David Petiot, Andreas Schmocker, and Sinan Ucak. It was great working with you all. Thank you for your work and your motivation.

Thanks also to the members of the Neuroscience Department at the University Medical Center (CMU) in Geneva for the warm welcome to their office, especially to Alessandra Adami, Tiziano Binzoni, Aurélien Bringuard, Guido Ferretti and Christian Moia.

I would like to warmly thank all the friends from EPFL and especially Joël Cugnoni, Thomas Gmür, Jean-Daniel Landis, Marco Matter, Thiéry Meyer and Arata Nakajo.

Most of all, I would like to thank my parents, my brother, my family and all of my friends, especially Isma, Guig and Nev, for their support and for the many nice times we have had over the past years.

Content

RÉSUMÉ

La circulation artérielle induit des forces hémodynamiques qui jouent un rôle important dans de nombreuses maladies vasculaires. La variation temporelle des contraintes de cisaillement pariétale semble jouer un rôle important dans le développement des plaques d'athérosclérose et de leur stabilité. Il a également été montré que les contraintes de cisaillement induites par le flux sanguin sont liées à la croissance et au risque de rupture éventuel des anévrismes cérébraux.
Les forces hémodynamiques sont intrinsèquement liées au patient et difficiles à estimer en clinique, à l'heure actuelle, et avec le niveau de précision requis. Cependant, les techniques d'imagerie utilisées fréquemment en clinique permettent de recréer la géométrie de vaisseaux sanguins de manière précise et peuvent donc servir à construire des modèles de la circulation. Ces derniers peuvent être utilisés pour comprendre la circulation dans les cas physiologiques et pathologiques et rendre donc cette approche intéressante.

Premièrement, nous avons développé un modèle 1-D générique de la circulation artérielle humaine, qui est constitué des principales artères systémiques et couplées à un modèle du cœur. Les équations de la mécanique des fluides sont résolues numériquement afin d'obtenir la pression et le flux sanguins à travers tout l'arbre artériel. Les parois artérielles sont modélisées avec une loi de comportement viscoélastique non linéaire alors que les vaisseaux distaux sont terminés avec un modèle de Windkessel à trois éléments. Les coronaires sont modélisés en faisant l'hypothèse que la résistance au débit sanguin lors de la systole est proportionnelle à l'élastance variable du ventricule cardiaque. Les prédictions du modèle sont validées avec des mesures non invasives de pression et de débit sanguins de jeunes volontaires. Le débit dans les grandes artères a été mesuré par imagerie par résonance magnétique alors qu'au niveau cérébral, il l'a été par Doppler transcranien et la pression au niveau des artères superficielles mesurée par tonométrie. La comparaison des prédictions du modèle avec les mesures de pression et débit en différents lieux anatomiques est bonne, ce modèle générique est donc capable de reproduire les courbes de pressions et débits d'un sujet moyen.

En suivant la même approche, nous avons construit et validé un modèle spécifique à une personne et dans ce cas, les données géométriques, le débit et la pression sanguine ont été obtenus pour la même personne. La comparaison des prédictions du modèle avec les mesures agrée toujours bien en termes de forme et de caractéristiques des ondes et de manière plus proche quantitativement que le modèle générique.

La sous-estimation des pertes énergétiques qui est inhérente au fait que le modèle 1-D de propagation des ondes ne tient pas compte des bifurcations réelles, des géométries non planaires et complexes a été étudiée. Le modèle 1-D a été comparé à une simulation 3-D CFD pour laquelle les propriétés rhéologiques Newtoniennes et non-Newtoniennes du sang ont été simulées et l'évolution de la pression le long des artères comparée entre les deux modèles. Les résultats montrent que la chute de pression moyenne n'est significative que dans les artères de faible diamètre comme les artères pré-cérébrales et cérébrales. En effet, dans ces derniers, la chute de pression est constamment sous-estimée par le modèle 1-D. Les écoulements complexes dus aux géométries asymétriques et aux bifurcations engendrent des contraintes de cisaillement plus élevées dans le modèle 3-D.

Une simulation d'interaction fluide-structure en 3-D et instationnaire a été menée dans un modèle spécifique d'un patient afin de saisir les détails d'un modèle 3-D et l'effet de la propagation d'ondes tel que saisit par le modèle 1-D. Cette approche 3-D est la plus complexe en termes de calculs et de mises en place, mais permet d'effectuer des simulations physiologiques avec un niveau élevé de détails et d'une grande précision. Par exemple, cette approche peut être pertinente afin d'obtenir l'écoulement sanguin dans des régions ou se développent des plaques d'athérosclérose ou des

anévrismes. Cette simulation à été appliquée à la circulation dans une aorte et des paramètres d'importance, comme la contrainte de cisaillement pariétale, ont été quantifiés. Des différences significatives ont été relevées, comparé au modèle 3-D pour lequel le lumen était considéré rigide ; ceci montre la l'intérêt de ce type d'approche. Les résultats du modèle 3-D à parois artérielles élastiques ont également été comparés au modèle 1-D équivalent, ils montrent une bonne corrélation en termes d'ondes de pression et de débit.

L'effet de la perte de compliance de l'arbre artériel sur les paramètres hémodynamiques a été étudié. La diminution de compliance locale au niveau de l'aorte proximale, et globale de l'arbre artériel a été modélisée. Ces deux cas engendrent une augmentation du « pulse pressure » au niveau central, cependant, les mécanismes sous-jacent sont différents. La diminution de la compliance au niveau local induit un accroissement de l'impédance caractéristique et de l'amplitude du pic systolique de l'onde de pression incidente, par contre une diminution globale de la compliance artérielle augmente l'amplitude et la vitesse des ondes de pression rétrogrades et une augmentation de la pression en fin de systole. Ces deux mécanismes qui ont été reportés dans la littérature, basés sur des données in vivo, ont probablement une contribution à l'accroissement de la pression systolique.

Ces modèles spécifiques pourront bientôt être utilisés dans un environnement clinique et être utiles pour des diagnostics et la planification d'un traitement.

MOTS-CLÉS

Propagation d'ondes de pression, hémodynamique, circulation cérébrale, modèle 1-D, techniques de mesure non invasives, IRM à contraste de phase, Doppler, modèle cardiaque, couplage ventriculaire artériel, viscoélasticité, CFD, FSI, sang Non-Newtonien, reconstruction images médicale.

SUMMARY

Blood flow in the arterial circulation induces hemodynamic forces that play an important role in various forms of vascular diseases. Temporal variation of the wall shear stress seems to play a significant role in atherogenesis and plaque stability. Flow induced wall shear stress has been linked to growth and possibly rupture of the aneurysm wall.
Hemodynamic forces are patient-specific and difficult to assess in the clinic. At present, there is no in vivo measurement technique that enables measurement of hemodynamic forces to the degree of precision needed. However, when imaging modalities used frequently in clinical routine re-create high-definition, patient geometric quantification of the blood vessel, they can be employed as a base for creating predictive hemodynamic models. Which in the case of understanding healthy vs. pathologic blood flow within the cerebral or systemic circulation, renders this an interesting approach.

First, we developed a "generic 1D" distributed model of the human arterial tree including the primary systemic arteries and coupled this to a heart model. The fluid mechanics equations were solved numerically to obtain pressure and flow throughout the arterial tree. A nonlinear viscoelastic constitutive law for the arterial wall was considered while distal vessels were terminated with a three-element Windkessel model. The coronary arteries were modeled assuming a systolic flow impediment proportional to ventricular varying elastance. The model predictions were validated with noninvasive measurements of pressure and flow performed in young volunteers. Flow in the large arteries was visualized with magnetic resonance imaging, cerebral flow detected with ultrasound Doppler and blood pressure measured with applanation tonometry. Model predictions at different arterial locations compared well to measured flow and pressure waves at the same anatomical points. Thus, the generic 1D model reflected the flow and pressure measurements of the "average subject" of our volunteer population.

Following the same approach as the generic 1D model, we built and validated a patient-specific model. In this case, geometric data, flow and pressure measurements were obtained for one person. The model predicted pressure and flow waveforms in good agreement with the in-vivo measurements with regards to wave shape and features. Comparison with a generic 1-D model has shown that the patient-specific model better predicted pressure and flow at specific arterial sites. Overall, the patient-specific 1-D model was able to predict pressure and flow waveforms in the main systemic circulation, whereas this was not always the case for a generic 1-D model.

The inherent underestimation of energy losses of the 1-D wave propagation model, due to bifurcations, non-planarity and complex geometry, were examined. The 1-D model was compared to a rigid wall 3-D computational fluid dynamic model. Newtonian and non-Newtonian blood properties were studied and the longitudinal pressure distribution along the arteries was compared with the 1-D patient-specific model mean pressure prediction. The results indicated that pressure drop is significant only in small diameter vessels such as the precerebral and cerebral arteries. In these vessels the 1-D model in comparison to 3-D models consistently underestimated pressure drop. The complex flow patterns resulting from asymmetry and bifurcation yield shear stresses in the 3-D model that were greater than the 1-D model.

A 3-D unsteady fluid structure interaction simulation in a patient-specific model was performed to simultaneously capture the flow details, given by the 3-D model, and wave propagation phenomena, provided by the 1-D model. The 3-D unsteady fluid structure interaction approach is the most computationally intense and cumbersome, but it allows physiological simulations with a high level of detail and accuracy. For instance, this approach could be relevant to obtain blood flow details in

regions that are prone to atherosclerotic plaques or development of aneurysms. The 3-D fluid structure interaction simulation was performed for a patient-specific aorta. Important clinical parameters such as wall shear stress were quantified and significant differences were found in comparison to the rigid wall 3-D simulation indicating the relevance of a fluid structure interaction approach. A comparison of the fluid structure interaction to an equivalent 1-D model resulted in good reproduction of the pressure and flow waveforms.

The effect of a decreased compliance of the arterial tree on hemodynamical parameters has been assessed with the use of a 1-D model. Local, proximal aorta and global stiffening of the arterial tree were modeled and led to two different mechanisms that contribute to the increase in central pulse pressure. They probably both contribute to systolic hypertension and their relative contribution depends on the topology of arterial stiffening and geometrical alterations taking place in aging or in disease.

All these patient-specific models are about to being in use in a clinical environment and will be useful for providing better diagnostics and treatment planning in a near future.

KEYWORDS

Wave propagation, hemodynamic, cerebral circulation, 1-D model, noninvasive measurements techniques, PC-MRI, MRI, MRA, Doppler, heart model, ventricular-vascular coupling, viscoelasticity, vascular imaging, CFD, FSI, Non-Newtonian blood, blood flow simulation, medical images reconstruction.

NOMENCLATURE

a.	artery
ACA	anterior cerebral artery
BA	basilar artery
CA	cerebral aneurysm
CBF	cerebral blood flow
CCA	common carotid artery
CFD	computational fluid dynamic
CoW	circle of Willis
CSF	cerebral spinal fluid
CT	computed tomography
ECA	external carotid artery
E_N	normalized elastance
FSI	fluid structure interaction
HR	heart rate
ICA	internal carotid artery
ISH	isolated systolic hypertension
MCA	middle cerebral artery
MRI	magnetic resonance imaging
PCA	posterior cerebral artery
PC-MRI	phase contrast MRI
t_{max}	time to reach maximum elastance
t_N	normalized time
VA	vertebral artery
VEM	varying elastance model
WSS	wall shear stress

INTRODUCTION

Motivation

Blood flow phenomena and related hemodynamical forces play an important role in various forms of cerebrovascular disease. The temporal profile of wall shear stress seems to play a role in atherogenesis and the stability of plaque in the carotid bifurcation (DePaola, Gimbrone et al. 1992; White, Haidekker et al. 2001; Gambillara, Montorzi et al. 2005). The wall shear stress acting on the endothelial cells is linked to growth and possibly rupture of the aneurysm wall (Cebral, Castro et al. 2005) (Fig. 1). From a clinical standpoint, the assessment of hemodynamical forces within the cerebral circulation is still difficult because pressure can be measured only invasively and flow, especially in small deep intracranial vessels such as those in the vicinity of the circle of Willis, cannot be measured directly with Doppler ultrasound. This renders modeling of blood flow within the cerebral circulation an attractive alternative.

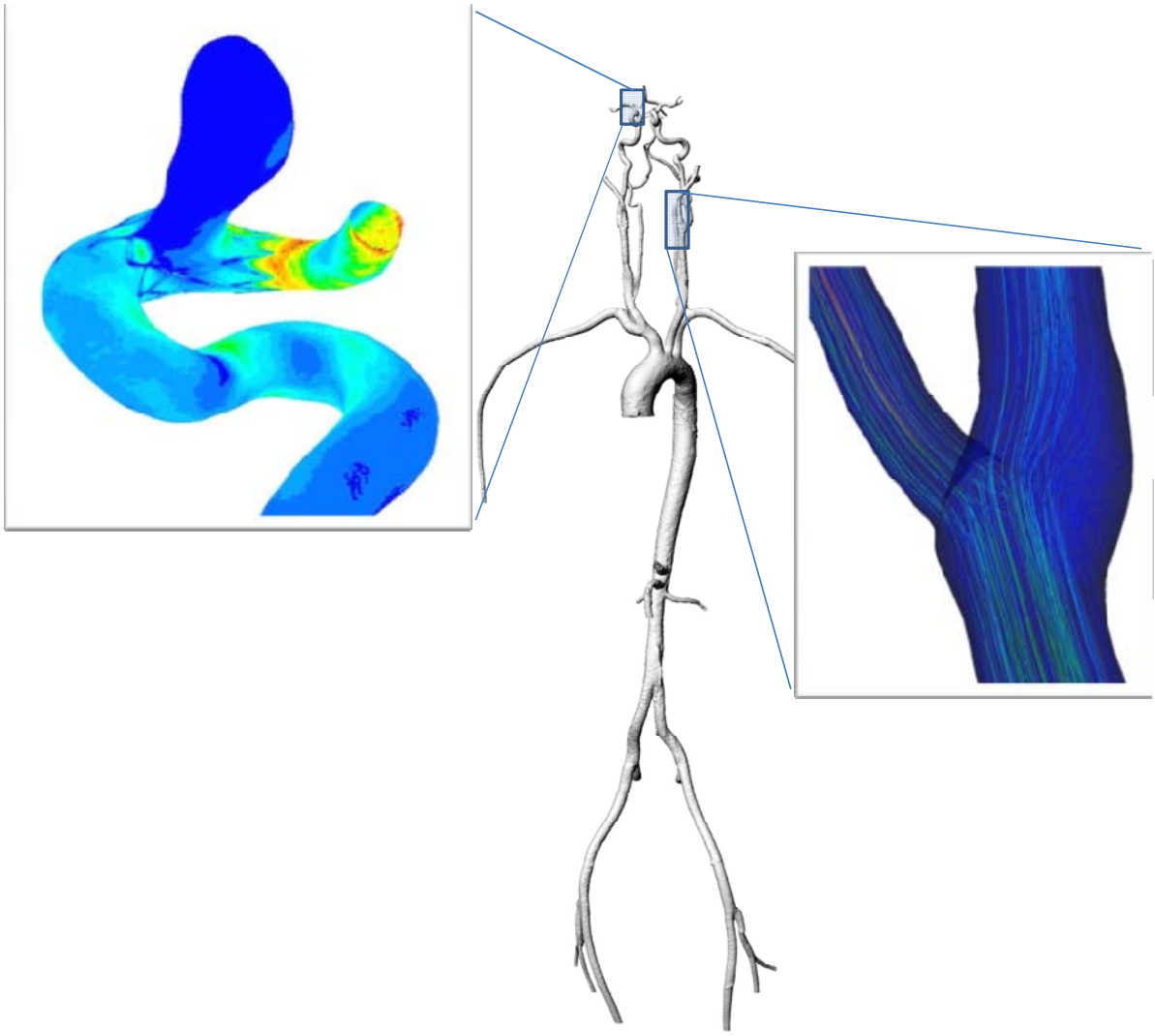

Figure 1. Example of computational blood flow simulation in a cerebral aneurysm with stent (left) and complex secondary blood flow inside an arterial bifurcation (right).

Modern imaging modalities, such as magnetic resonance imaging, MRI, computed tomography, CT and 3-D digital subtraction angiography provide high-definition images of the vessel geometry and thus can give precise description of the local 3-D geometry with millimeter resolution, a spatial definition which is necessary for accurate simulation of the flow field by computational fluid dynamics (CFD) and fluid structure interaction (FSI) simulations. However, CFD and FSI simulations require not only accurate description of geometry but also accurate boundary conditions, often expressed as flow or pressure waveforms in the afferent (upstream) and efferent (downstream) vessels (Fig. 2). As mentioned earlier, flow and pressure are not measurable in deep and small cerebral vessels. Thus, modeling approaches are desirable and was the aim of the recent European Commission @neurIST Project (European Commission contract no. IST-027703).

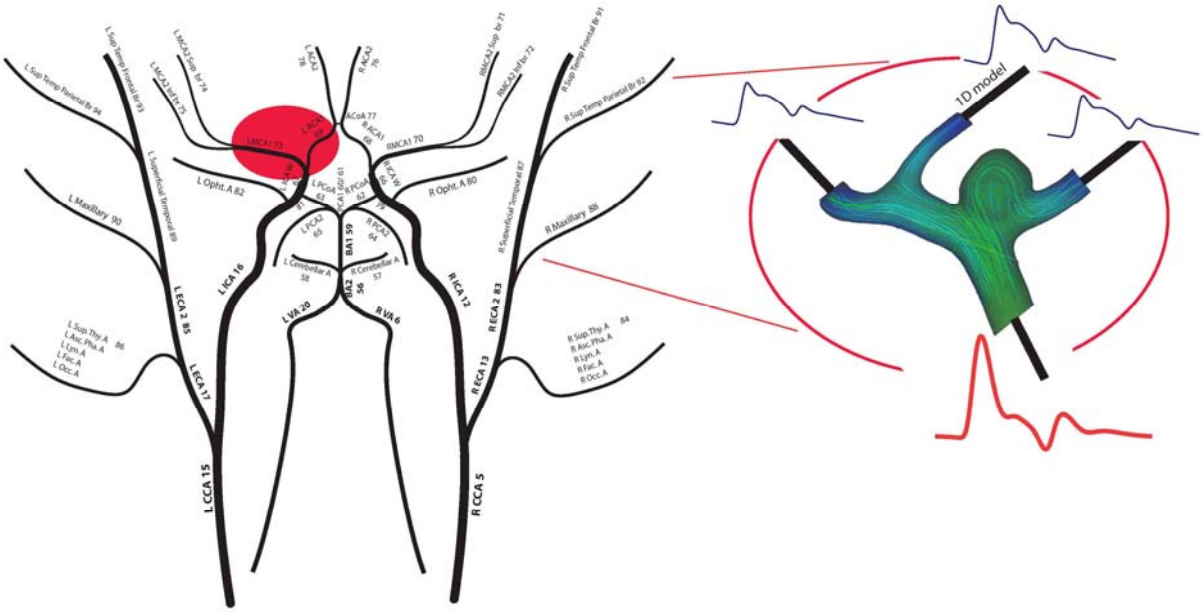

Figure 2. Blood flow simulation in a patient-specific cerebral aneurysm with boundary condition waveforms obtained with the 1-D model.

Because of their relatively low computational cost and complexity, 1-D models have been extensively used in the past to study different pathologies, such as hypertension (Westerhof, van den Wijngaard et al. 2008), arteriosclerosis (Raines, Jaffrin et al. 1974), stenosis (Avolio 1980; Stettler, Niederer et al. 1981; Stettler, Niederer et al. 1981; Meister 1983; Kufahl and Clark 1985; Stergiopulos, Young et al. 1992; Cassot, Zagzoule et al. 2000), anatomical variations of cerebral arteries and arterial occlusion (Alastruey, Parker et al. 2007) and for surgical planning (Wan, Steele et al. 2002).

In the case of isolated systolic hypertension, pressure load on the heart is affected by the contribution of pressure waves that travel forward and backward (reflected waves). In this situation, hemodynamics are governed by global wave phenomena and to a lesser extent by local 3-D flow. Therefore, wave propagation models (1-D models) are the most appropriate. 1-D models are also able to provide pressure and flow waveforms in an extended region of the arterial tree, which is useful for diagnostics and treatment planning (Taylor and Figueroa 2009). Outcome of bypass surgery predicted by a 1-D wave propagation model with MRI data has been reported (van de Vosse and Stergiopulos 2011). An extended review of literature on the 1-D wave propagation models is provided in the first paper of this thesis.

Overall goal

The primary goal of this thesis is to develop and validate a generic and patient-specific model of the systemic circulation including a detailed description of the cerebral circulation. In vivo validation of the 1-D model is based on comparison with in vivo measurement of flow (ultrasound Doppler, MRI) and pressure (applanation tonometry) on volunteers and patients.
A comparison and assessment of the 1-D model with 3-D rigid wall and 3-D FSI models is performed.

The models are used to:
a) Predict blood pressure and flow rate waveforms in primary systemic and cerebral arteries
b) Characterize the local 3-dimensional flow field in pathological points of interest, such as at the aortic arch and in cerebral aneurysms
c) Better understand the mechanisms of systolic hypertension

Cardiovascular Physiology

The circulation system provides blood with oxygen, nutrients and hormones to tissues and removes carbon dioxide and waste products. The circulation is composed of arteries, arterioles capillaries, venules and veins. Arteries bear high blood pressure leaving the heart. Arterioles are small branches that can regulate the resistance of flow by the presence of smooth muscle cells. Nearly half of the vascular resistance is due to small arteries and arterioles. Capillaries are the interface between the blood and tissues and permit the exchange of nutrients and substances. Venules are small branches that connect to the veins to bring low pressure blood back to the heart. Most of blood volume (64 %) resides in the veins.
The heart is a pump composed of two sides and four chambers. The left side propels blood into the systemic circulation at high pressure and the right side to the pulmonary circulation. Each side is composed of two chambers, an atrium and ventricle. The atrium has a primary goal to transfer blood across the mitral (left) or tricuspid (right) valve to the ventricle, which further propels blood into the arterial tree across the pulmonary (right) valve for the pulmonary circuit (lesser circulation), and the aortic (left) valve for the systemic circuit (great circulation), respectively. These valves prevent blood from flowing backward.
In this thesis, we focus our work on the systemic arterial tree. Elasticity of the arterial wall limits blood pressure (Windkessel effect) thereby reducing load on the vessel walls and left ventricle heart load. The elasticity (or viscoelasticity) of the arterial wall also results in pressure and flow wave propagation along the arterial tree.

Generic models

We are interested to build a generic arterial tree model of the systemic circulation with specific detail of cerebral circulation. This model represents a subject with average arterial geometry and elastic properties.
Some data for pressure and flow in major systemic arteries is available, where Doppler measurements for flow are accessible and tonometry (for pressure) is feasible (Kelly, Hayward et al. 1989). However, non-invasive measurements of intracranial pressure and flow waves are scarce. Most of the measurements have been performed for extracranial arteries such as the common carotid by Doppler ultrasound (Holdsworth, Norley et al. 1999) and the internal carotid and vertebral artery flow rate by MRI (Ford, Alperin et al. 2005). Few data are available for the efferent vessels of the circle of Willis (anterior, middle and posterior cerebral arteries (Aaslid, Lash et al. 2003)). For systemic arteries, there is no complete data set for pressure and flow measured at several arterial locations and where arterial properties are also measured or estimated on an individual basis. Hence, 1-D model validation cannot be based on data in the literature. Thus, we performed a more complete set of non-invasive measurements than previous studies.

The approach we followed was to compare the predictions of the generic 1-D model with the average pressure and flow waveforms measured noninvasively in a group of healthy young people. The underlying hypothesis was that although the generic model would not represent precisely a specific individual it would represent the “average” of the group. Hence, the model validation was strictly qualitative.

Geometry of the arterial network was obtained from the literature (Gabrielsen and Greitz 1970; Krayenbuehl and Yasargil 1982; Yasargil 1982; Yasargil 1984; Hillen, Hoogstraten et al. 1986; Krabbe-Hartkamp, van der Grond et al. 1998; Holdsworth, Norley et al. 1999) and completed by patient MRI scans. Elastic properties were taken from values reported in the literature (Hayashi, Handa et al. 1980; Hayashi, Nagasawa et al. 1980).

Generic models are useful for research purposes and after normalization (age, weight, …) have potential to provide patient-specific pressure and flow waveforms to study blood flow in cerebral aneurysm with realistic predictions (Marzo, Singh et al. 2011).

Patient-specific models

Interest in patient-specific models of the systemic circulation has increased in recent years (Perktold and Rappitsch 1995; Gerbeau and Chapelle 2005; Quarteroni, Formaggia et al. 2009; Taylor and Figueroa 2009). A decrease in numerical simulations time in conjunction with increased availability of clinical data for geometry and elastic properties have made patient-specific models more feasible. For instance, patient-specific models are now utilized to assess the risk of aneurysm rupture, plan surgical procedures and predict treatment outcome. The reproducibility of patient-specific hemodynamic simulations has been reported in the literature for numerical simulation of cerebral aneurysms (Radaelli, Augsburger et al. 2008). Such patient-specific approaches may lead to novel diagnostic and treatment planning tools in the future. Thus, we constructed a model based on patient-specific geometry, elasticity, and noninvasive flow and pressure measurements from the same subject.

Theoretical and numerical models

0-D Lumped model

0-D or the Windkessel model is a lumped model composed of resistance, compliance and inertial components (electrical circuit analog) connected in series and parallel. A classic example of a 3 element Windkessel model is presented in (Fig. 3). R_1, R_2 and C_T correspond to proximal resistance, distal resistance and terminal compliance, respectively. They are utilized to mimic part of or the entire arterial tree. They give information on flow and pressure; however they do not take into account wave propagation phenomena. Their advantage lies in the few parameters required for characterization.

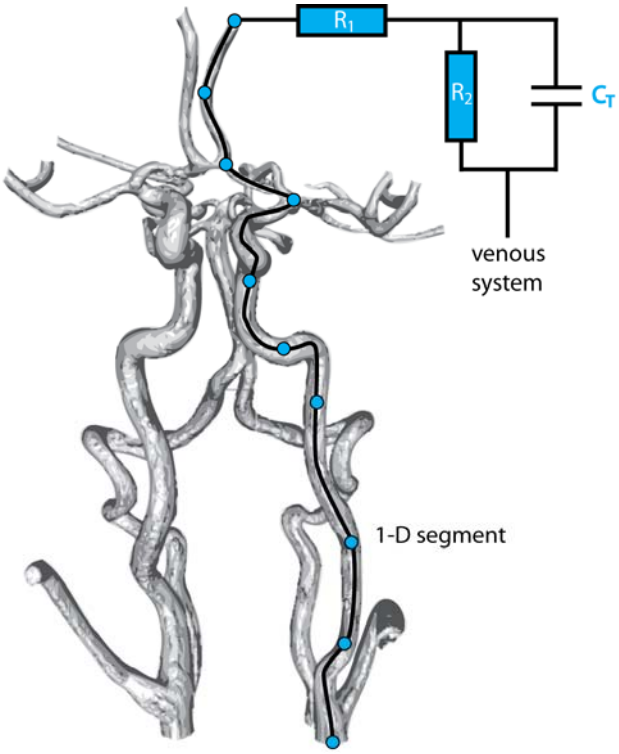

Figure 3. A 3 element Windkessel model connected to the distal region of an anterior cerebral artery.

1-D distributed model

The main arteries of the arterial tree are decomposed into interconnected straight arterial segments. In each of these segments, one can either solve the integrated forms of the Navier-Stokes equations or use the oscillatory flow theory from (Witzig 1914; Womersley 1955) or the electrical transmission line theory (Westerhof, Bosman et al. 1969).

The arterial tree includes a detailed description of the cerebral artery network (Fig. 3). We have included all main cerebral artery segments as well as all afferent and efferent arteries in the vicinity of the circle of Willis. This is useful when studying blood flow in cerebral aneurysm, as such circle is the most frequent location of cerebral aneurysms (Yasargil 1984). Many extracranial arteries, such as the superficial temporal arteries have also been added, in order to include points where pressure can be measured noninvasively (tonometry), a step that is required for the validation phase of the work.

In this thesis, 1-D wave propagation is based on the integrated forms of the continuity and axial-momentum equations of the Navier-Stokes equations and a description of the local arterial wall compliance. A viscoelastic constitutive relation linking distending pressure to local cross-sectional area was implemented. Their advantages reside in the possibility to consider non-linearity of the blood fluid mechanics and arterial wall solid mechanics equations.

Because of their hyperbolic character, the 1-D flow equations are well adapted to reproduce the wave propagation phenomena in the systemic arterial tree. In contrast to 3-D CFD models of local flows, which require powerful computations, 1-D models are much simpler and require little computational power. Within seconds, 1-D models can give accurate predictions of pressure and flow in all the main arteries, which offers a distinct advantage for clinical applications using patient specific data.

1-D models of the systemic circulation have been extensively studied in the past (Westerhof, Bosman et al. 1969; Schaaf and Abbrecht 1972; Avolio 1980; Meister 1983; Zagzoule and Marc-Vergnes 1986; Stergiopulos, Young et al. 1992; Cassot, Zagzoule et al. 2000). These studies were focused on the main systemic arteries, from the ascending aorta to the upper and lower limbs. Only 2 studies have considered the cerebral circulation in detail (Zagzoule and Marc-Vergnes 1986; Cassot, Zagzoule et al. 2000). Cassot et al. studied the role of the circle of Willis on the flow and pressure distribution in the case of internal carotid stenosis and in the autoregulation during arterial hypotension. A major drawback of the study of Cassot et al. and Zagzoule and Marc-Vergnes laid in the fact that although the cerebral circulation was described in detail, the rest of the arterial tree was not taken into account, which limits the applicability and generality of this approach. Furthermore, all of the actual 1-D models published in the literature used a measured proximal boundary condition or an idealized flow or pressure at the root of the ascending aorta. This modeling approach does not take into account the coupling between the left ventricle and the systemic arterial tree. The lack of ventricular-vascular coupling is a major shortcoming, because it assumes that the heart acts as either a flow or a pressure source, which is not true from a physiological standpoint. The heart is neither a pressure nor a flow pump and it is the interaction between the pump (heart) and load (arterial tree) which determines the genesis of the aortic flow and pressure wave. Furthermore blood is assumed to be a Newtonian fluid with constant density and dynamic viscosity.

At the proximal end (ascending aorta), the arterial tree is coupled to the heart, which will be modeled using the time varying elastance model, providing a versatile and physiologically relevant way to take into account parameters like heart rate, maximum contractility, changes in preload and atrial pressure. At terminal sites, all distal vessels and vascular beds are modeled as a three-element Windkessel model, indeed, modeling of the small distal arteries, arterioles and capillaries using 1-D fluid mechanics equations is not possible or useful (Fig. 3).

3-D Computational fluid dynamics

Unlike the 1-D wave propagation model, 3-D Computational fluid dynamics consists of solving the full Navier-Stokes equations with finite element or finite volume methods. 3-D CFD models are appropriate to study complex flow structures in local geometries of interest, such as arterial bifurcations (Taylor, Hughes et al. 1998), the abdominal aorta (Taylor, Hughes et al. 1998), aneurysms (Cebral, Castro et al. 2005) or close to cardiac valves. CFD simulation of blood flow has become a relevant way to analyze the flow patterns in patient-specific vasculature. The aim is to provide a better understanding of the flow fields and the resulting hemodynamical forces on the arterial wall, as these forces are implicated in the genesis, evolution and regression of vascular pathologies. For instance the role of the wall shear stress on formation and stability of atherosclerotic plaques in the carotid bifurcation (Steinman 2002) and the growth and rupture of cerebral aneurysms (Cebral, Castro et al. 2005) are two important examples that bolster this concept.

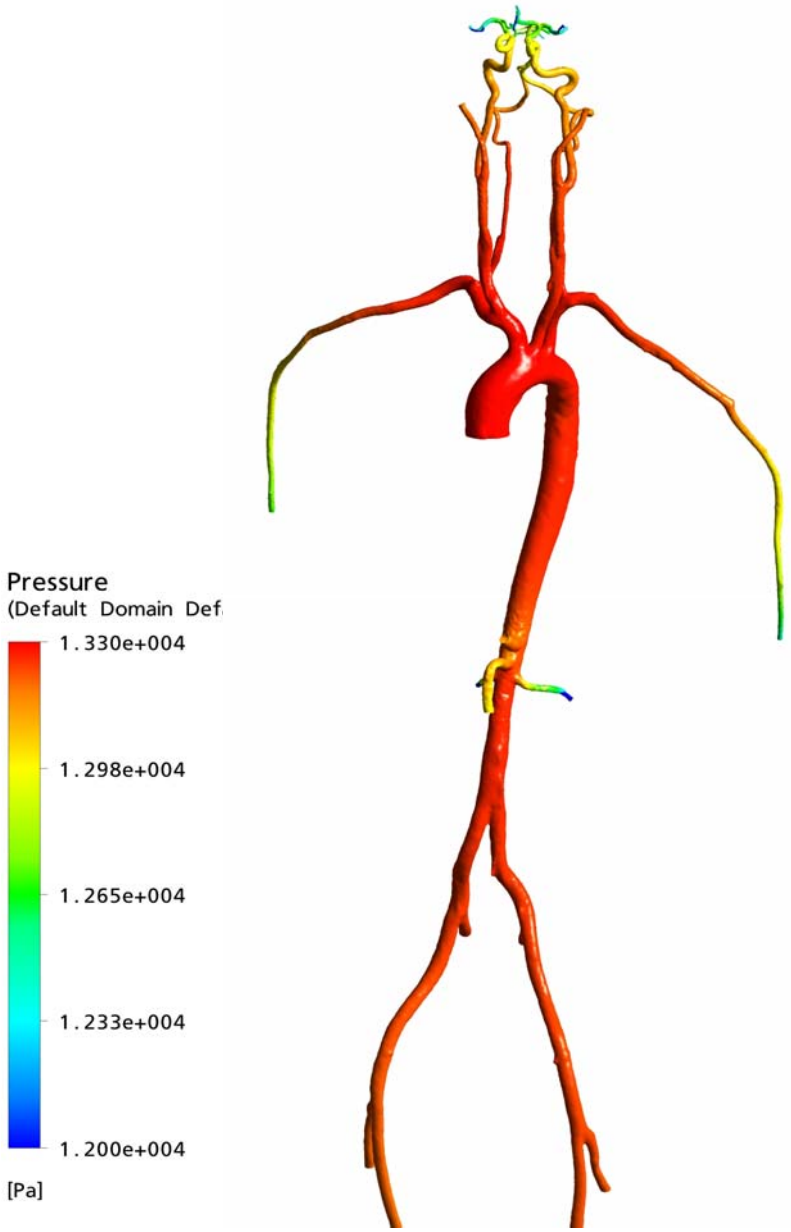

Figure 4. Blood pressure in a patient-specific arterial tree computed by 3-D CFD.

3-D models are still difficult to apply in extended regions of the arterial tree, because they are computationally expensive and required difficult geometry preparation. Therefore a multi-scale approach, where 3-D CFD is coupled to a distributed 1-D model is often utilized. The 1-D model, serves to provide pressure and flow boundary conditions required by the 3-D solver. Figure 4 is an example of 3-D blood flow simulation over an extended region of the arterial tree. Main arterial branches, arising from the ascending aorta up to small cerebral vessels distal the circle of Willis, are considered.

3-D Fluid Structure Interaction

Most of the 3-D models that are utilized to study blood flow consider the vessel wall to be a rigid structure. These rigid wall models make an intrinsic assumption that the wall motion does not affect the flow field significantly. This assumption simplifies the numerical approach and is fully justifiable only in the cases where the wall motion is relatively small. However, when significant arterial wall deformation occurs during the heart cycle, such as the 10-15% diameter change of the aorta, it becomes essential to consider deformation of the arterial wall. A fluid-structure interaction approach is necessary to address this issue to provide physiological simulations with a high level of precision. In addition to fluid mechanics equations, FSI will solve the solid mechanic equations for the arterial wall.

Fluid structure interaction modeling of a patient-specific vasculature is complex and computationally expensive due to the additional geometry (arterial wall) and boundary conditions (outer surface of the arterial wall) needed for such simulation. However, the development of automated meshing processes in conjunction with the use of more efficient parallel algorithms renders the FSI approach applicable in research or clinical framework in the near future.

Non-invasive medical measurement techniques

The following briefly describes the techniques utilized in this thesis to improve and validate the models.

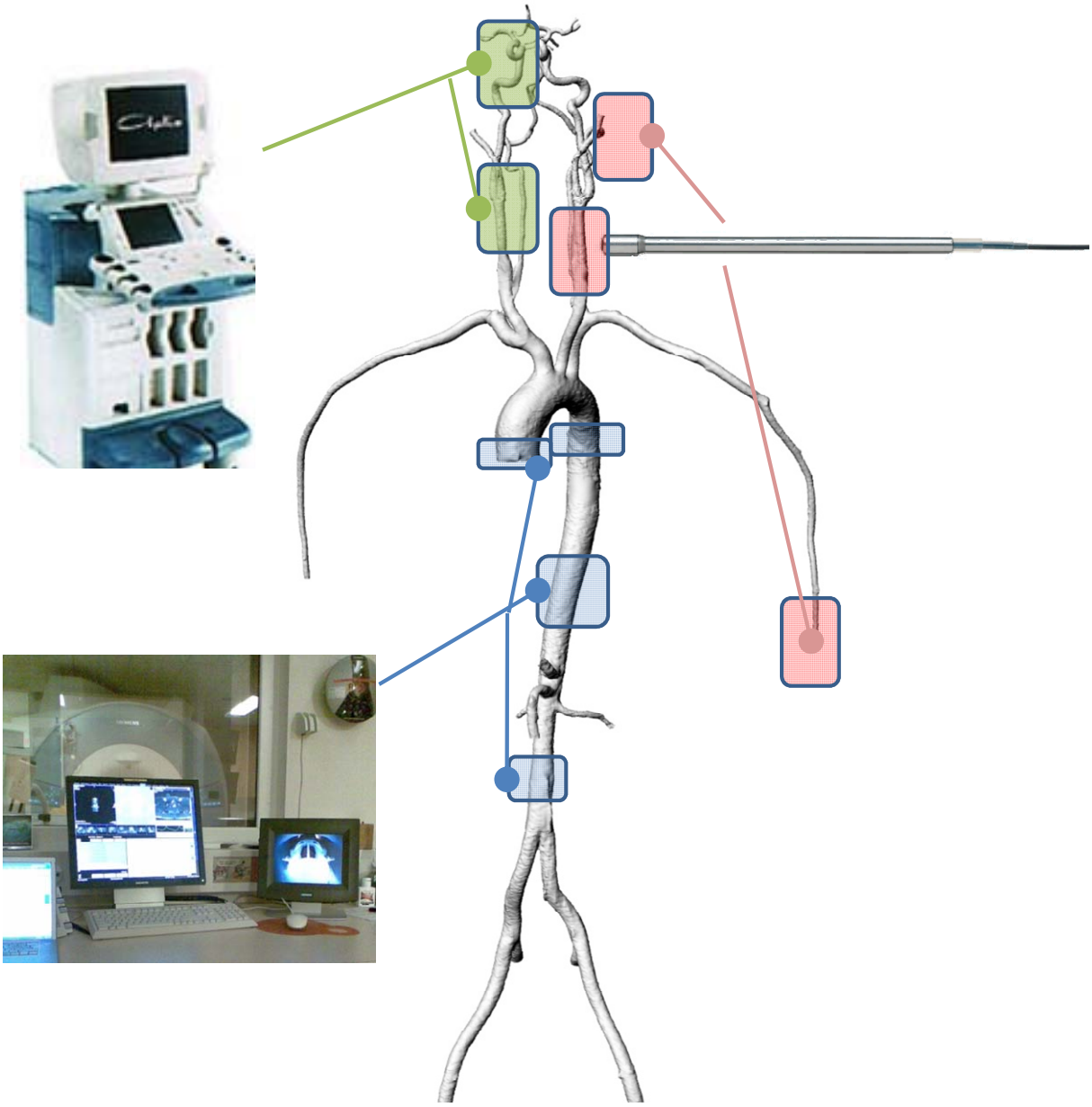

Figure 5. Blood flow was measured with PC-MRI in aortic locations, velocity with transcranial Doppler in precerebral and intracranial arteries and pressure waveform with applanation tonometry at the temporal, carotid and radial arteries.

Magnetic resonance angiography MRA and phase contrast PC-MRI

Magnetic resonance angiography is a MRI technique to visualize the blood flow regions (Fig. 5). It can be done with or without injection of contrast agent to enhance the image quality. This modality has an advantage over computed tomography (CT) scans that expose the subject to X-ray irradiation. The technical drawback is the lower spatial resolution attained on the order of 0.5 – 1.0 mm.

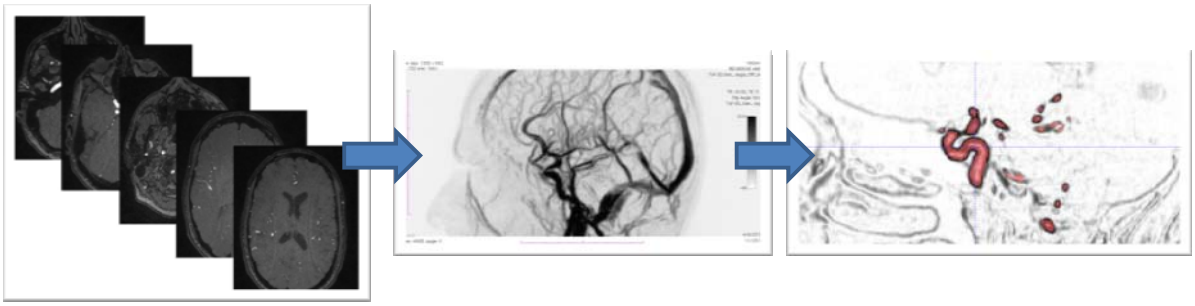

Figure 6. Stack of image slices obtained by MRI (left), angiography of the main cerebral vessels (arteries and veins) (middle) and the segmentation of the vessel lumen (right).

Once the stack of slices is acquired, a second software is used to segment the dicom images (medical format of the images) to obtain a raw 3-D surface of the vessel lumen (Fig. 3). Post processing is necessary to obtain a geometry that is appropriate for the simulation. This surface corresponds to the lumen of the vasculature. The inner volume is meshed with tetrahedral elements (where 3-D equations are solved) and finally imported into a CFD solver.

Phase Contrast MRI is a specific MRI sequence that enables quantification of the temporal variation of blood velocity. In this technique both magnitude and phase images are acquired simultaneously (Fig. 7).

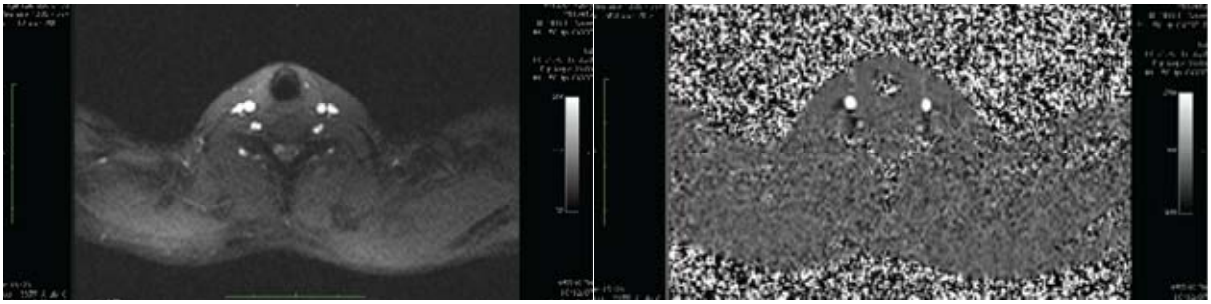

Figure.7 Example of Phase Contrast images at the same location (axial slice at the neck region). Magnitude encoded image (left) and phase encoded counterpart (right).

In the phase images, the velocity at each pixel is proportional to the contrast. When acquired in a vessel cross-section, the integration of the normal velocities over the area gives the volumetric blood flow. At present, temporal resolution is limited to 20 or 30 frames per cardiac cycle using phase contrast MRI. This number of frames is sufficient to obtain an accurate flow waveform.

Transcranial Doppler

Transcranial Doppler measurement was utilized in this thesis to provide peak blood velocity waveforms (Fig. 8). Color-coded duplex flow imaging with linear phase array and a sectorial transducer was used to assess blood flow velocities in the cerebral vasculature via the temporal, orbital and occipital acoustic bone windows.

Blood velocity in the following extracranial and intracranial arteries was measured: common carotid a., external carotid a., internal carotid a., vertebral a., middle cerebral a., anterior cerebral a., posterior cerebral a., basilar a. and ophthalmic a.. With knowledge of the blood velocity and some assumptions, the flow rate waveforms can be determined using Womersley's theory for pulsatile flow (Womersley 1955).

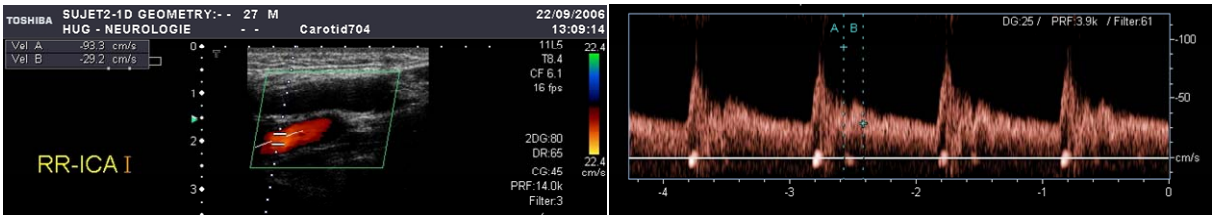

Figure 8. Longitudinal cross section of the vessel and ultrasound beam (left). Typical peak velocity, of 4 consecutives heart cycles, measured in the internal carotid artery.

Applanation tonometry

One possibility for non invasive measurement of pressure waveform is applanation tonometry (Fig. 5). Applanation tonometry can be performed only on superficial arteries, ideally with a rigid (bony) structure underneath. These measurements are performed usually in the following arteries: superficial temporal a., carotid a. (vicinity of the carotid bifurcation) and radial a. Because applanation tonometry does not yield a calibrated signal, calibration is performed by comparison with brachial systolic and diastolic pressure obtained by a standard sphygmomanometer (Segers, Rietzschel et al. 2005).

Other applications of 1-D models

Coronary circulation

Coronary circulation can also be studied with 1-D models and can help understanding the physiological specificity of the coronary circulation (Rogers, Kiyooka et al. 2006). Contraction of the myocardium affects the surrounding arteries irrigating the heart, which can be seen on a typical blood flow waveform in the coronary branch (Fig. 9).

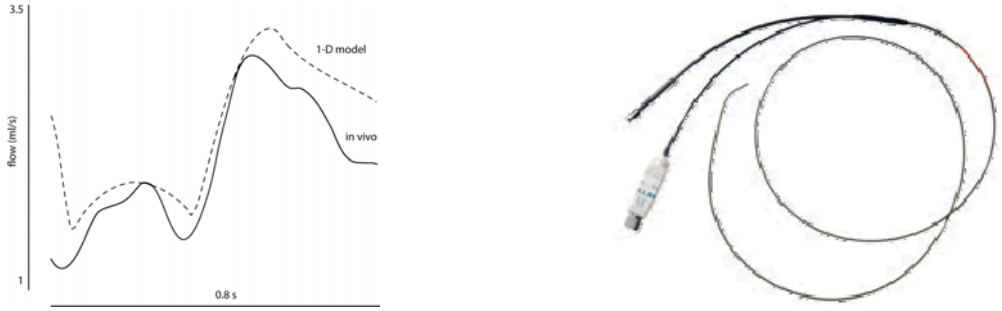

Figure 9. Coronary blood flow waveforms measured and simulated by the 1-D model (left); measured was performed with intra-arterial pressure-velocity catheter (right).

In vivo measurement shows a reduction of flow in the systolic phase and elevation in the diastolic phase, which is different than the rest of the systemic circulation. Many questions remain regarding the physiology and hemodynamics of coronary circulation and numerous models have been proposed. Classical models referred to the systolic extravascular model, waterfall model or intramyocardial pump model and the effect of the contraction can be affected by the elastance and/or pressure of the left ventricle. These different models can be studied with the help of a 1-D wave propagation approach.

Pulmonary circulation

Pulmonary circulation can also be studied by the 1-D model to study pulmonary hypertension. However, the latter presents some unique differences from the systemic arterial tree, including a higher and uniform distensibility of the main branches (McDonald, Nichols et al. 1990), and therefore need to be adapted in terms of ventricle elastance, vessel distensibility and distal compliances. Figure 10 is a 3-D geometry of the main pulmonary branches, acquired with MRA scan, used to build the model.

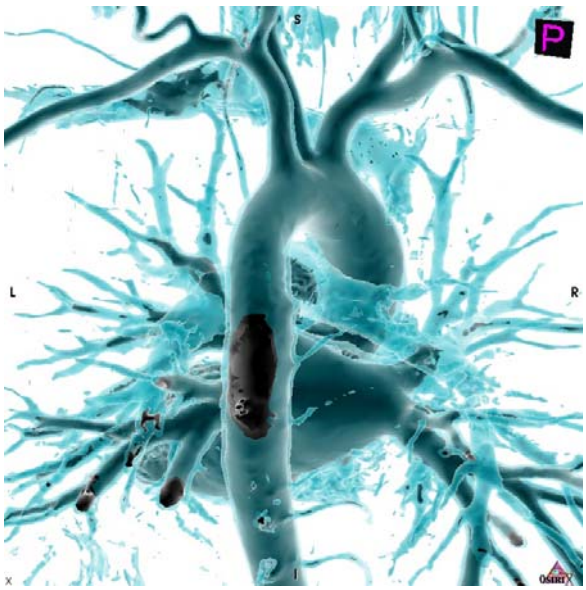

Figure 10. Posterior view of the aortic arch and main branches, thoracic aorta and main pulmonary arteries obtained from a MRA scan.

Inverse problem

Based on a person-specific in vivo measurements, a 1-D model can be used and optimized to find the better fit between measured and simulated pressure and flow waveforms, by adjusting key parameters such as compliance, geometry, and elastance (Leguy, Bosboom et al. 2010). Estimation of the arterial tree or heart model parameters can be useful to characterize the state of the arterial tree.

Transfer function

Central aortic pressure is a better indicator of cardiac risk than distal peripheral pressure. However, aortic pressure is only available with invasive measurements. Thus, the use of a transfer function between peripheral and central pressure could be a useful clinical tool to help for a better understanding of the cardiac risk in a non-invasive manner. A 1-D wave propagation model is well suited for this task (Stergiopulos, Westerhof et al. 1998; Westerhof, Guelen et al. 2007).

1-D model has also been used recently to evaluate the wave propagation theory of a method that measure the stiffness of central arteries with a new and non invasive device (Trachet, Reymond et al. 2010).

ABSTRACTS OF PAPERS

PAPER I

A distributed model of the human arterial tree including all main systemic arteries coupled to a heart model is developed. The one-dimensional form of the momentum and continuity equations is solved numerically to obtain pressures and flows throughout the systemic arterial tree. Intimal shear is modeled using the Witzig-Womersley theory. A nonlinear viscoelastic constitutive law for the arterial wall is considered. The left ventricle is modeled using the varying elastance model. Distal vessels are terminated with three-element Windkessels. Coronaries are modeled assuming a systolic flow impediment proportional to ventricular varying elastance. Arterial dimensions were taken from previous 1D models and were extended to include a detailed description of cerebral vasculature. Elastic properties were taken from the literature. To validate model predictions, noninvasive measurements of pressure and flow were performed in young volunteers. Flow in large arteries was measured with MRI, cerebral flow with ultrasound Doppler and pressure with tonometry. The resulting 1D model is the most complete, because it encompasses all major segments of the arterial tree, accounts for ventricular-vascular interaction and includes an improved description of shear stress and wall viscoelasticity. Model predictions at different arterial locations compared well to measured flow and pressure waves at the same anatomical points, reflecting the agreement in the general characteristics of the "generic 1D model" and the "average subject" of our volunteer population. The study constitutes a first validation of the complete 1D model using human pressure and flow data and supports the applicability of the 1D model in the human circulation.

PAPER II

The aim of this study is to develop and validate a patient-specific distributed model of the systemic arterial tree. This model is built using geometric and hemodynamic data measured on a specific person and validated with non-invasive measurements of flow and pressure on the same person, providing thus a patient-specific model and validation. The systemic arterial tree geometry was obtained from MR angiographic measurements. A non-linear viscoelastic constitutive law for the arterial wall is considered. Arterial wall distensibility is based on literature data and adapted to match the wave propagation velocity of the main arteries of the specific subject, which were estimated by pressure waves traveling time. The intimal shear stress is modeled using the Witzig-Womersley theory. Blood pressure is measured using applanation tonometry and flow rate using transcranial ultrasound and phase-contrast MRI. The model predicts pressure and flow waveforms in good qualitative and quantitative agreement with the in-vivo measurements, in terms of wave shape and specific wave features.

Comparison with a generic 1-D model shows that the patient-specific model better predicts pressure and flow at specific arterial sites. These results obtained let us conclude that a patient-specific 1-D model of the arterial tree is able to predict well pressure and flow waveforms in the main systemic circulation, whereas this is not always the case for a generic 1-D model.

PAPER III

One-dimensional models of the systemic arterial tree are useful tools for studying wave propagation phenomena, however, their formulation for frictional losses is approximate and often based on solutions for developed flow in a straight non-tapered arterial segments. Thus, losses due to bifurcations, tortuosity, non-planarity and complex geometry effects cannot be accounted for in 1-D models. This may lead to significant errors in the estimation of mean pressure. To evaluate these errors, we simulated steady flow in a patient specific model of the entire systemic circulation using a standard CFD code with Newtonian and non-Newtonian blood properties and compared the pressure evolution along three principal and representative arterial pathlines with the prediction of mean pressure, as given by the 1-D model. Pressure drop computed from aortic root up to iliac bifurcation and to distal brachial is less than 1 mmHg and 1-D model predictions agree well with the 3-D model. In smaller vessels like the precerebral and cerebral arteries, the losses are more significant, (mean pressure drop over 10 mmHg from mean aortic pressure) and are consistently underestimated by the 1-D model. Complex flow patterns resulting from tortuosity, non-planarity and branching yield shear stresses, which are higher than the ones predicted by the 1-D model. In consequence, the 1-D model overestimates mean pressure in peripheral arteries and especially in the cerebral circulation.

PAPER IV

Interest in patient-specific models of the systemic circulation has increased substantially in recent years. Clinical data for 3D geometry and elastic properties of the arterial tree become more readily available and numerical methods are also more efficient and easier to use, rendering patient-specific modeling relevant and feasible. Among the different numerical models used to study the blood circulation in the main arteries, fluid structure interaction (FSI) is the most computationally intense and cumbersome but allows physiological simulations with high level of details and accuracy.

Patient-specific tree starting at the proximal aorta and including the main proximal arterial branches was created based on geometry acquired using MRI angiography. The lumen geometry was obtained after segmentation. The arterial wall geometry was created with a variable thickness. The boundary conditions for the fluid domain at the ascending aorta root were either pressure or flow waveform. Flow waveforms were imposed for each outlet. The waveforms were obtained using phase contrast MRI for blood velocity or completed by results from a 1-D model, when not available at a specific location. The 1-D model was validated quantitatively on the same person. To mimic the mechanical effect of surrounding tissues in the 3-D FSI simulation, a linear stress-displacement constitutive relation was applied on the outer surface of the arterial wall.

A comparison between compliant and rigid wall flow simulations, with the same set of physiological boundary conditions is done. The temporal variation and spatial patterns of wall shear stress are presented. Averaged wall shear stress differences between FSI and rigid wall simulations were -11 %, 68 % and 37 % at lower, middle and upper locations in the aortic arch respectively and 5.7 %, 30% at anterior and posterior locations in the thoracic aorta.

The pressure and flow waveforms at different locations are compared to the ones obtained with a 1-D model. Relative RMS of the difference between waveforms computed by 3-D FSI and 1-D model were 2.9, 3.3 % for pressure and 9.0, 11.0 % for flow at the aortic arch and thoracic aorta locations respectively.

A fluid structure interaction simulation, with physiological boundary conditions, on a patient-specific aorta has been performed. Clinical parameters of importance like the wall shear stress have been reported. Significant differences compared to a simulation with rigid walls are present that show the relevance of an FSI approach. A comparison of the FSI to an equivalent 1-D model shows good reproduction of the pressure and flow waveforms.

PAPER V

Decrease in arterial compliance leads to an increased pulse pressure, as explained by the Windkessel effect. Pressure waveform is the sum of a forward running and a backward running or reflected pressure wave. When the arterial system stiffens, as a result of aging or disease, both the forward and reflected waves are altered and contribute to a greater or lesser degree to the increase in aortic pulse pressure. Two mechanisms have been proposed in the literature to explain systolic hypertension upon arterial stiffening. The most popular one is based on the augmentation and earlier arrival of reflected waves. The second mechanism is based on the augmentation of the forward wave, as a result of an increase of the characteristic impedance of the proximal aorta.

The aim of this study is to analyze the two aforementioned mechanisms using a 1-D model of the entire systemic arterial tree.

A validated 1-D model of the systemic circulation, representative of a young healthy adult was used to simulate arterial pressure and flow under control conditions and in presence of arterial stiffening. To help elucidate the differences in the two mechanisms contributing to systolic hypertension, the arterial tree was stiffened either locally with compliance being reduced only in the region of the aortic arch, or globally, with a uniform decrease in compliance in all arterial segments.

The pulse pressure increased by 58 % when proximal aorta was stiffened and the compliance decreased by 43 %. Same pulse pressure increase was achieved when compliance of the globally stiffened arterial tree decreased by 47 %. In presence of local stiffening in the aortic arch, characteristic impedance increased to 0.10 mmHg s/ml vs. 0.034 mmHg s/ml in control and this led to a substantial increase (91 %) in the amplitude of the forward wave, which attained 42 mmHg vs. 22 mmHg in control. Under global stiffening, the pulse pressure of the forward wave increased by 41 % and the amplitude of the reflected wave by 83 %. Reflected waves arrived earlier in systole, enhancing their contribution to systolic pressure.

The effects of local vs. global loss of compliance of the arterial tree have been studied with the use of a 1-D model. Local stiffening in the proximal aorta increases systolic pressure mainly through the augmentation of the forward pressure wave, whereas global stiffening augments systolic pressure principally though the increase in wave reflections. The relative contribution of the two mechanisms depends on the topology of arterial stiffening and geometrical alterations taking place in aging or in disease.

PAPER I - VALIDATION OF A ONE-DIMENSIONAL MODEL OF THE SYSTEMIC ARTERIAL TREE

Philippe Reymond[1], Fabrice Merenda[1], Fabienne Perren[2],
Daniel Rüfenacht[3] and Nikos Stergiopulos[1]

[1] Laboratory of Hemodynamics and Cardiovascular Technology
Ecole Polytechnique Fédérale de Lausanne, Switzerland
[2] HUG, University Hospital and Medical faculty of Geneva,
Dept of Clinical Neurosciences, Neurology, Geneva, Switzerland
[3] HUG, University Hospital and Medical faculty of Geneva,
Dept of Clinical Neurosciences, Neurointerventional, Geneva, Switzerland

INTRODUCTION

One-dimensional (1D) models of the arterial tree are, to date, the models of choice for studying pressure and flow wave propagation in the arterial system. The primary reason is that 1D flow equations are hyperbolic in nature, thus well adapted to describe wave propagation phenomena. Furthermore, the solution is given only for one spatial dimension and time and thus 1D models do not require high computational power. In contrast, 3D computational fluid dynamics (CFD) models including fluid-structure interaction (FSI), although in principle amenable to describe wave phenomena, are computationally very intense and in consequence more adapted to studying detailed local flow fields rather than pressure and flow waves over extended regions or the entire arterial tree.

Distributed 1D models of the arterial tree have been used extensively in the past (cf. Table 1 for review) for simulating wave propagation in the entire (Avolio 1980; Fitchett 1991) or parts of the arterial tree (Schaaf and Abbrecht 1972; Raines, Jaffrin et al. 1974; Wan, Steele et al. 2002; Bessems, Rutten et al. 2007) under various physiological (Schaaf and Abbrecht 1972; Wemple and Mockros 1972; Zagzoule and Marc-Vergnes 1986; Olufsen, Peskin et al. 2000; Sherwin, Franke et al. 2003) or pathological conditions (Westerhof, Bosman et al. 1969; Meister 1983; Stergiopulos, Young et al. 1992; Cassot, Vergeur et al. 1995; Alastruey, Parker et al. 2007; Azer and Peskin 2007). Careful examination of the different 1D models (Table 1) reveals that these models vary substantially in many essential aspects of their formulation. The main differences, categorized in Table 1, pertain to:

1) Incorporation, or not, of a heart left-ventricle (LV) model. This aspect is essential for studying ventricular-vascular coupling effects
2) Completeness of the systemic arterial tree. Entire systemic circulation or parts thereof.
3) Detailed description of the cerebral and coronary arteries
4) Inclusion of wall viscoelastic properties
5) Approximation of wall shear stress
6) Approximation of the convective acceleration term
7) Boundary conditions at terminal sites

Table 1 shows that out of the 13 previously published 1D models of the entire systemic circulation, only 2 of them ((Formaggia et al., 2006 and Fitchett, 1991) had incorporated a heart model allowing for some degree of ventricular-vascular coupling, all others have specified aortic flow or pressure as proximal boundary condition. Furthermore, out of the same 13 1D models of the entire systemic circulation, only 2 (Avolio, 1980 and Fitchett 1991) have included a detailed description of the cerebral arterial tree and none included the coronary tree in their model. Viscoelasticity was often neglected except in Fitchett (1991) and Avolio (1980). Most of the 1D models have included a wall friction approximation based on steady flow (Poiseuille) and have neglected convective acceleration, and in the rest of the 1D models there is a significant disparity in the way wall friction and convective acceleration is approximated. There is also great disparity in the way boundary conditions at the distal termination sites are formulated.

Table 1. Literature review of distributed 1D models of the systemic arterial tree

	REF	Heart model	Complete systemic arterial	Cerebral arterial tree	Coronary arteries	Arterial wall visco-elasticit	Wall shear stress formulat	Convective acceleration	Distal vasculature models
Bessems et al. (2007)	(Bessems, Rutten et al.	-	-	-	-	-	+ (†[a])	+ (†[a])	-
Azer and Peskin (2007)	(Azer and Peskin 2007)	-	+	-	-	-	+ (*[a])	+ (*[a])	(†[b])
Huo and Kassab (2007)	(Huo and Kassab 2007)	-	-	-	+	-	-	-	(†[b])
Alastruey et al. (2007)	(Alastruey, Parker et al.	-	-	+	-	-	-	-	+ (*[b])
Formaggia et al. (2006)	(Formaggia, Lamponi et al.	+	+	-	-	-	-	+ (§[a])	+ (*[b])
Sherwin et al. (2003)	(Sherwin, Franke et al.	-	+	-	-	-	-	-	-
Wan et al. (2002)	(Wan, Steele et al. 2002)	-	-	-	-	-	-	-	-
Olufsen et al. (2000)	(Olufsen, Peskin et al. 2000)	-	+	-	-	-	+ (†[a])	+ (†[a])	(†[b])
Cassot et al. (2000)	(Cassot, Zagzoule et al.	-	-	+	-	-	-	-	-
Stergiopulos et al. (1992)	(Stergiopulos, Young et al.	-	+	-	-	-	+ (†[a])	+ (§[a])	+ (*[b])
Fitchett (1991)	(Fitchett 1991)	+	+	+	-	+	-	-	-
Papapanayotou et al. (1990)	(Papapanayotou, Cherruault et	-	-	+	-	-	-	-	-
Hillen et al. (1986)	(Hillen, Hoogstraten et	-	-	+	-	-	-	-	-
Zagzoule and Marc-Vergnes (1986)	(Zagzoule and Marc-Vergnes	-	-	+	-	-	-	-	(§[b])
Kufahl and Clark (1985)	(Kufahl and Clark 1985)	-	-	+	-	-	+ (†[a])	+ (†[a])	+ (*[b])
Meister (1983)	(Meister 1983)	-	+	-	-	-	+ (*[a])	-	-
Stettler et al. (1981)	(Stettler, Niederer et al.	-	+	-	-	-	-	-	-
Avolio (1980)	(Avolio 1980)	-	+	+	-	+	-	-	-
Raines et al. (1974)	(Raines, Jaffrin et al. 1974)	-	-	-	-	-	-	+ (§[a])	+ (*[b])
Wemple and Mockros (1972)	(Wemple and Mockros 1972)	-	+	-	-	-	+ (†[a])	+ (†[a])	-
Schaaf and Abbrecht (1972)	(Schaaf and Abbrecht 1972)	-	+	-	-	-	+ (†[a])	+ (§[a])	-
Westerhof et al. (1969)	(Westerhof, Bosman et al.	-	+	-	-	-	-	-	-
Noordergraaf et al. (1963)	(Noordergraaf, Verdouw et al.	-	+	-	-	-	-	-	-

Heart model: (+) denotes presence of a heart model coupled to the arterial tree.

Complete systemic arterial tree: (+) signifies that all major arteries of the systemic tree are included whereas (-) means that the model is restricted to specific parts of the arterial tree.

Cerebral arterial tree: (+) signifies a detailed description of the cerebral arterial tree, including the circle of Willis and smaller efferent vessels, whereas (-) means that the cerebral circulation is limited only to major cerebral vessels (i.e., carotids and vertebrals).

Coronary arteries:

(+) marks the presence of coronary arteries in the models whereas (-) denotes total omission of coronary arteries.

Arterial wall visco-elasticity:

(+) denotes modeling of a viscoelastic arterial wall, (-) means that the arterial wall is considered elastic.

Wall shear stress formulation and convective acceleration:

(-) signifies that wall shear stress is calculated based on mean flow and using Poiseuille's law. (*[a]) shear stress estimated from the Witzig-Womersley theory for pulsatile flow, (†[a]) Young and Tsai formulation, (‡[a]) approximated velocity profiles, (§[a]) flat velocity profile.

Distal vasculature models:

(*[b]) Windkessel 3 elements models (WK3), (†[b]) structured tree from (Olufsen 1999), (‡[b]) Womersley impedance, (§[b]) Microcirculation and venous system considered.

In view of the above, we undertook the present study in order to construct an 1D model of the entire arterial circulation which is as complete as possible, i.e., it incorporates a heart model, it includes a detailed description of the cerebral and coronary arterial tree, it models nonlinear and viscoelastic properties of the wall in a physiologically relevant manner, it includes wall friction and convective

acceleration effects while respecting the pulsatile nature of the velocity profile and provides for realistic distal boundary conditions at the termination sites. This model is subsequently validated against measurements of pressure and flow waves measured in various locations of the arterial tree in a group of young and healthy individuals to qualitatively assess correspondence between model predictions and actual arterial pressure and flow waves.

METHODS

Mathematical model

Governing equations

Arteries are considered as straight long tapered segments with viscoelastic wall. The 1D continuity and momentum equations are obtained by integrating the continuity and longitudinal momentum equations of the Navier-Stokes equations:

$$\frac{\partial A}{\partial t}+\frac{\partial Q}{\partial x}+\psi=0 \qquad (1)$$

$$\frac{\partial Q}{\partial t}+\frac{\partial}{\partial x}\left(\int_A u^2 dA\right)=-\frac{A}{\rho}\frac{\partial P}{\partial x}-2\pi R\,\frac{\mu}{\rho}\frac{\partial u}{\partial r}\bigg|_{r=R}+A\,b_x \qquad (2)$$

where *A(x,t)* is the instantaneous arterial lumen area of radius *R(x,t), u(r,x,t)* the longitudinal velocity component, *Q(x,t)* the volumetric flow rate (VFR), *P(x,t)* the transmural pressure, $\tau_w(x,t)$ the wall shear stress, b the body forces and ψ the arterial wall seepage. Blood is assumed to be a Newtonian fluid with density ρ and dynamic viscosity μ. Equations (1) and (2) contain 3 primary variables (*P, Q* and *A*) and thus one more equation is needed to close the system. This is given by the constitutive relation relating distending pressure, *P*, to local cross-sectional area, *A* (see subsection on Viscoelastic properties below). The formulation of the momentum equation (Equation 2) contains the convective acceleration term $\left(\frac{\partial}{\partial x}\int_A u^2 dA\right)$ as well as a wall friction term $\left(\tau=\mu\frac{\partial u}{\partial r}\Big|_{r=R}\right)$, both of which depend on the local velocity profile, which is *a priori* unknown. Approximations to these two terms using the Witzig-Womersley pulsatile theory are discussed below.

Viscoelastic properties of the arterial wall

The arterial wall behavior is non-linear (elastic modulus depends on distention) and viscoelastic. Following Holenstein et al. (Holenstein, Niederer et al. 1980), we assume that the arterial lumen area at a given location is the sum of a nonlinear elastic, A^e, and viscoelastic, A^v, component, respectively.

$$A(t)=A^e(P(t))+A^v(t) \qquad (3)$$

The elastic component of the local area A^e is related to instantaneous distending pressure, *P*, via the local area compliance C_A^e. The latter is a function of distending pressure but also a function of location. To account for both pressure and location dependence, we assumed that area compliance is the product of a pressure-dependent function, $C_p^e(p)$ and a location-dependant function $C_d^e(\bar{d},p_{ref})$, such that

$$C_A^e(\bar{d},P)=C_d^e(\bar{d},P_{ref})\cdot C_p^e(P) \qquad (4)$$

$C_d^e(\bar{d},P_{ref})$ gives the compliance for a given local mean lumen diameter, $\bar{d}$, and at a given reference pressure value, here taken as $P_{ref}=100mmHg$. In general, the arterial lumen diameter decreases as we move from the heart towards the periphery and this decrease is accompanied by a decrease in local area compliance, therefore there is good ground to propose a general $C_d^e(\bar{d},P_{ref})$

function for all arterial segments. The pressure dependency of the compliance in thoracic and abdominal aortas was measured and determined by (Langewouters 1982) to be

$$C_p^e(P) = a_1 + \frac{b_1}{1 + \left[\frac{P - P_{\max C}}{P_{width}} \right]^2} \quad (5)$$

with a_1=0.4, b_1=5, P_{maxC} = 20 (mmHg), P_{width} = 30 (mmHg) yielding a good functional fit. These parameter values are retained for the entire arterial tree, assuming that the functional dependence of local area compliance on pressure is approximately the same in all arterial locations.

Most published data in the literature provide for estimates of local pulse wave velocity (PWV) rather than compliance. We therefore derive the values of compliance at reference pressure from PWV values using the relation:

$$C_d^e(\bar{d}, P_{ref}) = \frac{A}{\rho \, PWV^{\,2}(\bar{d}, P_{ref})} \quad (6)$$

Reported values of PWV in the literature will be represented as a function of the mean arterial lumen diameter to deduce a global empirical relationship based on which compliance at every arterial location will be derived (see subsection "Physiological data" below). To include the viscoelastic component, the model developed by Holenstein et al. (Holenstein, Niederer et al. 1980) is implemented. The viscoelastic behavior is given by the convolution product between the elastic area A^e and the derivative of a creep function J(t).

$$A^v(t) = \int_0^\infty \dot{J}(\tau) A^e(P(t-\tau)) d\tau \quad (7)$$

$$\dot{J}(\tau) = \tilde{a} \frac{e^{-t/\tau_2} - e^{-t/\tau_1}}{t} \quad (8)$$

In Holenstein et al. the values $\tau_1 \cong 0.00081$s, $\tau_2 \cong 0.41$s were derived from the published data by Bergel (Bergel 1961). Furthermore, based on Bergel's data for the thoracic aorta, abdominal aorta and femoral artery, we may assume that the viscoelastic coefficient, $\tilde{a}$, increases linearly as the diameter decreases from heart to periphery. We may thus write

$$\tilde{a} \cong a_3 \cdot \bar{d} + b_3 \quad (9)$$

Considering the elastic and viscoelastic arterial wall components (Equation 3), the continuity equation (Equation 1) is rewritten in the following form:

$$\frac{\partial P}{\partial t} = -\frac{1}{C_A^e} \left[\frac{\partial A^v}{\partial t} + \frac{\partial Q}{\partial x} \right] \quad (10)$$

Wall shear stress and convective acceleration term

Both convective acceleration and wall shear stress depend on the instantaneous velocity profile, which is a priori unknown in the 1D formulation. Approximations need to be made. Earlier studies have used a number of different approaches for the two terms (see Table 1). Our approach is to use the Witzig-Womersley theory to model as best as possible the pulsatile effects on the velocity profile. Because the Witzig-Womersley theory is obtained in the frequency domain, this requires the knowledge of the local flow waveform over the entire heart cycle. To overcome this inherent difficulty, we assume that the solution is periodic and we use the flow waveform from the previous heart cycle to calculate the velocity profile and the wall shear stress using the relations:

$$u(r,t) = \frac{2}{\pi R^2}\left(1-\frac{r^2}{R^2}\right)Q_1 + \sum_n Re\left\{\frac{Q_n}{\pi R^2}\frac{1-\frac{J_0\left(\alpha i^{3/2}\, r/R\right)}{J_0\left(\alpha i^{3/2}\right)}}{1-\frac{2J_1\left(\alpha i^{3/2}\right)}{\alpha i^{3/2} J_0\left(\alpha i^{3/2}\right)}}e^{i\omega t}\right\} \quad (11)$$

$$\tau_w(t) = -\frac{4\mu}{\pi R^3}Q_1 + \sum_n Re\left\{\frac{\mu}{\pi R^3}Q_n \alpha i^{3/2}\frac{J_1(\alpha i^{3/2})}{J_0(\alpha i^{3/2})}\frac{1}{1-\frac{2J_1(\alpha i^{3/2})}{\alpha i^{3/2} J_0(\alpha i^{3/2})}}e^{iwt}\right\} \quad (12)$$

We solve in time over a number of repeating cycles till convergence. $\bar{Q}$ is mean flow, $Q_n(z,t)$ is the n^{th} harmonic of the flow pulse and J_0 and J_1 are the complex Bessel functions of first kind and of zero and first order, respectively. In equations (11, 12) the artery radius R is assumed constant and equal to the local radius at mean arterial pressure. α_i is the Womersley number for each harmonic defined as $\alpha_i = R\left(\rho 2\pi f_i / \mu\right)^{1/2}$, f_i being the frequency of the i^{th} harmonic.

Distal vasculature models and boundary conditions at termination sites

Peripheral arterial segments are terminated with a 3-element Windkessel (WK3) model, which accounts for the cumulative effects of all distal vessels (small arteries, arterioles and capillaries) beyond a terminal site. The WK3 model accounts for the proximal resistance (R_1), compliance (C_T) and distal resistance (R_2) of the vascular bed. The relation between pressure and flow in the time domain constitutes the distal boundary conditions and is expressed in differential form as:

$$\frac{\partial Q}{\partial t} = \frac{1}{R_1}\frac{\partial P}{\partial t} + \frac{P}{R_1 R_2 C_T} - \left(1+\frac{R_1}{R_2}\right)\frac{Q}{R_1 C_T} \quad (13)$$

Total peripheral resistances $R_T = R_1+R_2$ are estimated based on measured mean flow distribution in the major arterial beds (see Section on Blood flow rate quantification below). For terminal arterial segments where flow rate is not measured or available, we completed the values assuming that the mean WSS (given by Poiseuille's law) is the same as for nearby arteries. In order to define the values of the proximal (R_1) and distal (R_2) resistances, we further assume that the wave reflections at terminal sites vanish at high frequencies. A reflection coefficient at the distal interface is defined as

$$\Gamma(f) = \frac{Z_T(f) - Z_C}{Z_T(f) + Z_C} \quad (14)$$

where $Z_C = \rho \cdot PWV/A$ is the characteristic impedance of the last arterial segment proximal to the terminal WK3. Reflections at high frequencies vanish when $Z_C = |Z_T|$. At high frequencies, the modulus of the WK3 tends towards the value of its equal to its proximal resistance ($|Z_T| = R_1$). Hence, the condition for minimal reflection at high frequencies is $R_1 = Z_C$. Distal resistance is then obtained as $R_2 = R_T - R_1$. In the case of the present arterial tree, the minimal reflection at high frequencies implies that the ratio R_1/R_T varies in the range of [0.05-0.4], as compared to a fixed value of 0.2 arbitrarily chosen in previous studies (Raines, Jaffrin et al. 1974; Stergiopulos, Young et al. 1992). To respect the continuity in elastic properties of the terminal vessels, the Windkessel

compliance, C_{Ti}, is assumed to be proportional to the area compliance, C_A^i, of the terminal vessel at its distal end:

$$C_T^i \cong C_T \frac{C_A^i}{\sum C_A^i} \quad (15)$$

where $C_T = \sum_i C_T^i$ is the part of the total volume compliance attributed to peripheral vessels beyond the termination sites.

Arterial bifurcations

We impose continuity of pressure and flow across each branching point, neglecting thus any minor pressure losses occurring in the vicinity of the bifurcation. Earlier wave reflection analysis on the original Noordergraaf/Westerhof tree (Westerhof, Bosman et al. 1969), subsequently modified by Stergiopulos et al. (Stergiopulos, Young et al. 1992), has shown that significant non-physiological reflections arise in the aorta, and this is primarily due to rather high reflection coefficients at various bifurcations along the aorta (F. Merenda, unpublished observations). Papageorgiou et al. (Papageorgiou, Jones et al. 1990) studied wave reflections along the aorta and concluded that the main arterial junctions are well matched for minimizing forward wave's reflections. The forward wave reflection coefficient at an arterial bifurcation is given by:

$$\Gamma = \frac{Z_{up-stream}^{-1} - \sum Z_{down-stream}^{-1}}{Z_{up-stream}^{-1} + \sum Z_{down-stream}^{-1}} \quad (16)$$

where Z is the characteristic impedance of the upstream and downstream vessels. To minimize forward wave reflections, we chose to adapt the characteristic impedance of the downstream branches, so that the absolute value of the reflection coefficient given by Equation 16 is always lower than 0.1. This is achieved by slightly adjusting the cross sectional area of the daughter branches, while keeping the arterial wall distensibility unchanged.

Heart model

At its proximal end (root of the ascending aorta), the arterial tree is coupled to a model of the left ventricle (LV). The LV is modeled using the varying elastance model (VEM), as suggested by (Sagawa 1988). VEM is based on the time varying elastance (E(t)) of the left ventricle, which describes the variation of LV pressure (P_{LV}) and volume (V_{LV}) during a cardiac cycle:

$$E(t) = \frac{P_{LV}(t)}{V_{LV}(t) - V_0} \quad (17)$$

where V_0 is the dead volume of the LV (Figure 1A). Figure 1A also shows the four phases of the cardiac cycle, and it is to be noted that under physiological conditions (no leaky valves), only during ejection (phase II on Figure 1A) there is interaction between the LV and the arterial tree. Figure 1B shows the normalized varying elastance curve for one heart cycle. According to Senzaki et al. (Senzaki, Chen et al. 1996), the normalized varying elastance curve is relatively invariable in young and old subjects and is relatively unaffected by various forms of disease. Hence, the varying elastance curve for any individual is fully determined by only three cardiac parameters, i.e., the maximal elastance (Emax), the minimal elastance (Emin) and the time to maximum elastance (t_{max}).

During ejection, the aortic valve is open and thus reflected waves traveling backwards in the aorta will be reflected according to the impedance mismatch between the proximal aorta and the left ventricle. Earlier studies have pointed out that modeling the ventricle as a purely compliant chamber yields non-physiological wave reflection for the backward running waves (Campbell, Ringo et al. 1982; Shroff, Janicki et al. 1985) and suggested the introduction of an internal LV resistance in series to its compliance to improve the wave reflection characteristics of the left ventricle. The internal resistance R_{int} was introduced to explain, phenomenologically, the observed difference in the ventricular pressure of an ejecting heart (P_{LV}) and the ventricular pressure during an isovolumic contraction P^*_{LV} (Figure 1B). Hence, in an ejecting heart ventricular pressure is equal to P^*_{LV} minus the pressure drop over the internal resistance:

$$P_{LV} = P^*_{LV} - R_{int}(t)Q(t) \quad (18)$$

Experimental evidence showed that internal resistance is itself proportional to P^*_{LV}, so that

$$R_{int}(t) = \kappa P^*_{LV} \quad (19)$$

Taking the above into consideration, we derive the following expression for the varying elastance of an ejecting heart:

$$E(t) = E^*(t)\left[1 - \kappa Q(t)\right] \quad (20)$$

where E^* represents the elastance that would be measured during an isovolumic (non-ejecting) contraction. Equation (20) allowed us to reconstruct a normalized isovolumic elastance E^* from the normalized elastance curves (E) reported by (Senzaki, Chen et al. 1996) (Figure 1B) and from aortic flow waves measured in vivo (see Physiological data – Heart model).

Coronary model

Main coronary arteries are modeled assuming a systolic flow impediment which is proportional to the varying elastance. The coronary vessel diameter and compliance are affected by the contraction of the myocardium. Epicardial vessels are affected differently from endocardial and sub-endocardial vessels, but for the sake of simplicity, we follow here the approach of Vis et al. (Vis, Sipkema et al. 1995) and assume that compliance and resistance changes are proportional to the local time varying elastance of each vessel, which, according to (Krams, Sipkema et al. 1989), is assumed to have the same wave shape as the varying elastance of the left ventricle. Hence, we may express the contraction-induced changes in vessel wall distensibility (D_w) and terminal Windkessel properties (R_1, R_2 and C_T) as follows:

$$\begin{aligned} D_w\left(E(t)\right) &\approx D_w^{ref} - \varepsilon D_w^{ref} E(t) / E_{max} \\ C_T\left(E(t)\right) &\approx C_T^{ref} - \alpha C_T^{ref} E(t) / E_{max} \\ R_1\left(E(t)\right) &\approx R_1 + \beta R_1 E(t) / E_{max} \\ R_2 &\approx \delta R_2 \end{aligned} \quad (21)$$

where ε, α, β, δ are constants of proportionality. These relations are applied to the left coronary arteries. For the right coronaries, we assume that the effect of the right ventricle (RV) contraction is smaller by a factor proportional to the ratio of maximal pressure in the two ventricles, taken as $P_{LV,\max} / P_{RV,\max} \approx 6$.

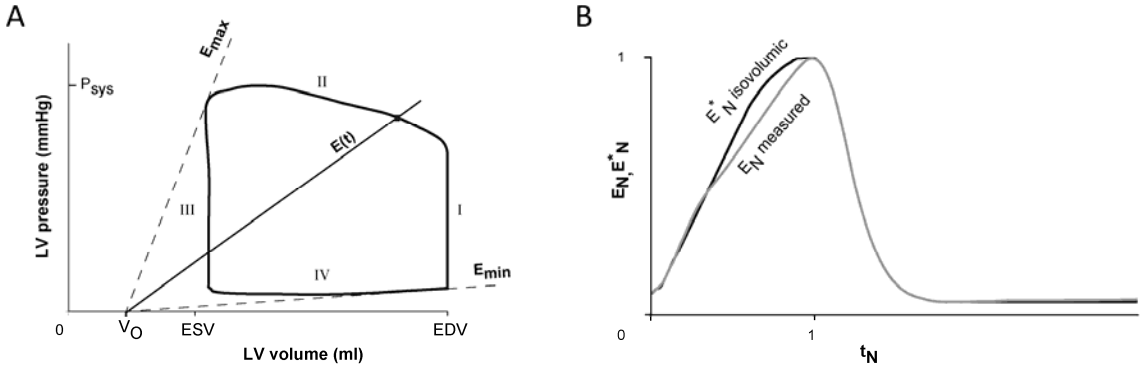

Figure 1. (A) A heart cycle represented as a ventricular pressure-volume graph. Instantaneous elastance, maximum elastance (E_{max}) and minimal elastance (E_{min}) are represented as well. E_{max} intersects the LV volume axis at the dead volume abscissa (V_0). (B) Normalized time varying elastance as function of normalized time.

Numerical solution

The set of equations with the boundary conditions described above are solved using an implicit finite difference scheme to yield pressure and flow waveforms over the entire arterial tree. Nonlinear terms are iteratively solved at each time step using the Newton-Raphson method. We initialize the arterial with an arbitrary pressure of 100 mmHg and a flow of 1 ml/s in each artery, the solution being quite insensitive to initial distribution of pressure and flow and always converging. Our convergence criterion is based on the maximum relative difference of 1% in pressure and flow between two consecutives cardiac cycles for all nodes and all time steps within the cardiac cycle.

PHYSIOLOGICAL DATA

Geometry

The arterial tree dimensions are based on the original Noordergraaf tree (Noordergraaf 1956), which was later adapted by Westerhof et al. (Westerhof, Bosman et al. 1969) and by Stergiopulos et al. (Stergiopulos, Young et al. 1992) (Figure 2A). Because the Stergiopulos et al. tree did not provide for a detailed description of the cerebral circulation, we added the main afferent and efferent vessels in the vicinity of the circle of Willis (CoW), as shown in Figure 2D. The considered CoW is assumed to be complete, although representative of only (42%) of the population (Krabbe-Hartkamp, van der Grond et al. 1998) due to significant anatomical variations from subject to subject. Geometry of the main cerebral arteries was obtained from averaged literature data (Table 2) and completed by real patient scans (3DRA and MRA). Many extracranial arteries, such as the superficial temporal arteries have also been added, in order to include points where pressure can be measured non invasively (tonometry), which is required for the validation phase of the work. The secondary anastomoses, such as the internal-external carotid, subclavian-carotid and subclavian-vertebral are not considered.

The Stergiopulos et al. arterial tree model did not include the coronaries. Because the coronary circulation is particular and perhaps not well adapted to the 1D model description, we decided to limit ourselves only to simplified description of the coronary tree, where only the main coronary arteries are included (Figure 2B).

Blood rheological invariable parameters in the current study are: ρ=1050 (kg/m^3) and μ=0.004 (Pa s). We assume impermeable arterial wall (ψ=0).

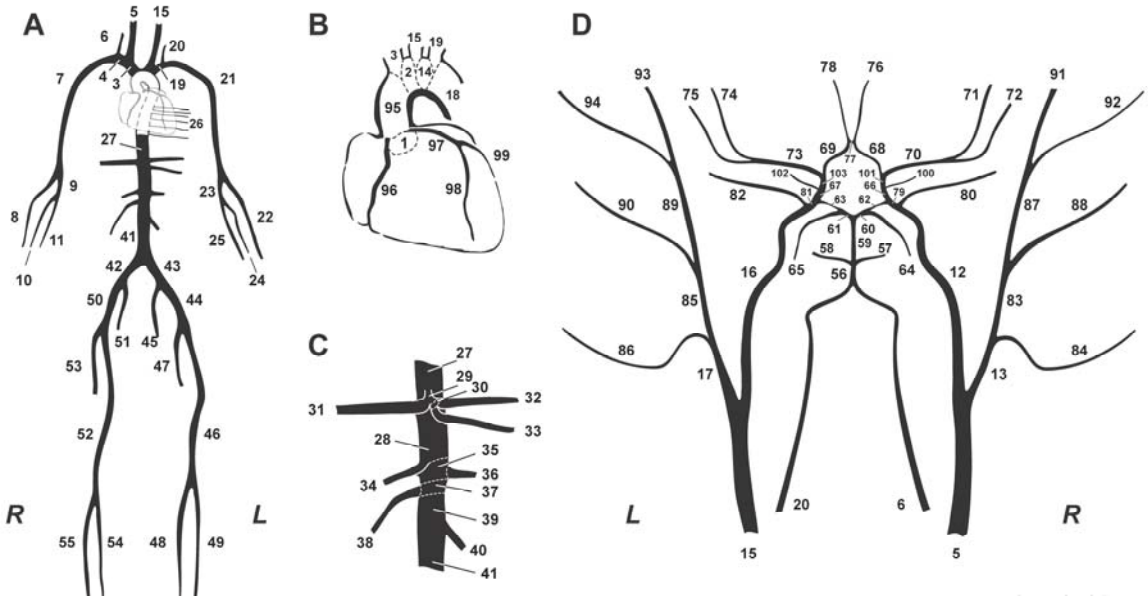

Figure 2. Schematic representation of the arterial tree.
(A) Main systemic arterial tree, based on the model of Stergiopulos et al (Stergiopulos, Young et al. 1992).
(B) Detail of the aortic arch and the coronary network.
(C) Detail of the principal abdominal aorta branches.
(D) Blown-up schematic of the detailed cerebral arterial tree, which is connected via the carotids (segments 5 and 15) and the vertebrals (segments 6 and 20) to the main arterial tree shown in (A)

Elastic properties

Values of PWV reported in the literature for different arteries as a function of the mean arterial lumen diameter are presented in Fig. 3. We observe that, despite some well-anticipated dispersion, there is a general trend of an inverse global relation between artery size and PWV. To that effect, we fitted an empirical inverse power curve:

$$PWV\,(\bar{d}) \approx \frac{a_2}{\bar{d}^{b_2}} \tag{22}$$

This simple empirical relation seems to be sufficiently well adapted, especially for large arteries with a lumen diameter greater than 5 mm. For smaller arteries, encountered for instance in the vicinity of the circle of Willis, it seems to underestimate the PWV. The coefficients obtained from the best fit are $a_2 = 13.3$, $b_2 = 0.3$, with $R^2 = 0.6$.
For intracranial arteries that are surrounded by the cerebrospinal fluid (CSF), we assume that the CSF mean pressure is of 15 mmHg and acts on the outer surface of the arterial wall. This implies that the distending pressure, which is lumen pressure minus external pressure, is decreased and thus the arterial wall compliance is increased (Equation 5).

Table 2. Geometry, distensibility, viscoelastic properties and peripheral resistances and compliances of the arterial tree

Arterial segment name	Arterial segment number (Right/Left)	Arterial segment length (mm)	Proximal lumen diameter (mm)	Distal lumen diameter (mm)	Distensibility (Dw) (10^{-3} 1/mmHg)	Viscoelasticity coeff. (a)	Terminal resistance ($R_1 + R_2$) (mmHg s/ml)	Terminal compliance (R_T) 10-5 (ml/mmHg)
Ascending Aorta 1	1	5	29.4	29.3	5.46	0.05		
Aortic Arch A	2	20	25.1	24.0	4.90	0.05		
Brachiocephalic	3	34	20.2	18.0	4.22	0.05		
Subclavian A	4/19	34	11.5/11.0	9.0/8.5	2.90/2.81	0.09/0.10		
Common Carotid	5/15	94/139 (§[b])	13.5/12.0	7.0/6.0 (*[b])	2.93/2.68	0.09/0.10		
Vertebral	6/20	149/148	3.7 (*[c]) (§[a]) (†[c])	2.8 (‡[a])	1.46	0.14		
Subclavian B, Axillary, Brachial	7/21	422	8.1	4.7	2.19	0.12		
Radial	8/22	235	3.7/3.5	3.1/2.8	1.49/1.43	0.14	39.7	702.9
Ulnar A	9/23	67	3.7/4.3	3.4/4.3	1.53/1.72	0.14/0.13		
Interosseous	10/24	79	2.1/1.8	1.8	1.08/1.03	0.14/0.15	633.8	44.0
Ulnar B	11/25	171	3.2/4.1	2.8/3.7	1.39/1.62	0.14/0.13	39.7	702.9
Internal Carotid	12/16	178	5.7/5.3 (*[c]) (§[a]) (†[c])	4.3/4.1 (*[c]) (‡[a])	1.89/1.82	0.13		
External Carotid 1	13/17	41 (§[b])	5.0/4.7	4.5/4.3	1.83/1.77	0.13		
Aortic Arch B	14	39	21.4	20.8	4.48	0.05		
Thoracic Aorta A	18	52	20.0	18.9	4.26	0.05		
Intercostals	26	80	12.6	9.5	3.04	0.09	10.5	2670.1
Thoracic Aorta B	27	104	16.5	12.9	3.60	0.07		
Abdominal Aorta A	28	53	12.2	12.2	3.22	0.08		
Celiac A	29	20	7.8	6.9	2.38	0.11		
Celiac B	30	20	5.2	4.9	1.90	0.13		
Hepatic	31	66	5.4	4.4	1.87	0.13	27.3	1022.5
Gastric	32	71	3.2	3.0	1.42	0.14	40.7	686.1
Splenic	33	63	4.2	3.9	1.66	0.13	17.4	1599.8
Superior Mesenteric	34	59	7.9	7.1	2.41	0.11	7.0	3991.0
Abdominal Aorta B	35	20	11.5	11.3	3.09	0.09		
Renal	36/38	32	5.2	5.2	1.93	0.12	8.5	3284.6
Abdominal Aorta C	37	20	11.8	11.8	3.16	0.08		
Abdominal Aorta D	39	106	11.6	11.0	3.07	0.09		
Inferior Mesenteric	40	50	4.7	3.2	1.64	0.13	51.7	539.5
Abdominal Aorta E	41	20	10.8	10.4	2.96	0.09		
Common Iliac	42/43	59	7.9	7.0	2.39	0.11		
External Iliac	44/50	144	6.4	6.1	2.15	0.12		
Inner Iliac	45/51	50	4.0	4.0	1.65	0.13	59.7	467.7
Femoral	46/52	443	5.2	3.8	1.77	0.13		
Deep Femoral	47/53	126	4.0	3.7	1.61	0.13	35.9	778.1
Posterior Tibial	48/54	321	3.1	2.8	1.38	0.14	35.9	778.1
Anterior Tibial	49/55	343	2.6	2.3	1.24	0.14	42.0	664.0
Basilar Artery 2	56	20	4.0 (§[a]) (†[c])	3.6	1.60	0.31		
Superior Cerebellar	57/58	10	1.7 (†[c])	1.4	0.93	0.33	200.8	3.6
Basilar Artery 1	59	5	3.1 (†[b])	2.7	1.36	0.32		
Post. Cerebral 1	60/61	2	1.9 (§[a]) (‡[a]) (†[c]) (†[b])	1.9	1.05	0.33		
Post. Communicating	62/63	4	1.2 (‡[a]) (†[c]) (†[b])	1.2	0.78	0.33		
Post. Cerebral 2	64/65	59	2.0(†[b])	1.8	1.12	0.32	80.5	5.8
ICA distal PCo – Ant. Chor. seg.	66/67	2	3.9	3.8	1.62	0.31		
Ant. Cerebral 1	68/69	12	2.1 (§[b]) (§[a]) (‡[a]) (†[c]) (†[b])	2.0	1.10	0.32		
Middle Cerebral M1	70/73	8	3.0 (‡[a]) (†[c]) (†[b])	2.8	1.36	0.32		
MCA M2 Sup. Br. Dist Sylvian bif	71/74	71	2.0	1.0	0.92	0.33	75.2	2.8
MCA M2 Inf. Br. Dist Sylvian bif	72/75	70	2.0	1.0	0.92	0.33	75.2	2.8
Ant. Cerebral A2	76/78	24	1.8	1.7	0.99	0.33	80.5	4.7
Ant. Communicating	77	2	1.3 (*[c]) (†[c]) (†[b])	1.3	0.84	0.33		
Int. Car. sinus	79/81	11	4.3	3.9	1.67	0.31		
Ophthalmic	80/82	11	1.0 (*[c])	0.5	0.60	0.33	200.8	0.4
External Carotid 2	83/85	61	4.0	3.5	1.59	0.13		
Sup Thy Asc Ph Lyng Fac Occ	84/86	101	2.0	1.0	0.92	0.15	225.6	5.9
Superficial Temporal	87/89	61	3.2	3.0	1.42	0.14		
Maxillary	88/90	91	2.2	1.0	0.95	0.15	188.0	5.0
Superficial Temporal Frontal Br.	91/93	100	2.2	1.4	1.02	0.15	188.0	8.2
Superficial Temporal Parietal Br.	92/94	101	2.2	1.4	1.02	0.15	188.0	7.6
Ascending Aorta 2	95	35	29.3	28.8	5.42	0.05		
R Coronary RCA	96	53.7(‡[b])	3.6 (*[a])	2.6 (*[a])	1.42	0.14	55.6	26.6
L Main Coronary LCA	97	5 (†[a])	4.9	4.7	1.84	0.13		
L Anterior Descending Cor. LAD	98	47 (‡[b])	3.8 (*[a])	1.5 (*[a])	1.29	0.14	45.1	26.6
L Circumflex LCx	99	26 (‡[b])	3.5 (*[a])	3.1 (*[a])	1.47	0.14	45.1	26.6
Ant. Choroidal	100/102	36	1.5	1.3	0.88	0.15	150.4	15.4

ICA distal Ant. Chor. - M1 seg.	101/103	2	3.8	3.8	1.61	0.13

Given arterial wall distensibility and lumen radius are assumed values for a reference transmural pressure of 100 mmHg.
(*a) Dodge, Brown et al. (Dodge, Brown et al. 1992), (†a) Fox, Davies et al. (Fox, Davies et al. 1973), (‡a) Gabrielsen and Greitz (Gabrielsen and Greitz 1970), (§a) Hillen, Hoogstraten et al. (Hillen, Hoogstraten et al. 1986), (*b) Holdsworth, Norley et al. (Holdsworth, Norley et al. 1999), (†b) Krabbe-Hartkamp, van der Grond et al. (Krabbe-Hartkamp, van der Grond et al. 1998), (‡b) Pennell, Keegan et al. (Pennell, Keegan et al. 1993), (§b) Krayenbuehl and Yasargil (Krayenbuehl and Yasargil 1982), (*c) Yasargil (Yasargil 1984), (†c) Data from G. P. B. Wollschlaeger summarized by Yasargil (Yasargil 1984).

Viscoelastic properties

The linear viscoelastic coefficient, $\tilde{a}$, was obtained by fitting Equation 9 on the viscoelasticity data reported by (Bergel 1961). The best-fit yielded a_3 = - 0.0062 (mm^{-1}) and b_3 = 0.16 (R^2 = 0.90). For cerebral arteries, which present a much stronger viscoelastic component (Bergel et al.) (Bergel 1961), only one point that corresponds to the carotid artery was available, therefore we assumed same slope (a_3) as for the other arteries, however the parameter b_3 was taken as b_3 = 0.34 to match the carotid viscoelasticity value.

Vascular resistance and compliance

Peripheral resistances were based on data by Stergiopulos et al. (Stergiopulos, Young et al. 1992). For the cerebral circulation, which was not included in the Stergiopulos et al. model, we derived peripheral resistances from mean flow data published in the literature or from our own flow measurements (Table 3).

The total systemic vascular compliance is the sum of the volume compliances of all vessels including also the compliance of the terminal beds, so that $C_v = \sum_i^n C_{v,i} + \sum_i^m C_{T,i}$, where n=103 is the number of arterial segments and m=47 is the number of terminal beds. The volume compliance of each arterial segment is obtained by integrating the area compliance (Equation 5) over the segment length. Volume compliances were finally adjusted so that the total systemic compliance matches literature values for a typical young healthy subject of the same age as the average age of our subject group. More than 50% of the total arterial compliance is in the aorta (Ioannou, Stergiopulos et al. 2003), and thus only a minor part is attributed to peripheral beds. We here follow Stergiopulos et al. and assume that the sum of compliances of the terminal beds is in the order of 20% of the total systemic compliance.

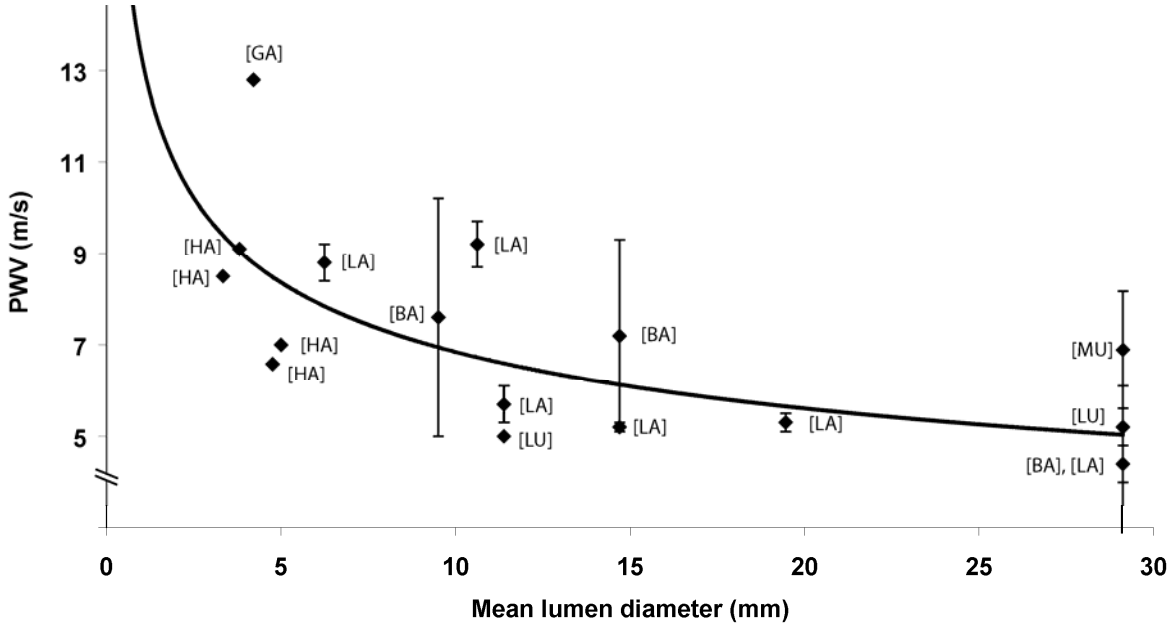

Figure 3. Pulse wave velocity (PWV) reported in the literature for different arteries, plotted as a function of the arterial lumen diameter. Acronyms refer to the publication from which the specific data points were extracted

(BA: Baguet, Kingwell et al. (Baguet, Kingwell et al. 2003); GA: Giller and Aaslid (Giller and Aaslid 1994); HA: Hayashi, Nagasawa et al. (Hayashi, Nagasawa et al. 1980); LA: Latham, Westerhof et al (Latham, Westerhof et al. 1985); LU: Luchsinger, Snell et al. (Luchsinger, Snell et al. 1964); MU: Murgo, Westerhof et al. (Murgo, Westerhof et al. 1980). Only available SD are shown.

Table 3. Mean flow rate for different cerebral arteries from literature and own measurements.

References	Modality	Age	CCA Left / Right	ICA Left / Right	ECA Left / Right	MCA Left / Right	ACA Left / Right	PCA Left / Right	VA Left / Right	BA	CBF
Enzmann, Ross et al. (Enzmann, Ross et al. 1994)	cine PC-MR	22-38				1.8 / 2.1	1.25 / 1.47	0.88 / 0.85		2.68	
Buijs, Krabbe-Hartkamp et al. (Buijs, Krabbe-Hartkamp et al. 1998)	ug 2D PC-MRA	19-29		5.1 / 4.9						2.53	12.5
Spilt, Box et al. (Spilt, Box et al. 2002)	PC-MRI	18-26 (2^{nd} gr.)									12.6
Scheel, Ruge et al. (Scheel, Ruge et al. 2000)	Color duplex	20-39									12.5
Holdsworth, Norley et al. (Holdsworth, Norley et al. 1999)	Doppler	24-34	6.0								
Stock, Wetzel et al. (Stock, Wetzel et al. 2000)	PC-MR	< 30				2.1 ± 0.5					
Marshall, Papathanasopoulou et al. (Marshall, Papathanasopoulou et al. 2004)	cine PC-MR	29 ± 7	6.16	4.14	1.59						
Obata, Shishido et al. (Obata, Shishido et al. 1996)	PC-MRI	18-65		3.8 ± 1.4/ 3.7 ± 1.0						2.37 ± 0.97	10.3 ± 2.1
Hillen, Hoogstraten et al (Hillen, Hoogstraten et al. 1986)	model †					2.78	1.39	2.08			
Ultrasound & TCCD		15-30	4.9 / 6.5	3.7 / 4.5	2.5 / 2.7	2.2	1.0		1.2	1.9	
Mean flow rate chosen ‡			6.0	4.5	1.5	2.5	1.25	1.0			12.5

† assuming that resistances are inversely proportional to irrigated brain mass. ‡ Averaged mean flow rate of the 1D model to set the distal WK3 resistances in the efferent vessels of the CoW.

Heart model

We derived isovolumic elastance (E^*, Equation 20) from the global normalized elastance curve (E) reported by Senzaki et al. (Senzaki, Chen et al. 1996) (Figure 1B). This required the use of a "standard" aortic flow waveform, which we obtained by averaging our own measurements with PC-MRI at the ascending aorta of a group of young volunteers (see subsection on In Vivo Measurements, below). The value of κ was derived by minimizing the difference between the resulting elastance of the 1D model run and the original one from Senzaki et al. (Senzaki, Chen et al. 1996). This yields κ = 0.0005 (s/ml).

The main parameters of the heart model were taken from a study by Merenda (Merenda 2003), who examined influence of each parameter on the waveforms in the ascending aorta. Heart parameters yielding physiologically relevant aortic pressure and flows for young adults pressure were in the following range: V_0= [-50, 300] ml, E_{min} = [0.03, 0.2] mmHg/ml, E_{max} = [1.0-6.0] mmHg/ml, end diastolic pressure $P_{END\text{-}DIA}$ = [5-25] mmHg and venous resistance R_{ven} = [0.001-0.003] mmHg s ml^{-1}. The reference values chosen for the present study were V_0=15 ml, E_{min} = 0.08 mmHg/ml, E_{max} = 2.6

mmHg/ml, $P_{END\text{-}DIA}$ = 14 mmHg (Senzaki, Chen et al. 1996) and the venous resistance R_{ven} = 0.003 mmHg s ml^{-1}. The heart rate (HR) is chosen to be 75 bpm, corresponding to average data for a 25 yrs old subject (Nichols, O'Rourke et al. 1985). The time to maximum elastance is set to t_{max} = 340 ms, this being the average value between our own measurements and those published by (Starling, Walsh et al. 1987), who reported a t_{max} range from 262 to 383 ms for subjects 36 to 60 years old.

In-vivo measurements

To validate the 1D model predictions, we performed noninvasive pressure and flow measurements in young healthy volunteers, aged 15-30 yrs old, at the Geneva University Hospital (HUG). The measurements were performed according to a protocol approved by the local ethics committee. Volume flow rate waveforms were obtained in a first group of patients in systemic arteries using gated phase contrast MRI (PC-MRI). In a second group of patients, flow was measured in precerebral and cerebral arteries using B-mode and color-coded duplex flow imaging. In a subgroup of this second group of patients, pressure waveforms were measured on superficial arteries using applanation tonometry. The foot of the end diastolic flow waveform was set as reference for time alignment of cardiac cycles for inter-volunteer data averaging.

Blood flow measurement using PC-MRI

2D PC-MRI sequences (slice thickness 6mm TE/TR 3.3/51.7 ms, flip angle 20°, FoV 220x320 mm, Siemens Trio-Tim 3T System) were acquired at 5 different large artery sites (Figure 4) on volunteers (n=6, male/female (4/2), age 28 $\pm$ 1.3 (mean $\pm$ SD), height = 178 ± 12 cm) at rest and in basal conditions. The measurements planes were determined using flash angiography images to ensure that the plane was perpendicular to the vessel axis.

For aortic measurements, breathold sequences were ran during 19 seconds to minimize movement artifacts. Twenty gated phase and magnitude images were acquired, gating being based on pressure pulse measured in the index finger. Arterial cross sections were manually segmented (Argus Flow software, Siemens) to follow lumen area changes over the heart cycle. Volume flow rate was the integral of the velocities across the lumen.

Blood flow measurement using Color-coded duplex ultrasound

Color-coded duplex flow imaging (CDFI) with a 5-8 MHz linear phase array and a 2-4 MHz sectorial transducer were used to assess blood flow velocities in the cerebral vasculature (Toshiba medical device, Aplio 80). CDFI was performed via the temporal, orbital and occipital acoustic bone windows. Insonation angle was close to 60°, except for the middle cerebral artery (MCA) where the angle was close to 0°. Diameter values of extracranial arteries were obtained using M-mode imaging. The subjects (n=8, male/female (4/4), age 26 $\pm$ 4) were measured at rest at basal conditions and in the supine position. Two subjects were not included, because their examination showed inconstant cardiac cycle periods.

Pressure measurements using applanation tonometry

Pressure waveforms over 10 heart cycles were acquired on distal radial artery, distal common carotid artery (CCA) and temporal arteries (Figures 4 and 5) with applanation tonometry (Millar Instruments, SPT 301, Houston, TX) on (n=5, male/female (3/2), age 29 $\pm$ 3), basal conditions, supine position). Pressure was calibrated with brachial pressure measured with a sphygmomanometer, based on the assumption that mean and diastolic pressures do not vary much between the brachial artery and the carotid, radial and temporal locations.

Mean sphygmomanometer pressure is calculated as $P_{mean} \cong P_{diastole}$ + 1/3 PP (Segers, Rietzschel et al. 2005), where PP is the pulse pressure (P_{sys}-P_{dia}).

RESULTS

Model predictions vs. in vivo measurements

PC-MRI flow measurements of flow in the main aortic segments (ascending aorta, thoracic aorta, abdominal aorta) and main lower limb arteries (common iliac and femoral artery) are shown in Figure 4 (upper panels). Figure 4F includes also pressure measurements in the radial artery. All pulses are plotted in their natural time scale. Model predictions at the same arterial sites are shown in the corresponding lower panels. We observe a good overall agreement in both amplitude and wave shape at all arterial locations. Comparison between predicted and measured maximal, minimal and mean flow is given in Table 4. Table 5 also gives the comparison for systolic, diastolic, mean and pulse pressure. The discrepancies are typically of 22 ± 16 % (mean $\pm$ SD) for peak systolic flow and 12 ± 11 % for mean flow, whereas they are 9 ± 6 % for systolic pressure and 12 ± 5 % for diastolic pressure.
Cerebral artery flow waveforms predicted by the model are compared to ultrasound measurements in the MCA, vertebral artery (VA), internal carotid artery (ICA) and CCA (Fig. 6). Pressure waveforms measured with applanation tonometry and compared to model predictions in the superficial temporal artery (Fig. 6B) and common carotid (Fig. 6F). As mentioned in the Methods section, cerebral blood flow measurements are based on pulsed Doppler data velocities and an "average" local vessel lumen diameter. This means that the absolute values for flow obtained experimentally may contain significant error, whereas the shape of the flow waveform is rather accurately captured by the Doppler ultrasound. Indeed, the similarity in the flow wave shape between model and measurements is quite evident (Figures 5A, C, D and E), with all primary and secondary wave shape features being captured quite well.

Table 4. Quantification of blood flow rate of in-vivo measurements and model results at different arteries

	Systolic flow rate (ml/s)		Diastolic flow rate (ml/s)		Mean flow rate (ml/s)	
	In-vivo	Model	In-vivo	Model	In-vivo	Model
Ascending aorta	470	420	0.5	-33	103	96
Thoracic aorta	303	235	-2.5	14	68	71
Abdominal aorta (§)	123	87	-21	-10	20	18
Iliac artery	38	34	-7.5	-2.4	7.5	7.8
Femoral artery	28	17	-5.7	-0.3	5.1	3.8
CCA	22	22	2.5	0.7	6.5	5.4
ICA	9.0	9.8	2.2	2.7	3.6	3.9
VA	2.4	2.9	0.8	0.8	1.2	1.2
MCA	3.9	2.7	1.7	1.5	2.5	1.9

§ at infra renal level

Effects of viscoelasticity, convective acceleration and wall friction formulation

Table 6 quantifies the effects of adding viscoelasticity, and applying Witzig-Womersley's theory to derive more accurate expressions of convective acceleration and wall shear stress. Differences in pressure and flow waveforms with respect to the "control" model are reported as the root mean square of the difference (RMS) over the entire heart cycle in 3 representatives arteries (thoracic aorta, common iliac artery and middle cerebral artery). As "control" model we take same 1D model but without viscoelastic effects and with Convective acceleration and wall shear stress being estimated using a quasi-steady parabolic profile. We observe that viscoelasticity as well as convective acceleration and wall friction impact in a significant manner on the flow waveform, in all three arterial sites. The impact on pressure is important only in the peripheral sites (common iliac and middle cerebral artery) but not in the aorta.

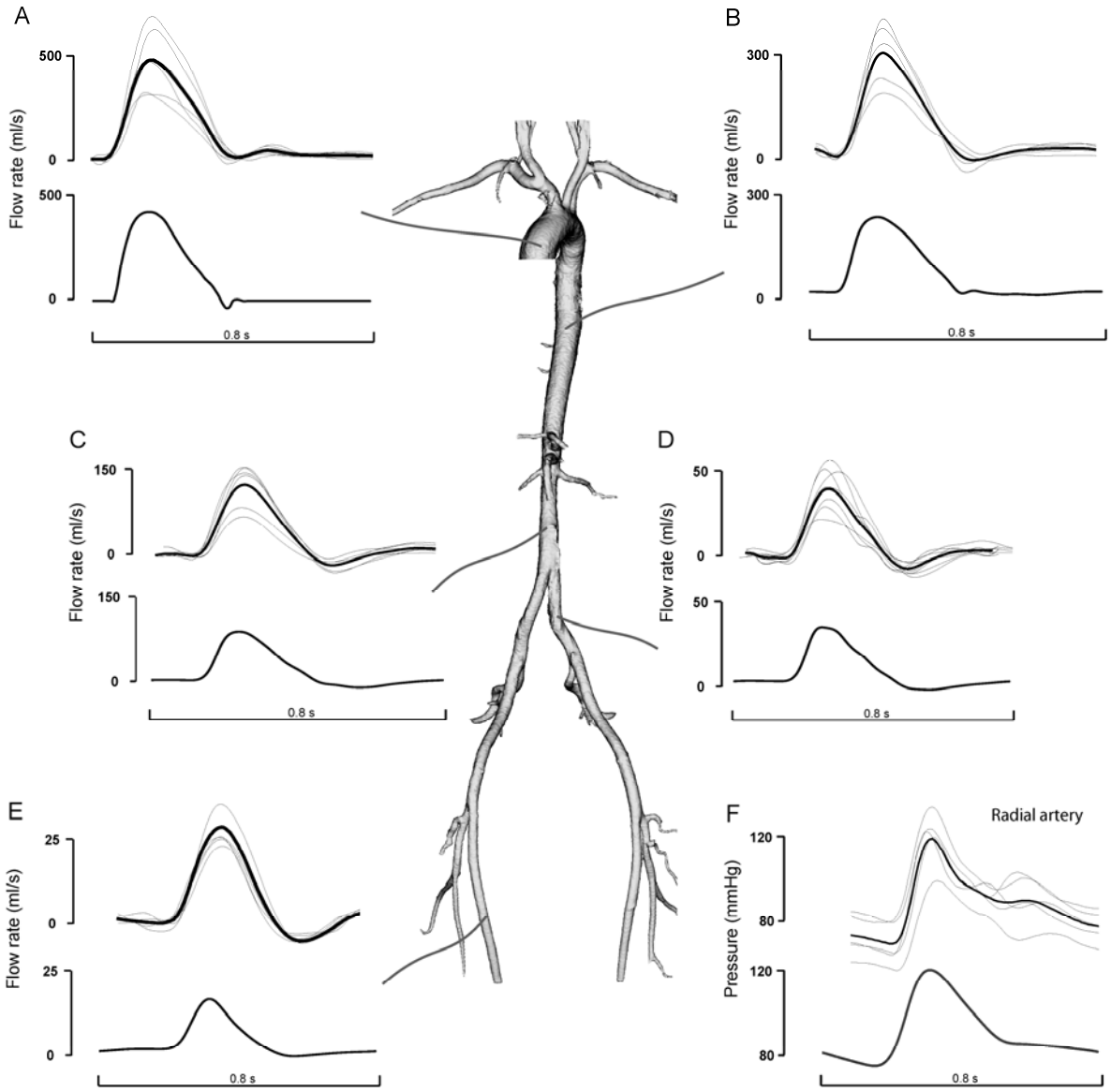

Figure 4. Model results (bottom panels) compared to in vivo measurements of flow and pressure waves (top panels) at various systemic arteries locations. Thick line represents the averaged waveform. The flow rate waveforms were not available due to poor quality measurements for volunteer 4 in (B), volunteer 1 in (D) and volunteers 5 and 6 in (D&E).

Table 5. Quantification of pressure of in-vivo measurements and model results at different arteries

	Systolic pressure (mmHg)		Diastolic pressure (mmHg)		Mean pressure (mmHg)		Pulse pressure (mmHg)	
	In-vivo measures	Model	In-vivo measures	Model	In-vivo measures	Model	In-vivo measures	Model
Radial artery	122	125	69	74	87	90	53	51
CCA	101	115	68	81	85	97	33	34
Superficial Temporal artery	106	119	71	79	87	96	35	40

Model predictions in presence of detailed cerebral circulation

To assess the importance of having a detailed description of the cerebral arterial tree, we examined the predicted pressure and flow waves at 2 arterial locations: the common carotid artery, which feeds into the cerebral circulation and thus susceptible to reflected waves coming back from the distal cerebral sites and the thoracic aorta, which is expected not to be directly affected by the cerebral vasculature. As a “control” we take a simple description of the cerebral tree as given in the model by Stergiopulos et al. (Fig. 2A). To preserve equivalence in terms of the global wave propagation and reflection properties, the distal sites of internal and external carotids and vertebral arteries of the “control” model were terminated by lumped 3-element Windkessel models (WK3) providing the same total terminal resistance and compliance as the detailed cerebral arterial tree model. The results are shown in Figure 4. We observe considerable differences in the carotid pressure and flow waveforms, the differences in flow being substantial in both amplitude and wave shape. We notice, in particular, that in presence of the detailed cerebral tree, the computed flow exhibits a physiological pulsatility and only forward flow throughout the heart cycle. In absence of the detailed cerebral tree, predicted common carotid flow exhibits an abnormally high pulsatility and a non-physiological backflow at the dicrotic notch (compare also with in vivo measurement on Figures 6).

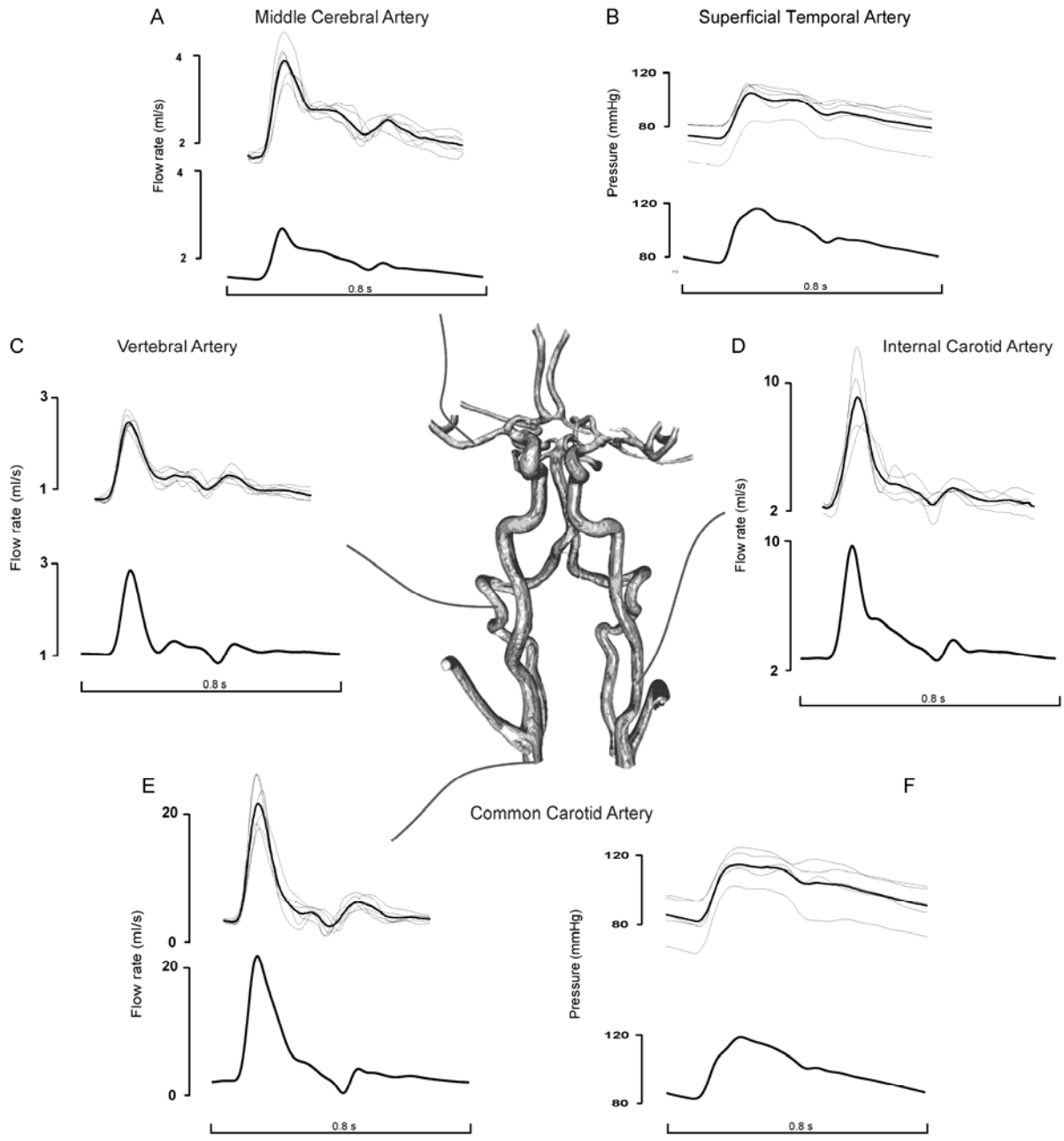

Figure 5. Model results (bottom panels) compared to in vivo measurements of flow and pressure waves (top panels) at various cerebral artery locations. Thick line represents the averaged waveform. Blood flow was measured with color-coded duplex ultrasound. Pressure was measured with applanation tonometry in the superficial temporal artery (B) and common carotid (F). Flow rate waveforms were not available due to poor quality measurements in one volunteer in (D).

DISCUSSION

This study aimed in achieving two goals. First, to improve the 1D model of Stergiopulos et al., which we have developed earlier (Stergiopulos, Young et al. 1992) and that we have successfully utilized as a research tool in a number of subsequent studies (Stergiopulos, Meister et al. 1994; Stergiopulos, Meister et al. 1995; Stergiopulos, Meister et al. 1995; Stergiopulos, Westerhof et al. 1998; Stergiopulos, Segers et al. 1999; Westerhof and Stergiopulos 2000). Second, to validate, at least in a semi-quantitative sense, the predictions of the 1D model with in vivo measurements of pressure and flow. The improvements were carried on at different levels. We included a heart model, we included a simple coronary model, we extended the cerebral circulation to include all major vessels, we added viscoelasticity onto the nonlinear elastic properties of vessel wall, and we improved the description of the convective acceleration and friction terms by employing the Witzig-Womersley theory. Our results showed that the implemented improvements were important, and in specific cases, such as the description of cerebral hemodynamics, essential. The validation was carried out by comparing our generic model predictions with average pressure and flow measured in a group of young subjects at different arterial locations. The validation was done by a quantitative comparison of systolic, diastolic and mean pressure and flow as well as by a qualitative comparison of the shape and features of pressure and flow waveforms. Despite its generic character, the 1D model provided with pressure flow predictions which faithfully reproduced the wave characteristics in all arterial locations and thus we conclude that the 1D model may very well be used as an efficient model for predicting pressure and flow wave propagation in the entire arterial tree.

Validation of the 1D model

A major driver for undertaking the present study was the lack of any previous validation of the 1D model prediction with *in vivo* data. One-dimensional models have been used for more than 30 years to predict or analyze pressure and flow in the arterial tree, but few studies performed a quantitative assessment of the validity of the 1D results. Such a quantitative assessment was performed *in vitro* in an elastic tube network dimensioned to resemble the human arterial tree by Matthys et al. (Matthys, Alastruey et al. 2007). The results were supportive of the 1D model's capacity to yield good predictions, however, neither the form of the waves nor the elastic properties of the in vitro tube network were matching faithfully their physiological counterparts, so the desire to validate the 1D model using *in vivo* measurements remained.

In vivo validation is a difficult task. The difficulty arises from the fact that a fully quantitative validation would require a "subject-specific" approach, where all parameters defining the 1D model (geometry, viscoelastic properties, peripheral impedances, varying elastance of the heart) are measured or estimated precisely on a specific subject. Only then, 1D model predictions at several arterial locations could be compared quantitatively with the in vivo measurements in the same person and the same locations. This is clearly a formidable, if not impossible task. We therefore opted for an alternate, less quantitative but easier to implement solution: perform measurements on a group of young individuals and obtain average pressure and flow waveforms at different arterial sites, which are then compared to the 1D model predictions. The logic behind our approach lies in that the 1D model is constructed based on literature values reflecting, to a certain extent, the average young adult. In that respect, the general 1D model may not reflect the characteristics of a single specific subject, but it should be, qualitatively at least, close to the average of a group of young subjects. The consequence of this approach is that the comparison can only be carried out by examining the qualitative characteristics of the pressure and flow waveforms, such as the wave shape at different arterial locations, rather than the absolute values of the pressure and flow waveform.

The qualitative comparison between the model predictions and measured pressure and flow waveforms is judged overall quite satisfactory. Results show us that the model is able to reproduce

the main aspects and features of physiological flow and pressure waveforms in large systemic arteries (Fig. 5) as well as in the arteries of the cerebral circulation (Fig. 6). In the aorta, model predictions have captured well the existence of a significant backflow in early diastole in the infrarenal region (Fig. 5C) and in the common iliac artery (Fig. 5D), a well-known feature which is also seen in our MRI measurements. Backflow is absent in the suprarenal aorta, a characteristic also present in the predicted flow waveforms. Comparisons are particularly interesting in the cerebral circulation, where flow waveforms are more complex and exhibit significant variations in their shape at different locations. We observe that the model captures quite well most of the qualitative wave shape features of flow in all cerebral sites. Measured flow waves in the common and internal carotid exhibit a sharp primary systolic peak followed by a second less pronounced peak in early diastole. Model predictions captured well these characteristics. Measured flow waves in the vertebral artery show a "3-peak structure", with a second shallow peak appearing in late systole. Again, model predictions show the same structure. Flow in the middle cerebral artery exhibits a characteristic plateau midway in the descending part of the systolic peak and this feature is well represented also in the flow predicted by the model. The same plateau appears also in the temporal pressure wave measured by tonometry in vivo and it is also present in the model predictions. There seems to be less good of an agreement in the shape of measured and predicted common carotid pressures, both shapes resembling a typical ascending aorta wave, which is expected by the proximity of the vessel to the aorta (Kelly, Hayward et al. 1989; McDonald, Nichols et al. 1990). Radial pressure waveform presents the same sharp peak at systole between the model and in vivo measurements, which is in accordance with data reported by (Kelly, Hayward et al. 1989; McDonald, Nichols et al. 1990). This feature is typical of person in the 2^{nd} to 4^{th} decade and different from elderly people, where increased and faster wave reflections occur at the end of systole.

Importance of viscoelasticity, convective acceleration and wall friction formulation

As seen in Table 1, very few of the previous models have introduced viscoelastic effects in their formulation. This is probably due to the fact that limited data are available on the viscoelastic properties of the human arterial wall. Yet, energy losses and damping effects due to wall viscoelasticity are of the same order magnitude as wall friction in large and medium size vessels. Table 6 shows that adding viscoelasticity leads to changes in the predicted pressure and flow in the order of a few percent in the thoracic aorta and this is consistent with previous finding (Segers et al) (Segers, Stergiopulos et al. 1997). The effects become more significant in the periphery, especially on the flow wave. We may thus conclude that viscoelastic effects maybe important, especially when fine details on peripheral sites are sought. The way we have modeled viscoelasticity is not unique and the data upon which we derived the viscoelastic properties of the entire arterial tree are from the classic study of Bergel (Bergel 1961), performed on a limited number of canine arteries. Hence, there is clearly a need for a consistent set of data derived from human subjects.

Table 6. Effect of viscoelasticity, wall shear stress and convective acceleration formulation on pressure and flow rate waveforms for 3 representative arterial sites.

			Thoracic aorta		Common iliac artery		Middle cerebral artery	
Visco-elasticity	wall shear stress *	convective acceleration *	Pressure (mmHg)	Flow rate (ml/s)	Pressure (mmHg)	Flow rate (ml/s)	Pressure (mmHg)	Flow rate (ml/s)
+	-	-	1.5 (1.5%)	4.0 (4.3%)	2.3 (2.4%)	1.4 (15%)	2.3 (2.4%)	0.09 (4.5%)
-	+	-	0.4 (0.4%)	4.0 (4.3%)	2.0 (2.1%)	1.5 (16%)	2.0 (2.1%)	0.09 (4.5%)
-	-	+	1.3 (1.3%)	11.3 (12%)	6.3 (6.6%)	4.4 (4.6%)	2.1 (2.2%)	0.07 (3.5%)
+	+	+	2.5 (2.5%)	11.1 (12%)	6.8 (7.2%)	4.8 (5.1%)	3.7 (3.9%)	0.11 (5.5%)

Reported data are difference between a "control" model using VEM but not considering viscoelasticity, improved wall shear stress and convective acceleration terms and models that consecutively consider viscoelasticity, wall shear stress and convective acceleration formulation.
Values are the root mean square (RMS) of the difference over the entire pressure or flow wave in absolute (relative to the reference model in %).
* Improved wall shear stress and convective acceleration terms from Witzig-Womersley theory

Our model is the only global arterial tree model that includes viscoelastic effects and nonlinear wall elasticity at the same time. Avolio (Avolio 1980) and Fitchet et al (Fitchett 1991) have developed models of the entire arterial tree including viscoelastic effects but have considered a linear constitutive relation for the arterial wall. The effects of nonlinearity have not been analyzed in detail here, because this has been done in detail earlier in the work of Segers et al (Segers, Stergiopulos et al. 1997). Segers et al. found that the RMS of difference in pressure between a linear and nonlinear model is in the order of 2% in the aorta to 3% in the brachial artery and to almost 9% in the femoral artery. The differences are thus more significant in peripheral arteries and of the same order as the viscoelastic effects.
Wall friction and convective acceleration terms were derived from Witzig-Womersley's theory. This is, of course, still a rough approximation, because it assumes straight, rigid tubes and developed flow. Entry effects, curvature, non-planar geometries and bifurcations would lead to substantial deviations from Witzig-Womersley's theory, with wall shear stress been rather underestimated in most cases. Witzig-Womersley's theory, constitutes, nevertheless, an improvement over the Poiseuille flow approximation, which often been used for estimating friction and the convective acceleration term (Table 1). We evaluated the difference it makes to use Witzig-Womersley's theory instead of simple quasi-static Poiseuille on predicted pressure and flow at different arterial locations and the results are presented in Table 6. With the exception of pressure in the thoracic aorta, the effects of replacing Poiseuille by Witzig-Womersley's theory on both the friction term and the convective acceleration term were significant, and of the same order of magnitude as the viscoelastic effects. We therefore conclude that, as for viscoelasticity, if details are sought, we should develop more precise ways of modeling the friction and convective acceleration terms. This may require developing semi-empirical models for taking into account non-developed flow and the effects of curvature, branching and non-planar geometries.

Cerebral circulation

With the exception of models specifically designed for studying wave propagation in the cerebral circulation (Kufahl and Clark 1985; Hillen, Hoogstraten et al. 1986; Alastruey, Parker et al. 2007), most of the other earlier 1D models included a very simplified representation of the cerebral circulation, with typically only the major proximal vessels (i.e., carotids and vertebrals) being included in the model (Table 1). We have hypothesized that the completeness of the cerebral circulation is necessary for obtaining accurate prediction of pressure and flow not only in the distal vessels and in the vicinity of the Circle of Willis, but also in the proximal major vessels (i.e., carotids and vertebrals). The rational for this hypothesis is that the distal cerebral arterial tree constitutes a complex arterial network with specific topological wave transmission and reflection properties, which will influence considerable pressure and flow in the entire cerebral circulation. The importance of a detailed cerebral arterial tree on wave reflections was first recognized by Avolio (1980). Our results indeed show that predicted wave shapes in the carotid artery are strongly affected by the presence of a detailed model of the distal cerebral circulation. This was clearly demonstrated in Figure 6, where the shape of the predicted common carotid pressure and flow is substantially different when the detailed cerebral arterial tree (Fig. 2D) is substituted by the simplistic one of Stergiopulos et al. (Figure 2A).

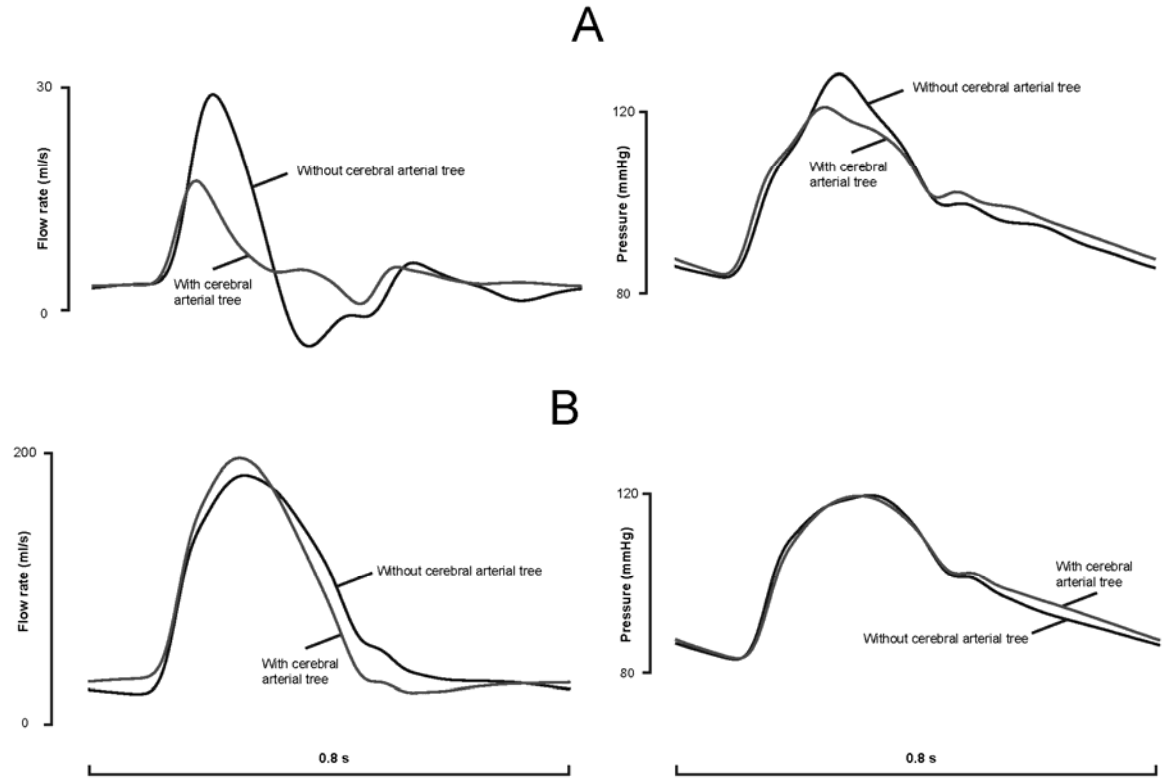

Figure 6. Pressure and flow waveform in the common carotid (A) and thoracic aorta (B) as predicted by the present one-dimensional model containing a detailed description of the cerebral circulation as well as by the model of Stergiopulos et al. (Stergiopulos, Young et al. 1992) containing only the major vessels feeding into the cerebral circulation.

The effects on the flow waveform are remarkable, despite the fact that the distal impedances at the termination points of the simple cerebral arterial tree model were carefully set to match the resistive and compliant characteristics of the detailed cerebral tree. Of particular importance is the enhanced pulsation, which exhibits the flow wave in absence of the detailed distal cerebral tree. The enhanced pulsation leads to negative flow in early diastole, a phenomenon clearly non-physiological, because we know from in vivo measurements that flow is purely unidirectional in the carotid. We attribute these effects to the enhanced, non-physiological wave reflection properties of the simplified cerebral tree, and in that respect we agree with Avolio (1980). We therefore conclude that a detailed cerebral arterial tree is necessary for obtaining accurate pressure and flows in the cerebral circulation, even in the major proximal cerebral vessels. On the other hand, the effects of the cerebral circulation in the aorta are, as expected, minimal (Fig. 4B). This means that, if the scope of the model is confined in all the other vessels of the systemic circulation and not concerned with cerebral blood flow, a detailed description of the cerebral circulation may not be necessary. We note, however, that abnormally high reflection coefficients in the main systemic arteries, such as those present in the original Noordergraaf-Westerhof model, lead to non-physiological waves along the aorta, manifested by the presence of excessive reflected waves and high augmentation index in the ascending aorta. The optimization of all reflection sites performed in the present model improved the wave reflection profile and led to physiological pressure waves in the aorta.

Heart model

Most of the previous 1D models of the arterial circulation used as proximal boundary conditions a prescribed pressure or flow wave. This is of course acceptable, however, it implies that the chosen

proximal wave corresponds to the particular state of the arterial tree. This is because the aortic pressure and flow wave are the results of the interaction of the heart and the arterial system and therefore any change in either the cardiac parameters (i.e., heart rate, contractility, filling, etc.) or the arterial parameters (i.e., resistance, compliance, etc.) would lead to changes in the aortic pressure and flow. Hence, the approach to describe pressure or flow as proximal boundary condition is very limiting, especially for performing parametric studies involving changes in the cardiac side, the arterial side or both. Using a heart model, as the varying elastance model employed here, allows for such flexibility. The resulting pressure and flow waves are physiological and compare well, as seen in Figures 4 and 5 with the measured waves. Although not in the scope of the present study and thus not presented in this work, we have performed a number of parametric studies, where we varied cardiac and arterial parameters and we obtained reasonable pressure and flow predictions, reinforcing thus the general applicability of the heart model. Additional studies are required to further validate the heart-arterial system interaction process as captured by our 1D model.

Limitations and future work

Limitations of the model with respect to formulations of viscoelasticity, wall friction and convective acceleration terms have been discussed above. The heart model is also a simplistic one, and there is evidence that the varying elastance curve may not be invariable with disease (Jegger, Mallik et al. 2007). The model neglects venous circulation as well as pulmonary circulation. The effects of CSF circulation surrounding intracranial arteries have not been taken into account. The limitations of the Windkessel models employed in the cerebral circulation are not known and need to be investigated in detail. Autoregulation phenomena, playing an important role in the cerebral and coronary circulation are neglected. The coronary tree model is also a simplistic one, requiring further modeling efforts to include the effects of myocardial contraction on vessels and peripheral coronary beds.

The validation has been restricted to a group of young volunteers. Future work will consider the effects of ageing and disease on arterial wall properties, peripheral impedances and cardiac function and validation on aged subjects or patients group will be performed.

This work permitted to qualitatively validate the predictions of a generic arterial tree model based on averaged in vivo measurements on volunteers. Future work will be focused on a quantitative validation of the model on a specific subject. The arterial tree will be construct based on geometry and elasticity data derived from measurements on the specific person and model predictions will be compared to noninvasive *in vivo* measurements on the same subject.

CONCLUSIONS

We have extended and improved a previous 1D model of the systemic circulation, by including a heart model, a detailed description of the cerebral arterial tree, viscoelasticity and a Witzig-Womersley theory-based formulation for the friction and convective acceleration terms. The model predicts pressure and flow waves which are in fairly good qualitative agreement with *in vivo* measurements, especially with respect to the shape and wave details. The results obtained validate the model predictions of pressure and flow in central arteries as well as in major arteries of the brain, reinforcing thus the general applicability of the model to the entire systemic and cerebral circulation.

ACKNOWLEDGMENTS

This work was supported by the European Commission contract no. IST-027703 @neurIST Project. MRI research was funded by the Center for Biomedical Imaging (CIBM) at the University Hospital of Geneva (HUG) and EPFL. The authors would like to thank François Lazeyras and Pascal Challande from the CIBM-HUG for the MRI measurements and Virginie Chenaux for the work performed during her EPFL Master thesis project.

PAPER II - VALIDATION OF A PATIENT-SPECIFIC 1-D MODEL OF THE SYSTEMIC ARTERIAL TREE

Philippe Reymond[1], Yvette Bohraus[1], Fabienne Perren[2], Francois Lazeyras[3] and Nikos Stergiopulos[1]

1 Laboratory of Hemodynamics and Cardiovascular Technology
Ecole Polytechnique Fédérale de Lausanne, Switzerland
2 HUG, University Hospital and Medical faculty of Geneva,
Dept of Clinical Neurosciences, Neurology, Geneva, Switzerland
3 HUG, University Hospital and Medical faculty of Geneva,
Dept of Radiology, Geneva, Switzerland

INTRODUCTION

At present, 1-D models are best suited to study flow and pressure waveforms along the whole or extensive parts of the systemic and pulmonary circulation. They can provide insight regarding wave propagation and reflection phenomena and allow for characterization of ventricular-arterial coupling. Because of their relatively low computational cost and complexity, 1-D models have been extensively used in the past to study different pathologies, such as hypertension by Westerhof et al. (Westerhof, Bosman et al. 1969; Westerhof, van den Wijngaard et al. 2008), arteriosclerosis by Raines et al. (Raines, Jaffrin et al. 1974), stenoses by many authors (Avolio 1980; Stettler, Niederer et al. 1981; Meister 1983; Kufahl and Clark 1985; Hillen, Hoogstraten et al. 1986; Zagzoule and Marc-Vergnes 1986; Papapanayotou, Cherruault et al. 1990; Fitchett 1991; Stergiopulos, Young et al. 1992; Cassot, Zagzoule et al. 2000), anatomical variations of cerebral arteries, arterial occlusion by Alastruey et al. (Alastruey, Parker et al. 2007) or to study surgery plans by Wan et al. (Wan, Steele et al. 2002). An extended review on 1-D models has been published in our previous article (Reymond, Merenda et al. 2009).

The primary question addressed in this article was the validity of the generic 1-D model predictions. The approach we followed was to compare the predictions of the generic 1-D model with the average pressure and flow waveforms measured noninvasively in a group of healthy young individuals. The underlying hypothesis was that although the generic model would not represent precisely a specific individual it should represent reasonably well the “average” of the group. Hence, the model validation was strictly qualitative. Reymond et al. 2009 suggested that future work should be focused on a quantitative validation of the model on a specific subject with the arterial tree constructed based on geometry and elasticity data derived from measurements on the specific person. The model predictions could then be compared to noninvasive in vivo measurements on the same subject. This is exactly the method followed and reported in the present follow-up study.

METHODS

Physiological data

To build a coherent patient-specific 1-D model of the arterial tree, we performed measurements of the arterial geometry using MR angiography on a 30-year old healthy volunteer (height 183 cm, weight 90 kg). Noninvasive pressure and flow measurements were performed on the same volunteer using applanation tonometry (pressure) and Doppler and MRI (flow). All measurements were obtained with the subject at rest in the supine position. with the heart rate nearly identical for the different measurements. Measurements were performed at the Geneva University Hospital (HUG), according to a protocol approved by the local ethics committee. The volunteer provided written, informed consent.

The arterial tree model is based on the 103-segment model reported by Reymond et al (Reymond, Merenda et al. 2009) with the primary model equations rewritten in the appendix. The present patient-specific arterial tree has been updated by removing the coronary and anterior choroidal arteries, vessels that were not available from the imaging performed in the specific volunteer (Fig. 1). The specific arterial tree has 94 arterial segments, specified by their proximal and distal cross-sectional area and length. The geometrical parameters are given in Table 1.

Table 1. Geometry, distensibility, viscoelastic properties and peripheral resistances and compliances of the arterial tree.

Arterial segment name	Arterial segment number (Right/Left)	Arterial segment length (mm)	Proximal lumen diameter (mm)	Distal lumen diameter (mm)	Distensi-bility (Dw) (10^{-3} $mmHg^{-1}$)	Visco-elasticity coeff. (a)	Terminal resistance ($R_1 + R_2$) (mmHg s/ml)	Terminal compliance (C_T) 10-5 (ml/mmHg)
Ascending Aorta 1	1	55	30.5	28.9	5.49	0.05		
Aortic Arch A	2	8	28.3	28	5.32	0.05		
Brachiocephalic	3	46	13.1	12.3	3.3	0.08		
Subclavian A	4/19	23/53	11.8/10	10.8/9.2	3.08/2.79	0.09/0.1		
Common Carotid	5/15	94/139	7.8/7.3	7.2/7.1	2.41/2.35	0.11		
Vertebral	6/20	149/148	3.5/3.3	1.7/2.4	1.27/1.35	0.14		
Brachial	7/21	299/333	8/7	3.9/3.8	2.09/1.98	0.12		
Radial	8/22	235	2.6/2.4	2.2/2.0	1.21/1.15	0.14	49.9	198.8/153.7
Ulnar A	9/23	67	2.6/3.0	2.4/2.9	1.25/1.37	0.14		
Interosseous	10/24	79	1.5/1.3	1.3/1.2	0.88/0.81	0.15	99.8	51.4/40.8
Ulnar B	11/25	171	2.3/2.8	2.0/2.5	1.13/1.29	0.14	99.8	153.7/287.9
Internal Carotid	12/16	178/177	6.5	4.4	1.99	0.12		
External Carotid 1	13/17	55/67	5.6/5.3	5.0/4.9	1.95/1.9	0.12/0.13		
Aortic Arch B	14	9	28	27.8	5.29	0.05		
Thoracic Aorta A	18	148	27	21.3	4.85	0.05		
Intercostals	26	14	7.5	7	2.36	0.11	10.4	1959
Thoracic Aorta B	27	84	20	19.8	4.32	0.05		
Abdominal Aorta A	28	18	20	19.8	4.32	0.05		
Celiac A	29	9	9.3	8.5	2.67	0.1		
Celiac B	30	9	8.5	7.6	2.51	0.11		
Hepatic	31	34	5.5	5.4	1.99	0.12	27.2	2022
Gastric	32	71	3.2	3	1.42	0.14	40.5	454
Splenic	33	241	6.2	5.3	2.05	0.12	17.4	2017
Superior Mesenteric	34	60	7.6	7.4	2.41	0.11	5.9	4600
Abdominal Aorta B	35	7	19.5	17.5	4.13	0.05		
Renal	38/36	27/46	6.3/5.7	5.5/5.0	2.08/1.96	0.12	7.1	2200/1713
Abdominal Aorta C	37	7	17.5	17.3	3.99	0.05		
Abdominal Aorta D	39	43	17.3	17.2	3.97	0.05		
Inferior Mesenteric	40	50	4.7	3.2	1.64	0.13	33.3	586
Abdominal Aorta E	41	43	17.8	17.6	4.03	0.05		
Common Iliac	42/43	86/85	11.5/12.5	11.4/12.2	3.1/3.25	0.09/0.08		
External Iliac	50/44	139/141	11.0/11.3	8.8/11	2.84/3.05	0.1/0.09		
Inner Iliac	51/45	30	6.0/8.1	5.5/6.3	2.05/2.35	0.12/0.11	49.9	2167/3253
Femoral	52/46	446/444	8.5/8.0	6.9/6.4	2.44/2.35	0.11		
Deep Femoral	53/47	55	7.0/6.5	6.7/6.0	2.28/2.16	0.11/0.12	33.3	3568/2711
Posterior Tibial	54/48	417/410	4.4/4.8	1.8/2.1	1.41/1.51	0.14	79.8	155/227
Anterior Tibial	55/49	422/417	3.1/3.2	1.9/2.1	1.24/1.29	0.14	79.8	157/199
Basilar Artery 2	56	20	3.4	3.1	1.46	0.32		
R Superior Cerebellar	57/58	15/10	1.7	1.4	0.93	0.33	200	12.8
Basilar Artery 1	59	5	2.7	2.5	1.27	0.32		
Post. Cerebral 1	60/61	2	1.6/2.2	1.55/2.15	0.94/1.14	0.33/0.32		
Post. Communicating	62/63	4	1.8/0.9	1.75/0.85	1.01/0.66	0.33		
Post. Cerebral 2	64/65	12	2.3/2.1	1.3/1.9	1.02/1.09	0.33/0.32	80.1	12.1/27.4
Int. Carotid Distal	66/67	4	3.9	3.8	1.61	0.31		
Ant. Cerebral 1	68/69	12/11	1.6/2.5	1.4/2.3	0.92/1.21	0.33/0.32		
Middle Cerebral 1	70/73	12/17	3.0/2.8	2.5	1.32/1.29	0.32		
Middle Cerebral 2 Sup. Branch	71/74	8	1.1/1.2	1.0	0.74/0.76	0.33	107	5.2/5.3

Middle Cerebral 2 Inf. Branch	72/75	8	2.3/2.2	1.0	0.97/0.95	0.33	107	6.8/6.6
Ant. Cerebral 2	76/78	24/23	1.7/1.9	1.2/1.4	0.90/0.97	0.33	80.1	9.0/13.3
Ant. Communicating	77	2	1.3	1.25	0.83	0.33		
ICA sinus	79/81	11/10	4.2	4	1.67	0.31		
Ophthalmic	80/82	11/10	1	0.5	0.6	0.33	200	1.06
External Carotid 2	83/85	61/60	4.5	3.9/4.0	1.7	0.13		
Sup. Thy. Asc. Ph. Lyng. Fac. Occipital	84/86	101/100	2.2/2.3	1.1	0.98/0.99	0.15	181	21.5/22.0
Superficial Temporal	87/89	61/60	3.6/3.5	3.4/3.3	1.52/1.5	0.14		
Maxillary	88/90	91	2.5/2.43	1.1	1.02	0.15	181	22.3/22.6
Superficial Temporal Frontal Br.	91/93	100/102	2.5	1.6	1.09/1.1	0.14	181	46.9/48.0
R Superficial Temporal Parietal Br.	92/94	101/103	2.5	1.6	1.09/1.1	0.14	181	46.9/48.0

Angiography

MRI Time of Flight (ToF) measurements were carried out on a 3T scanner (Siemens Trio-Tim 3T System). Images of the systemic circulation were obtained by addition of the contrast agent (23 ml OMNISCAN 0.5 mmol/ml + 25 ml NaCl) using adapted sequence parameters (flip angle 17°, TE = 1.02 ms, TR = 2.6 ms, FoV 431 mm x 834 mm, slice thickness 1.3 mm). Data on cerebral (flip angle 15°, TE = 3.69 ms TR = 22 ms, FoV 177 mm x 199 mm, slice thickness 0.6mm), neck (flip angle 60°, TE = 5.1ms, TR = 20ms, FoV 160 mm x 200 mm, slice thickness 1.5 mm) and lower limb circulation (flip angle 60°, TE = 5.1 ms TR = 20 ms FoV 240 mm x 300 mm, slice thickness 1.5 mm) were acquired without contrast agent use.

The arterial tree geometry was reconstructed in 3D (Fig. 2) from MRI magnitude data (ITK Snap software). Dicom images were processed using a gradient diffusion filter. The pre-segmented vasculature region was computed based on contrast threshold. This region was used as an initial region to obtain a more accurate segmentation using an edge detection method based on contrast intensity gradient.

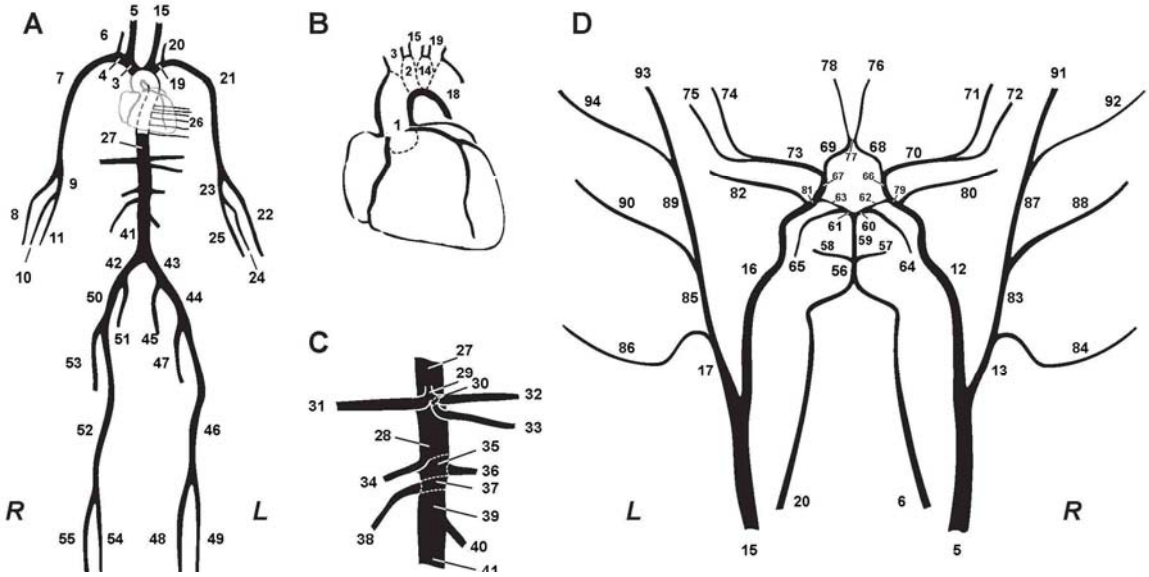

Figure 1. Schematic representation of the arterial tree adapted from Reymond et al (Reymond, Merenda et al. 2009).

(A) Main systemic arterial tree, (B) Detail of the aortic arch (coronary arteries are not taken into account).

(C) Detail of the principal abdominal aorta branches.

(D) Schematic of the detailed cerebral arterial tree, which is connected via the carotids (segments 5 and 15) and the vertebrals (segments 6 and 20) to the main arterial tree shown in (A) (anterior choroidal arteries are left out).

Geometric measurements for each arterial segment were acquired with ICEM CFD 11 software (ANSYS Inc., Canonsburg, PA). Local diameter values were estimated from the average of 4 measurements at each cross section, while length measurements were assessed along the centerline of the arterial segment (Table 1). Arterial tree dimensions were taken as measured and not adapted to minimize reflection coefficients for forward waves at bifurcations, as was the case in our previous work (Reymond, Merenda et al. 2009), where reflection coefficients were limited to 0.1. The effect of such optimization will be elaborated in the discussion.

In vivo measurements

Volume flow rate waveforms were obtained in several systemic arteries (common carotid arteries (CCA), ascending, descending, thoracic and abdominal aorta, iliac and femoral arteries) using gated phase-contrast MRI and in precerebral and cerebral arteries (common carotid, external carotid ECA, internal carotid ICA, vertebral arteries VA and middle cerebral artery MCA) using B-mode and color-coded duplex flow imaging. Pressure waveforms were measured at superficial arteries (radial, carotid and temporal arteries) using applanation tonometry. Mean blood flow rates measured by the phase contrast MRI and Doppler techniques presented hereafter are summarized in table 2. The end diastolic flow waveform foot was set as reference for temporal alignment of cardiac cycles and 5-15 cycles were averaged to obtain a smoothed waveform.

Table 2. Mean blood flow rate for different central and cerebral arteries from our in vivo measurements (PC-MRI and Doppler ultrasound) as well as the values obtained from the 1-D model.

Artery	Phase contrast MRI (ml/s)	Ultrasound (ml/s)	Model (ml/s)
Ascending aorta	103	-	103.1
Descending aorta	72	-	82.8
Thoracic aorta	70	-	73.0
Abdominal aorta	17	-	15.4
Right external iliac artery	7.3	-	5.5
Left external iliac artery	5.3	-	5.6
RCCA	9.7	7.0	6.0
LCCA	8.1	5.6	6.0
RICA	-	4.7	4.1
LICA	-	3.9	4.1
RECA	-	2.8	1.9
LECA	-	2.5	1.9
RVA	-	1.3	0.4
LVA	-	1.3	0.9
RMCA	-	1.7	1.8
LMCA	-	1.4	1.8

Blood flow measurement using Phase-Contrast MRI

Sequences that provided velocity measurements over an entire cardiac cycle at selected cross section locations were performed. 2-D through plane Phase Contrast PC-MRI sequences (slice thickness 6mm TE/TR 3.3/51.7 ms, flip angle 20°, FoV 220 x 320 mm, iPat Siemens Parallel acquisition Technique, VENC 150 cm/s for the CCA and the thoracic aorta, 110 cm/s for the abdominal aorta) were acquired in resting conditions. The measurement planes were determined using flash angiography images to ensure that the plane was perpendicular to the vessel axis. For aortic measurements, breathhold sequences were performed over a period of 19 seconds to minimize

movement artifacts. Twenty index finger pulse pressure gated phase and magnitude images were acquired at each measurement location.
Arterial cross sections were automatically segmented (Argus Flow VA60C 2004, Siemens) to follow lumen area changes over the heart cycle. Volume flow rate was the integral of the velocities across the lumen.

Blood flow measurement using Color-coded duplex ultrasound

Transcranial color-coded duplex flow imaging (CDFI) with a 5-8 MHz linear phase array and a 2-4 MHz sectorial transducer were used to assess blood flow velocities in the cerebral vasculature (Toshiba medical device, Aplio 80). CDFI was performed at the cervical (CCA, ECA, ICA: extracranial window, insonation angle 60°) and cerebral (VA: suboccipital window, insonation angle 60°; MCA: temporal window, insonation angle 0°) vessels. Blood flow was computed from the peak velocity waveforms using the Witzig-Womersley theory, assuming a constant lumen diameter values. Diameters of extracranial arteries were obtained using Doppler M-mode whereas geometrical dimensions of ICA were determined by MRI angiography.

Pressure measurement using applanation tonometry

Pressure waveforms over 10 heart cycles were acquired at the distal radial artery, distal common carotid artery (CCA) and temporal arteries (Figures 2F and 2H) with applanation tonometry (Millar Instruments, SPT 301, Houston, TX) . Brachial sphygmomanometer measurements were taken to calibrate applanation tonometry measurements, assuming that mean and diastolic pressures do not vary much between the brachial, carotid, radial and temporal locations. Mean sphygmomanometer pressure was calculated as $P_{mean} \cong P_{diastole} + 1/3\ PP$ (Segers, Rietzschel et al. 2005), where PP is the pulse pressure (P_{sys}-P_{dia}).

Arterial stiffness assessment

To render the elastic properties of the patient-specific 1-D model, we measured the timing of the foot of the pressure wave at the CCA, radial and temporal artery. Pressures were measured using applanation tonometry and were combined with simultaneous measurements of ECG (PSYLAB Contact Precision Instruments Inc., Boston MA). The time delay between the foot of the pressure wave and the ECG R-wave was 178, 96, and 104 ms for the radial, the distal part of common carotid, and the temporal arteries, respectively. Distensibilities of all vessels of the 1-D model were then adjusted by a common factor to obtain the minimum difference between the simulated and measured travel times. Local distensibility was taken to be a function of the transmural pressure and lumen diameter (Appendix equations A.3-7).

Mathematical description of the model

The 1-D form of the fluid mechanics equations are mentioned in the appendix. The intimal shear stress and non linear convective acceleration terms are modeled using the Witzig-Womersley theory. In contrast to our previous work, at the aortic root we impose flow measured in the subject by MRI.

Viscoelastic properties of the arterial wall

The non-linear viscoelastic constitutive law for the arterial wall, proposed by Holenstein et al. (Holenstein, Niederer et al. 1980) and adapted by Reymond et al. (Reymond, Merenda et al. 2009), was used in the present study (Equations A.8-10). Having limited information and testing methods to adjust the viscoelastic coefficients to the specific subject, we used the same model as for the generic tree. However, the viscous coefficients depend on local vessel size (Equation A.10) and are thus different than the generic tree.

Distal vasculature models at termination sites

All distal vessels are terminated with three-element Windkessel models to account for the proximal and distal resistance and compliance of the distal vascular beds. Distal resistances were adapted to obtain a flow distribution that was close to the flow deduced from the reported mean flow values in table 2.

Patient-Specific vs. generic arterial tree model comparison

In order to verify the advantages of using a patient-specific arterial tree, we compare the predictions of the patient-specific model to the generic one developed earlier by Reymond et al. (Reymond, Merenda et al. 2009). We apply the same inflow waveform at the aortic root with the distal Windkessel model values unchanged from the generic model. Global distensibility and systemic vascular resistance of the generic arterial tree is adapted to yield the same central mean and pulse pressure and mean pressure as the patient-specific model. The predictions of the patient-specific and generic arterial tree model are compared to flow measured at the thoracic aorta and ICA and pressure at the superficial temporal artery. A quantitative assessment of the relative error is performed by computing the root mean square of the error (RMSE) of the predicted waveforms compared to the in-vivo measurements. RMSE is considered to be a good indicator of the error, but, is not the best index to qualify the reproduction of specific wave features.

RESULTS

Patient-specific arterial tree model predictions vs. in vivo measurements

Figure 2 shows a comparison of predicted pressure and flow waveforms to measured waves at different arterial locations. The predicted flow waves in the main aortic segments (thoracic and abdominal aorta Fig. 2E, 2G) and common carotid artery (CCA, Fig. 2D) are compared to PC-MRI measurements. The predicted flow waveform at the internal carotid artery (ICA, Fig. 2A), at the middle cerebral artery (MCA, Fig. 2B) and external carotid artery (ECA, Fig. 2C) is compared to ultrasound measurements. Pressure waveforms measured with applanation tonometry are compared to model predictions in the CCA (Fig. 2F) and the superficial temporal artery (Fig. 2H). We observe that the overall agreement in both amplitude and wave shape features, at all arterial locations and for both pressure and flow is good. The relative RMSE for pressure is below 10%, with 4 and 6% at the temporal and CCA, respectively. Relative RMSE for flow is also below 10% except, at the left CCA and abdominal aorta, where RMSE is 11 and 21%, respectively. The error at the abdominal aorta was due to a marked difference in local flow pulsatility.

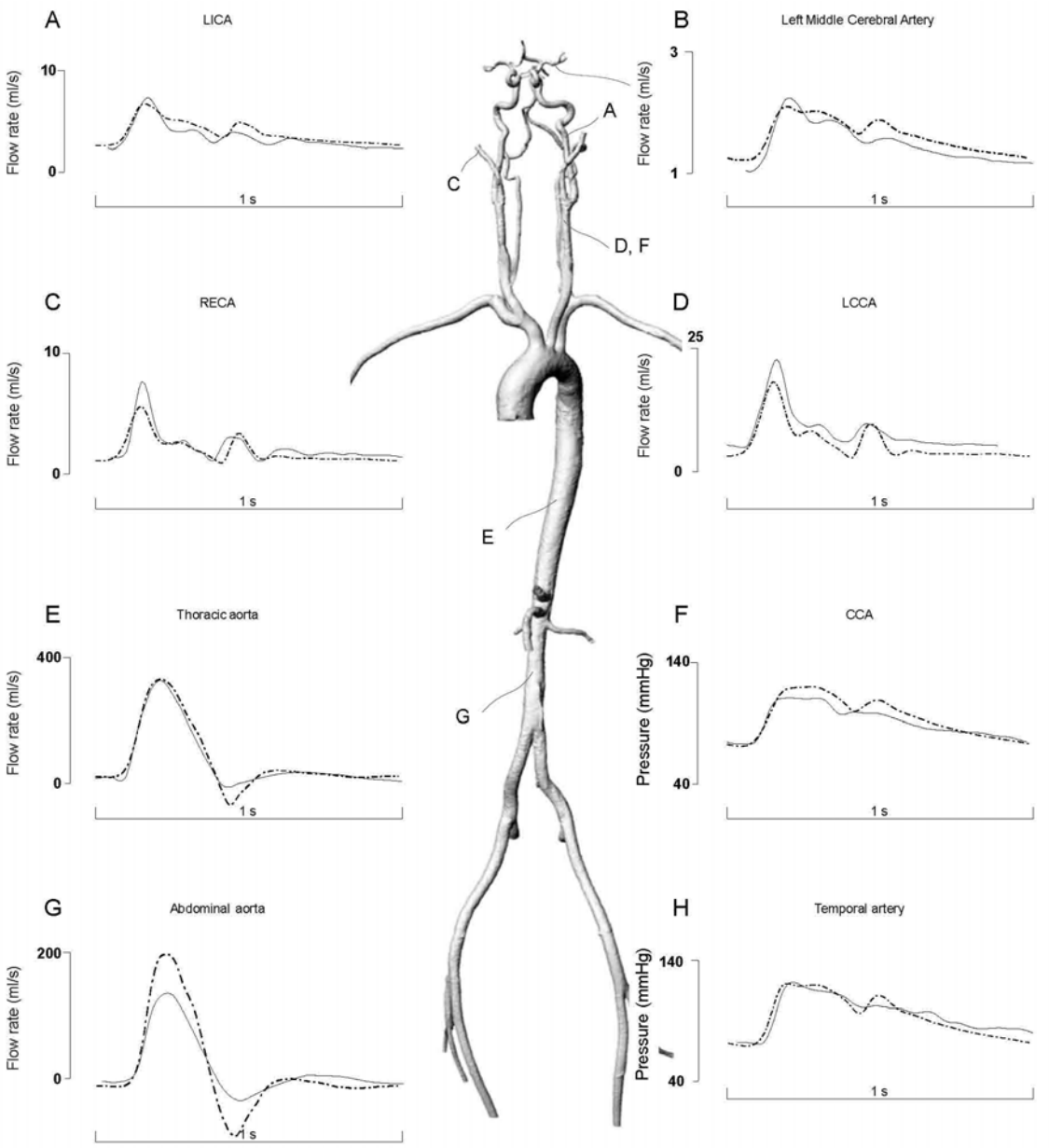

Figure 2. Model predictions (dash dot) compared to in vivo measurements of flow and pressure waves (continuous line) for different systemic and cerebral arteries. Flow is measured with B-mode color-coded duplex flow imaging technique in the left internal carotid LICA (A), left middle cerebral artery LMCA (B) and right external carotid RECA (C), with PC-MRI in the left common carotid artery LCCA (D) in the thoracic aorta (E) and in the abdominal aorta (G). Pressure was measured with applanation tonometry in the common carotid artery CCA (F) and superficial temporal artery (H). The central picture is the representation of the 3D geometry of the patient-specific arterial tree from MRI angiography. In parenthesis are RMSE computed between simulations and measurements and expressed in percentage relative to the in-vivo systolic values.

Patient-specific vs. generic arterial tree model comparison

The predictions of the patient-specific model are compared to those of the generic one in Figure 3. We observed that, overall, the patient-specific model reproduces the features of the flow and pressure waves better in terms of both amplitude and wave shape. The RMSE values
of the patient-specific model predictions at the thoracic aorta, proximal ICA and superficial temporal artery are 5, 9 and 4%, respectively. These RMSE values are lower than for those obtained from the same locations in the generic model (13, 12 and 5%).

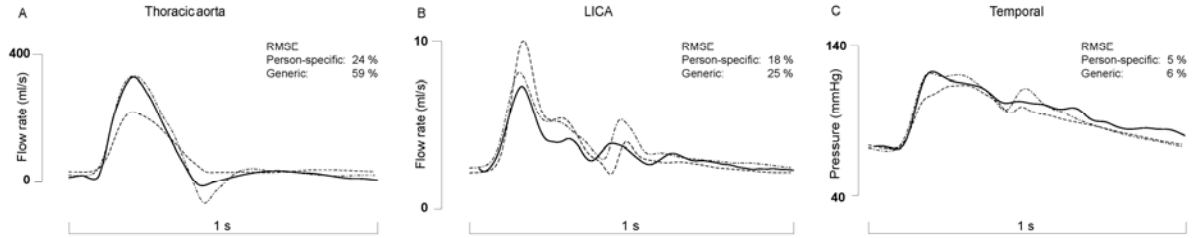

Figure 3. Generic (dash) and specific (dash dot) arterial tree model predictions are compared to in vivo measurements (continuous line) of flow and pressure waves for different systemic and cerebral arteries. Flow is measured with PC-MRI in the thoracic aorta (A) and with color-coded duplex ultrasound in the internal carotid LICA (B). Pressure was measured with applanation tonometry in the superficial temporal artery (C).

DISCUSSION

Patient-specific arterial tree

Flow in cerebral and precerebral arteries

Flow rate waveforms in cerebral and carotid arteries are well reproduced, the early and late systolic peaks are present and their relative amplitudes are predicted accurately. In the case of the LMCA, the pulsatility of the predicted wave is less pronounced (Fig. 2B). At the RECA level, all wave features are well reproduced with the wave peaks present at the correct time. However the early systolic peak amplitude is underestimated by the model compared to the in-vivo measurements (Fig. 2C). The flow waveform features for the LCCA are similar, while the average flow is different. Mean flows from the in-vivo measurements were used to derive the distal resistances of the Windkessel models. However, distal anastomoses affects the flow distribution among the different branches feeding the Circle of Willis.

Flow in the central aorta

Thoracic aorta flow waveform is discussed hereafter when specific and generic arterial tree are compared. Concerning the abdominal aorta, systolic peak and dicrotic notch have the same relative timing in the model and in the measurements, but their amplitudes differ. Mean flow values for the 1-D model prediction and PC-MRI measurements also differ (15.4 vs. 17 (ml/s), respectively), but this difference may not entirely explain the large discrepancy in pulsatility. We recognize that wave reflection phenomena that require a precise geometry of the distal vessels was not properly reproduced by the patient-specific model. Error in PC-MRI measurements may also contribute to the differences in pulsatility, e.g. error in the location and segmentation of the aortic cross-section.

Pressure in superficial arteries

Concerning the CCA, the patient-specific model and applanation tonometry present a kind of plateau during systole, that is marked by the presence of early and late systolic peaks. There is a time shift between the dicrotic notch in the patient-specific model and measured waveforms that is discussed in more detail hereafter. In the distal superficial temporal artery, the waves present a distinctive separation of the two peaks with the early systolic peak elevated. The comparison between the model and experimental waves is very favorable.

Model of the left ventricle

In our previous work, we implemented a simple model for the left ventricle based on the varying elastance model. In the present study, we preferred to use the flow waveform measured at the aortic root for the proximal boundary condition. This decision was motivated by the fact that the patient-specific and the generic model are different and in consequence they would represent different afterloads to the heart, yielding different flows in the proximal aorta.

Patient-specific vs. generic arterial tree comparison

Flow in the aorta

Figure 3 shows that the patient-specific model closely reproduces the systolic part of the thoracic aorta flow waveform. In contrast, the generic model underestimates it greatly, despite the fact that the wave shape predicted by the generic model is acceptable and mean flow in both models were nearly identical (~73 ml/s).

We observe that the dicrotic notch predicted by the specific model at the thoracic and abdominal aorta is more pronounced than that measured by PC-MRI and obtained by the generic arterial tree (Fig. 3A). This may be attributed to augmented wave reflection phenomena in the specific arterial tree. In Figure 4 we plotted the lumen area and local reflection coefficients of the specific and generic model along the main aortic trunk and the iliac arteries.

We observe that the specific arterial tree presents higher reflection coefficient at the iliac bifurcation (0.1) and, more importantly, values up to 0.3 (not visible in this figure) in the distal bifurcations, the femoral and tibia regions. We have chosen to keep the geometry as measured and not interfere in the construction of the specific arterial tree by means of optimizing wave reflections. In the generic arterial tree, reflection coefficients were limited to the somewhat arbitrary value of 0.1 by iteratively adjusting the area of downstream vessels. In addition, construction of the arterial tree in the lower limb regions from MRI scans was difficult in comparison to the aortic and cerebral regions. The MRI angiography images obtained for the lower limbs, such as the tibia, presented artifacts and were consequently difficult to segment and obtain a precise geometry.

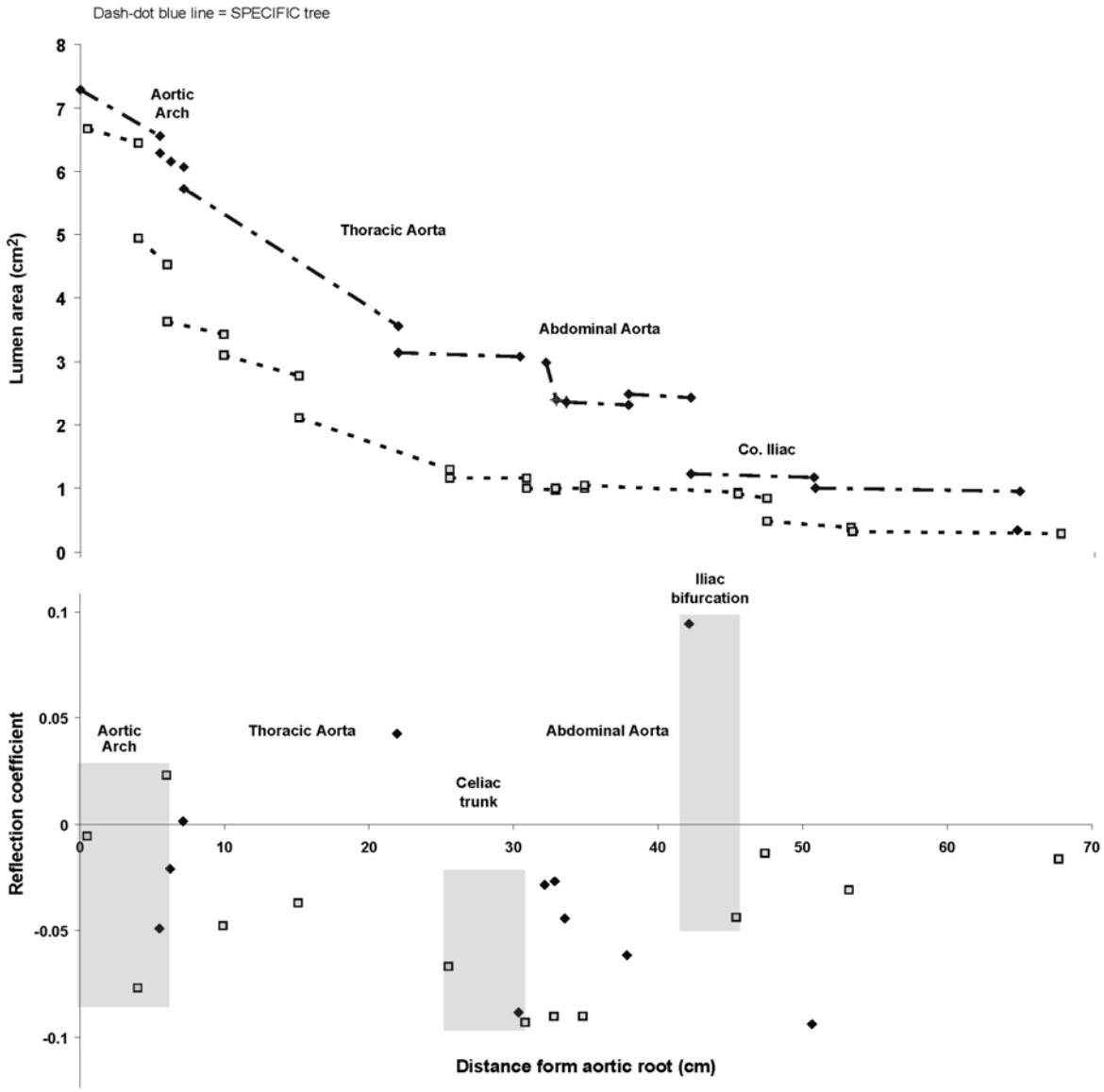

Figure 4.Lumen area (upper panel) and forward wave reflection coefficients (lower panel) along the aortic root and lower limb arteries. Generic (dash and square marker) and specific (dash dot and diamond marker) arterial tree models are represented.

To check whether optimization of reflections in the lower aorta and limbs is of importance, the patient-specific arterial tree was adapted to limit the reflection coefficients at specific locations to a value below 0.1. To achieve this, the area or compliance of the daughter branches can be modified. In order to avoid affecting the geometry, we adjusted the distensibility either increasing or decreasing its value in the downstream vessels. The dicrotic notch of the predicted flow waveforms was reduced and approached that measured in-vivo.

Flow in the internal carotid artery

The two first systolic peaks are reproduced well by the specific and generic arterial tree model (Figure 3B). However, the amplitude and pulsatility is better predicted by the patient-specific model. There is still a shift in the phase of the dicrotic notch and the third peak, for both models compared to the measurements. This may be a result of error in the estimation of distal cerebral vessel distensibility using the generic relationship in our models.

Pressure in the temporal superficial artery

Even though the quantitative comparison of specific and generic arterial tree is not as clearly in favor of the specific tree as it is for the flow comparison in the thoracic and internal carotid, the specific model was still able to better reproduce certain key wave features, such as the existence of a pronounced early systolic peak, which was totally missed by the generic model (Fig. 3C).

Perspectives on the use of a patient-specific 1-D model of the arterial circulation

Our previous work indicated that a generic 1-D model can be used to represent systemic arterial flow and pressure in an average young healthy adult and thus can be used to model the average of a population of a given group. In the present work, we have demonstrated that a carefully constructed patient-specific 1-D model of the arterial circulation gives substantially better results that a generic one. Earlier studies have also shown that a patient-specific model of the systemic circulation can give good predictions of arterial waves Olufsen et al. (Olufsen, Peskin et al. 2000), although the study by Olufsen et al. restricted the comparison of flow waves to the main arteries of the arterial tree and did not include comparison of pressure waves or comparison in arteries of the cerebral circulation. A well-tuned patient-specific model can become a very useful research tool. One can use such a validated model on a specific individual to study a number of important hemodynamic phenomena and validate model predictions with appropriate non-invasive measurements. However, such a patient-specific model requires a large amount of specific data related to geometry, elastic properties and peripheral impedances of the arterial tree, which would render the applicability of the model, for clinical and even for research purposes, very cumbersome. It is therefore logical to seek other ways to “personalize” to some extend the generic arterial tree based on fewer and clinically feasible measurements. One such approach, would be to use global descriptors related to the geometry and properties of the arterial tree which are easily measured, such as body size (height, weight), age, gender and pulse wave velocity (PWV) (i.e., carotid-to-femoral wave speed). One can then scale the geometry of the generic arterial tree based on body size and do similar adjustment on the elastic properties based on PWV. Gender and age can also be taken into account in a statistical manner, as was done previously for the generalized transfer function. This approach, which can be refined by adding other noninvasively measured appropriate indicators, has merit to be tested carefully in the future. It could provide a better means for modeling the arterial tree accurately enough without the complexity of a true patient-specific model.

Limitations

Venous circulation, as well as pulmonary circulation, is not included in the patient-specific and generic model. Cerebrospinal fluid pulsation effects on the intracranial arteries are not taken into account, while a mean transmural pressure from the CSF acting on the intracranial vessels (i.e. intracranial pressure) is taken into account.

Even though geometry, flow and pressure measurements were all performed on the same individual, there are still data (terminal compliance and resistances of the distal Windkessel models) that were not completely patient-specific. The peripheral resistances have been set as close as possible to those determined with the patient-specific flow measurements (table 2). Distal compliances were assumed to be proportional to the area compliance of the last arterial segment, as was done in (Reymond, Merenda et al. 2009), since direct measurements are difficult to implement and their effects are shown to be of secondary importance.

In summary, we have constructed, to the best of our knowledge, the first, rather complete, patient-specific 1-D-model of a human arterial tree. The model accurately predicts pressure and flow waves in the central and peripheral arteries. The patient-specific model compared favorably against a

generic 1-D model, indicating the importance of knowing well the exact geometry and elastic and resistive properties of the arterial tree.

CONCLUSIONS

A patient-specific 1-D model of the main systemic circulation, based on specific geometric arterial tree has been developed. It predicts pressure and flow waveforms shape and wave features at primary systemic circulation locations with a high qualitative agreement compared to in vivo measurements. Quantitative aspects of pressure and flow waveforms are also well reproduced, thereby validating the suitability of the 1-D model to predict pressure and flow waves in the entire systemic arterial tree.

ACKNOWLEDGMENTS

This work was supported by the by the European Commission contract no. IST-027703 @neurIST Project and by the Center for Biomedical Imaging (CIBM) of the Geneva-Lausanne Universities, the EPFL and the University Hospitals of Geneva and Lausanne. Specific functions for segmentation were developed and implemented in ITK Snap software by Dr. Joël Cugnoni, EPFL.

PAPER III - PATIENT- SPECIFIC MEAN PRESSURE DROP IN THE SYSTEMIC ARTERIAL TREE A COMPARISON BETWEEN 1-D AND 3-D MODELS

Philippe Reymond[1], Fabienne Perren[2], François Lazeyras[3] and Nikos Stergiopulos[1]

[1] Laboratory of Hemodynamics and Cardiovascular Technology
Ecole Polytechnique Fédérale de Lausanne, Switzerland
[2] HUG, University Hospital and Medical faculty of Geneva,
Dept of Clinical Neurosciences, Neurology, Geneva, Switzerland
[3] HUG, University Hospital and Medical faculty of Geneva,
Dept of Radiology, Geneva, Switzerland

INTRODUCTION

One-dimensional (1-D) models are, to date, the most appropriate models to study pressure and flow wave propagation in the arterial tree or parts thereof. 1-D models can be coupled with physiological models for the left ventricle (such varying elastance model (Fitchett 1991; Formaggia, Lamponi et al. 2006; Reymond, Merenda et al. 2009) and lumped or distributed models for the peripheral beds (Olufsen 1999; Alastruey, Parker et al. 2007; Azer and Peskin 2007). These models have been used extensively in the past to study physiological and pathological situations and have been validated qualitatively and quantitatively in-vitro and in-vivo (Stettler, Niederer et al. 1981; Meister 1983; Olufsen, Peskin et al. 2000; Matthys, Alastruey et al. 2007; Reymond, Merenda et al. 2009). For extensive review on the 1-D models, their formulation their use and validation can be found in (van de Vosse and Stergiopulos 2011).

Because 1-D models are based on integrated forms of the axial momentum equation, they lack information on the 3-D velocity profile and, in consequence, frictional losses can be only approximated by assuming a certain velocity profile function (Kufahl and Clark 1985; Olufsen, Peskin et al. 2000; Azer and Peskin 2007; Bessems, Rutten et al. 2007). The assumed velocity profile is often referred to a developed flow in a straight, non-tapered segment. This approach brings about two sources of error in the estimation of viscous losses: first, errors due to the assumptions on the velocity profile and, second, errors due to complex 3-D geometry of the arterial tree, with tapering, non-planarity and bifurcations all affecting the velocity profile and thereby shear stress and frictional losses (Grinberg, Cheever et al. 2011). To the above, one should add the non-Newtonian nature of blood, which is often neglected in the 1-D formulations.

The purpose of the current work is to compare pressure evolution from central arteries to peripheral arteries in a 1-D model of a patient-specific model of the arterial tree to that of 3-D CFD model of the exact same arterial tree. Because the 3-D CFD model does not include fluid structure interactions and thus cannot predict waveform propagation phenomena, the comparison was performed for the mean pressure distribution along the main arterial path lines, the mean pressure drop being the most appropriate indicator of the effective frictional losses.

METHODS

Arterial tree geometry

To obtain the detailed 3-D geometry the arterial tree, we performed measurements using MR angiography on a 30-year old healthy volunteer (height 183 cm, weight 90 kg) using a 3T MRI scanner (Siemens Trio-Tim 3T System). The arterial tree geometry was reconstructed in 3-D from the raw medical images. After pre-processing of the dicom using gradient diffusion, a threshold growing region was set as a starting surface for segmentation, using edge detection method based on intensity gradient. The resulting arterial tree geometry is shown in Fig. 1.

The 1-D model arterial tree, composed of 94 arterial segments, is based on the same MRI scan. Local diameter values were deduced from averaged measurements on each cross-section while length measurements were acquired along the centerline of the arterial segments. More details on the 1-D model are mentioned in (Reymond, Bohraus et al. 2011).

1-D model

The 1-D form of the continuity and axial-momentum equation is applied over each arterial segment. A non-linear viscoelastic constitutive law for the arterial wall was considered. Global arterial wall distensibility was based on literature data and adapted to the specific subject by matching pulse wave velocities estimated using the traveling time of pressure waves, as measured with ECG-referenced tonometry. The intimal shear stress and nonlinear convective acceleration terms are modeled using the Witzig-Womersley theory. In particular, wall shear stress, τ_w, at each arterial location was estimated using Womersley's theory as:

$$\tau_w(t) = -\frac{4\mu}{\pi R^3} Q_1 + \sum_n Re\left\{ \frac{\mu}{\pi R^3} Q_n \alpha i^{3/2} \frac{J_1(\alpha i^{3/2})}{J_0(\alpha i^{3/2})} \frac{1}{1 - \frac{2 J_1(\alpha i^{3/2})}{\alpha i^{3/2} J_0(\alpha i^{3/2})}} e^{iwt} \right\} \quad (1)$$

$$u(r,t) = \frac{2}{\pi R^2}\left(1 - \frac{r^2}{R^2}\right) Q_1 + \sum_n Re\left\{ \frac{Q_n}{\pi R^2} \frac{1 - \frac{J_0\left(\alpha i^{3/2}\, r/R\right)}{J_0\left(\alpha i^{3/2}\right)}}{1 - \frac{2 J_1\left(\alpha i^{3/2}\right)}{\alpha i^{3/2} J_0\left(\alpha i^{3/2}\right)}} e^{i\omega t} \right\} \quad (2)$$

where $Q_n(z,t)$ is the n^{th} harmonic of the flow pulse and J_0 and J_1 are the complex Bessel functions of first kind and of zero and first order, respectively. In equations (1, 2) the artery radius R is assumed constant and equal to the local radius at mean arterial pressure. α is the Womersley number for each harmonic.

Because the Womersley theory is obtained in the frequency domain, this requires periodic flows and the knowledge of the local flow waveform over the entire heart cycle. As in Reymond et al. (Reymond, Merenda et al. 2009), we use the flow waveform from the previous heart cycle to calculate the wall shear stress, $\tau_w(r,t)$, the velocity profile, u(r,t) and continue the heart cycles until convergence.

At its proximal end (root of the ascending aorta), we imposed to the model the flow rate waveform measured by Phase Contrast MRI (PC-MRI) on the same person. All distal vessels and vascular beds are terminated with three-element Windkessel models to account for the resistance and compliance of the distal small arteries, arterioles and capillaries. A detailed description of the 1-D model is presented in (Reymond, Bohraus et al. 2011).

3-D model

CFD approach

The segmented surface of the arterial tree lumen was imported in ICEM CFD (ANSYS Inc., Canonsburg, PA) and a tetrahedral mesh of the region was built. Different mesh density regions were created in the vicinity of the celiac trunk and in cerebral arteries to locally refine the mesh. Indeed these regions, which contain many bifurcations and branches, present complex flow patterns affecting the pressure drop. Maximum size of elements was specified in the different sub-domains of the arterials tree.

Mesh dependency test

We performed a mesh dependency test for both 1-D and 3-D models. We increased the number of mesh elements and computed the root mean square of the difference (RMSD) of pressure drop along the different centerlines, between consecutives heart cycles. The relative RMSD of two consecutives cycles are summarized in table 1. 3-D model meshes contained 2.2, 5.3, 10 and 20 millions of tetrahedral elements. 20M was the maximum mesh size, limited by the computer resources. This mesh seems appropriate to accurately characterize pressure drop, except for the centerline going to the cerebral vasculature (RMSD increases). Mesh refinement could have still been considered in this region, although the difference was considered acceptable (<0.5%). Concerning the 1-D model, we augmented the number of nodes along the brachial segment from 5, 10, 20 and 50. The amelioration between 20 and 50 nodes was not significant (less than 0.1 %). We choose to have a spatial increment of 1 cm for each segment of the arterial tree. This spatial increment was then applied to each segment of the arterial tree.

Table 1. Mesh dependency test. Quantification of pressure drop for the 3-D and 1-D models along different arteries. Difference of 2 consecutive mesh refinements is represented using the root mean square of the difference (RMSD) (%), relative to the mean pressure.

3-D (number of mesh elements)	2.2 to 5.3M	5.3 to 10M	10 to 20M
LFEM	8.67	0.14	0.10
RBRA	0.28	0.12	0.07
LMCA	0.45	0.22	0.46
1-D (number of nodes)	5 to 10	10 to 20	20 to 50
RBRA	0.94	0.18	0.07

Boundary conditions

For the inlet boundary conditions of the 3-D CFD, we imposed the mean pressure we obtained from the 1-D model at the aortic root, i.e. 93.8 mmHg. For the 25 outlets of the 3-D CFD, the mean flow rates computed by the 1-D model are imposed (table 2).

Table 2. Mean flow computed by the 1-D model utilized as boundary conditions for the 3-D model.

Arteries	mean flow, ml/s	Arteries	mean flow, ml/s	Arteries	mean flow, ml/s
Asc. Aorta	103.3	L int Iliac	2.38	LPCA	1.11
R Brachial	3.78	L Femoral	2.75	RMCA frontal	1.05
RECA	1.81	L Deep Femoral	3.57	RMCA parietal	1.2
LECA	1.87	R int Iliac	2.39	LMCA frontal	1.17
L Brachial	3.62	R Femoral	2.65	LMCA parietal	1.18
Celiac trunk	13.9	R Deep Femoral	3.59	ACA1	1.05
Sup Mesenteric	20	RSCb	0.44	ACA2	1.05
L Renal	14.8	LSCb	0.44	ACA3	1.05
R Renal	13.5	RPCA	1.12		

Blood rheology

1-D model blood rheology is Newtonian, density is 1050 (kg /m^3) and dynamic viscosity is 0.004 (Pa s). However for the 3-D CFD computation we considered both a Newtonian and Non-Newtonian description of blood viscosity. The Non-Newtonian model we implemented comes from the generalized Casson equation (Perktold and Rappitsch 1995). The dynamic viscosity μ is a function of the fluid shear strain rate γ (s^{-1}) and expressed as:

$$\mu = 0.1 \frac{(k_0(c) + k_1(c)\sqrt{\gamma})^2}{\gamma} \quad (Pa \cdot s) \tag{3}$$

where the coefficients given for a 45 % hematocrit (c) are k_0 = 0.194 $Pa^{1/2}$, k_1 = 0.055 $(Pa\ s)^{1/2}$. This relationship is implemented in CFX5-Preprocessor (ANSYS Inc.) using CEL expressions. An upper limit of shear rate was set, to limit the values of viscosity. It avoids singularities that lead to high non-physical values. Viscosity ranged from 0.004 to 0.06 (Pa s). The lower μ value (high γ) is the same as for the 1-D model.

Pressure drop calculations and comparisons

3-D steady flow simulations were run utilizing the CFX5 solver (ANSYS Inc.) with Newtonian and Non-Newtonian blood rheology. From the 3-D simulations pressure was computed along the 3 centerlines (shown in Figure 1 and compared to the averaged unsteady 1-D model predictions along the same centerlines. Centerlines originate all in the ascending aorta and end the left femoral artery (1), the right brachial artery (2) and the left middle cerebral artery (3), to cover all main pathways and different geometries and vessels sizes.

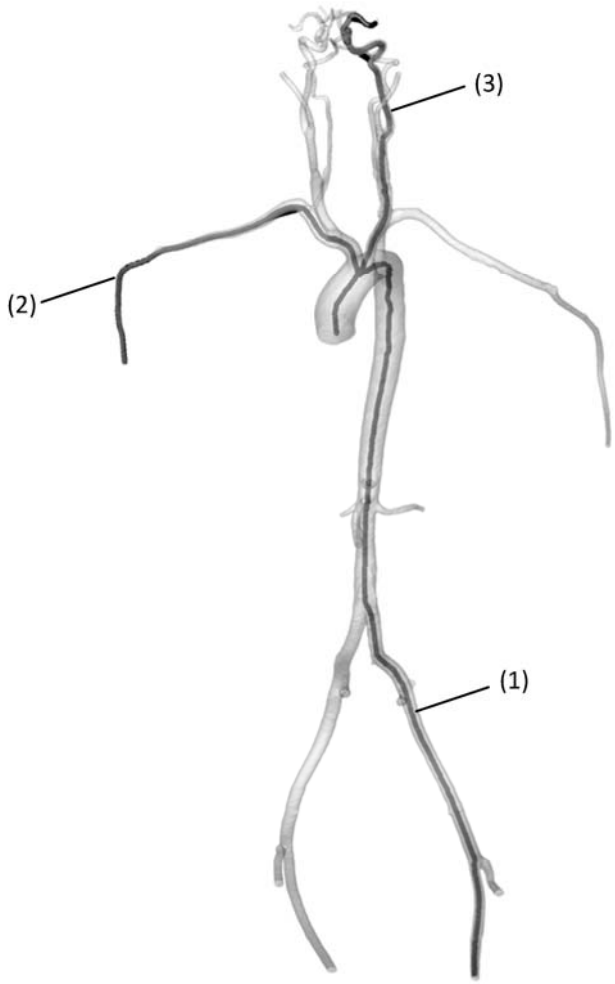

Figure 1. Representation of the patient-specific arterial tree obtained from MRI. The 3 centerlines, originating from the ascending aorta and along which pressure variation in calculated and compared between 1-D and 3-D model prediction, are represented.).

RESULTS

Figure 2 shows the pressure evolution along the 3 centerlines, as predicted by 3-D CFD simulations for Newtonian and Non-Newtonian blood rheology and the comparison to 1-D model mean pressure predictions (continuous line) along the same paths. CFD simulations predict a pressure drop from aortic root up to iliac bifurcation of 0.4 mmHg (0.7 mmHg for Non-Newtonian). The pressure drop is much more substantial along pathline 3, from aortic root up to the left middle cerebral artery and reaches 12 mmHg. Maximum difference of pressure between Newtonian and Non-Newtonian blood rheology is 1 mmHg in medium size arteries.

Pressure drop predicted by the 1-D and 3-D models in the aorta and the relatively large arteries included in pathline (1) was very similar. There is a localized non-monotonic decrease and subsequent increase in pressure along centerline (1) at the celiac trunk level, which is present in the 3-D simulations but absent in 1-D predictions (Figure 2A). The same remark applies at few locations of cerebral arteries where peaks are present. Along pathline (2), pressures are similar up to 260 mm from the aortic root. The differences increase in the distal part of the brachial artery, reaching up to 0.8 mmHg (Figure 2B). Significant differences exist along pathline (3), especially distal to the common carotid artery level. Differences reach 5 mmHg in the distal MCA-2 segment (Figure 2C).

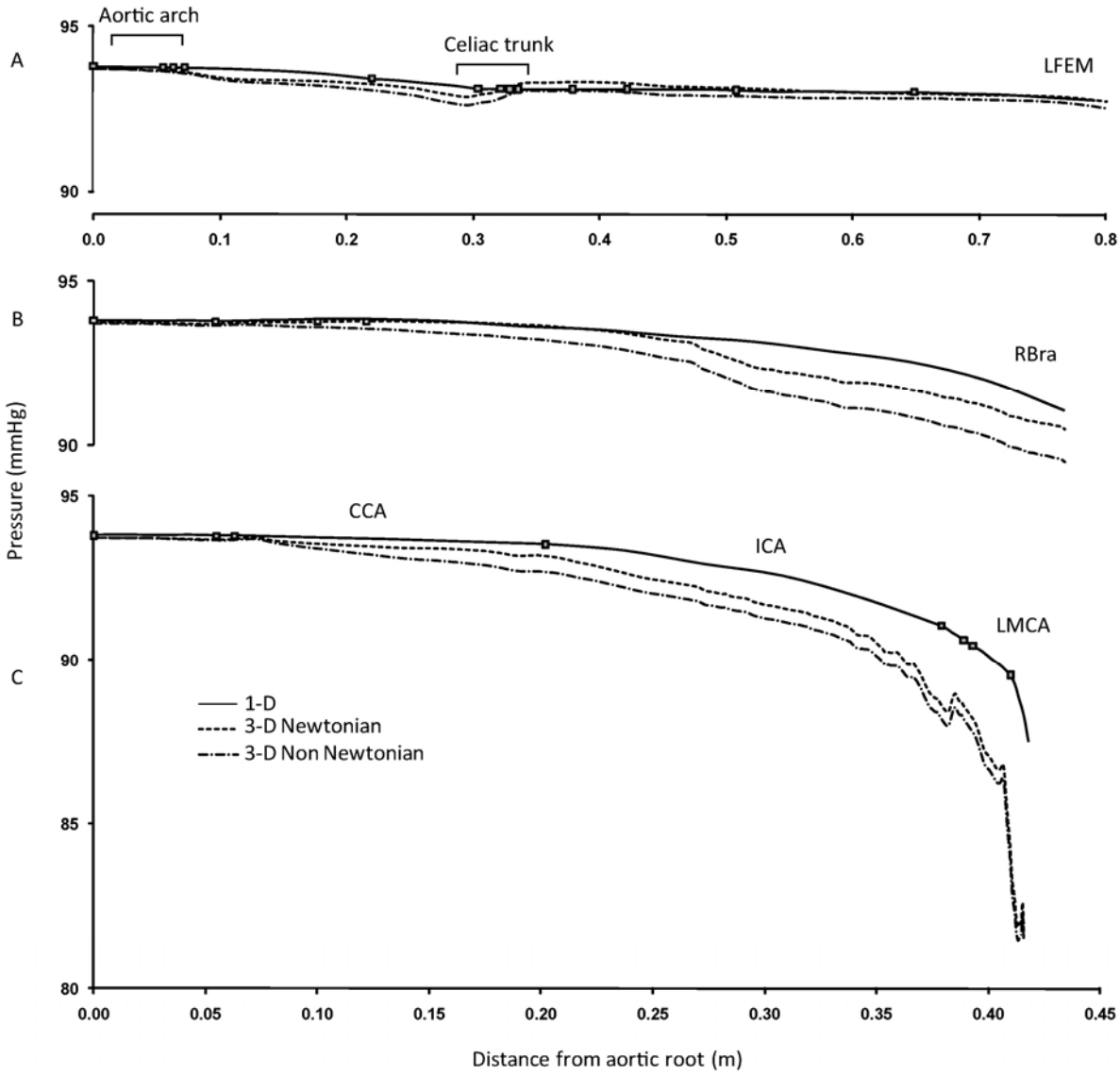

Figure 2. Pressure evolution from 3-D CFD (Newtonian and Non-Newtonian blood rheology) along the 3 centerlines, are compared to 1-D model predictions (continuous line). Centerlines originate from the ascending aorta, toward the left femoral artery (A), the right brachial artery (B) and the left middle cerebral artery (C). Squares delimit the 1-D arterial segments.

Table 3. Pressure gradients at different locations, for the 1-D and 3-D models.

Segment	Gradient (mmHg/m) 1-D	Gradient (mmHg/m) 3-D
R. Subclavian B, Axillary, Brachial (7)	6.2	10.4
L. Common Carotid (15)	3.0	3.7
L. Internal Carotid 16)	14.0	25.3
L. Femoral (46)	1.8	1.3
L. Middle Cerebral M1 (73)	53.5	123
L. MCA M2 Superior Branch Distal Sylvian bifurcation (74)	250	600

The 3-D pattern of the mean wall shear stress (WSS) derived from CFD simulations with non-Newtonian blood viscosity is shown in Fig 3. WSS is a main contributor to pressure gradient, and also a physical parameter of importance for vascular wall metabolism and pathology. We observe that in

most location along the systemic arterial tree mean WSS is in the range of 1-2 Pa, which is in accordance with literature (Cheng, Helderman et al. 2007). WSS increases in the vessels of the celiac trunk and at some distal arteries of the upper limbs and cerebral circulation, where WSS values reach 8-10 Pa.

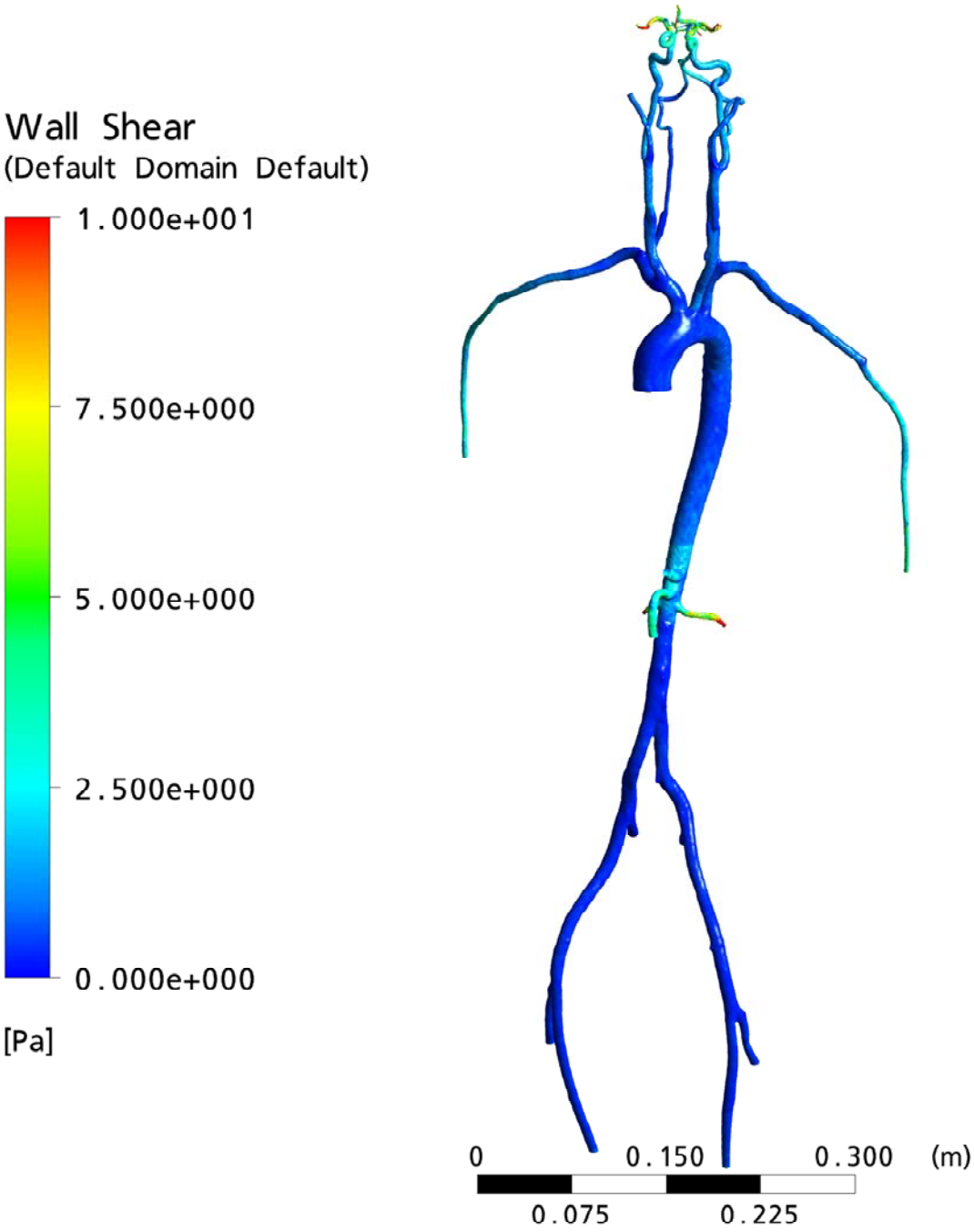

Figure 3. Wall shear stress pattern computed from steady 3-D CFD simulation. With non-Newtonian blood rheology

The largest difference in the mean pressure between 1-D and 3-D simulations occurred in the cerebral circulation (Fig 3), which is also the part of the arterial tree with the highest geometrical complexity, as manifested by the presence of anastomoses, high tortuosity and non-planarity. Figure 4 shows streamlines computed with the 3-D model along the left internal carotid artery (LICA) to the left middle cerebral artery (LMCA), and brings into evidence the truly complex flow patterns existing

in these vessels. In consequence, it may be expected that in the cerebral vasculature the WSS computed by the 3-D model will be substantially different and higher than the one computed using Womesley's theory. To illustrate the above, Figure 4 (insert) shows also the comparison between the mean wall shear stress predicted by the 1-D model at a specific point in the LMCA to the WSS distribution along the circumference of the same cross-section of the LMCA. We observe significant variations of the WSS around the circumference and that, overall, the WSS computed by the 3-D model is substantially higher than the WSS of the 1-D model. The peak difference is 118 % higher and on average WSS predicted by the 3-D model is +48 % higher than the mean WSS of the 1-D model.

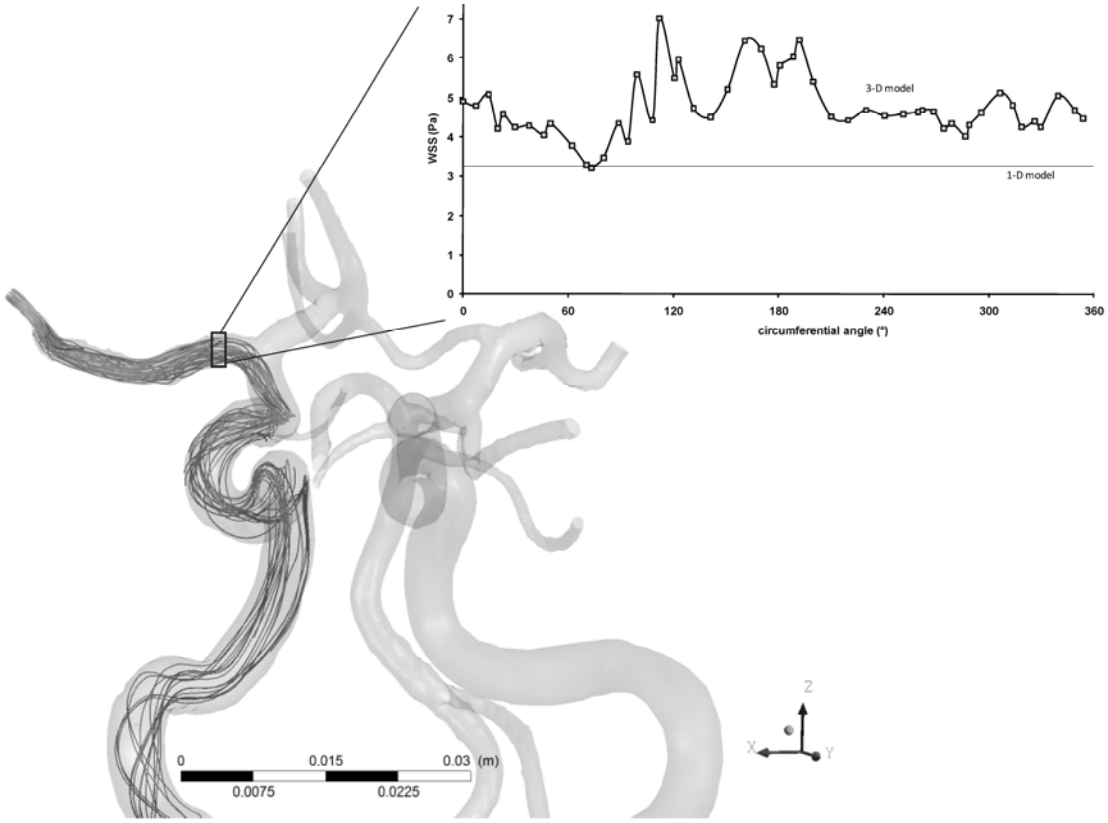

Figure 4. Streamlines computed by the 3-D model in the internal carotid (LICA) and left middle cerebral artery (LMCA). 3-D steady wall shear stress along the circumference of a cross-section of the LMCA is shown in the insert and compared to mean 1-D WSS averaged along the cardiac cycle.

DISCUSSION

Pressure drops are small in main central aorta and well reproduced by the 1-D model. After 0.4 m along the aorta the pressure drop was 0.5 mmHg, compared to the value of about 1.5 mmHg computed by Olufsen et al. (Olufsen, Peskin et al. 2000) for another patient-specific model. In mid size brachial artery (RBRA), pressure drop difference is still small between 1-D and 3-D models (especially with the Newtonian blood simulations), typically less than 0.5 mmHg. The difference starts to become substantial, i.e. larger than 0.8 mmHg at the middle of the brachial artery. There is one geometrical reason that may partially explain this: in the 1-D model, the cross-section area was assumed to decrease linearly between the proximal and distal end of the brachial artery (linear tapering), whereas the actual geometry, as measured by MRI and used in the 3-D simulations, is slightly different and the tapering is not constant. An additional run of the 1-D model with geometry and tapering adapted to correspond to MRI measurements has shown a pressure drop evolution closer to the one computed by the 3-D model (data not shown). Thus, a possible improvement of the 1-D model tapering descriptions is to consider other (i.e., nonlinear) descriptions of the decrease of the lumen area, as for instance, exponential form suggested by Fung Y.C (Fung 1984).

The losses are significant and only partially reproduced by the 1-D model in distal arteries and especially in precerebral and cerebral arteries. From the distal section of the ICA and into the circle of Willis and its branches, the blood flow presents complex patterns, as exemplified for part of the tree in Figure 4. Complex flow patterns lead not only to non-uniform WSS distribution at each cross-section, but also to increased WSS levels overall, contributing thus to augmented frictional losses. At the proximal cross-section of the LMCA, WSS from the 1-D model, averaged along the cardiac cycle, is equal to 3.22 Pa. Mean spatial WSS from the 3-D model is 4.76 Pa (+48 % more than 1-D model). Such important differences in WSS can explain, to a large extend, the differences in mean pressure evolution in cerebral arteries seen in Figure 2C.

Nature of blood rheology, as expressed in the comparison between Newtonian and Non-Newtonian models, is not very significant in medium-large size vessels (Quarteroni, Formaggia et al. 2009). Differences of up to 1 mmHg occur in smaller peripheral vessels (brachial, cerebral arteries). Furthermore, the tapering angle has an important effect on pressure drops. For instance, a 1.0 degree of tapering for the LMCA augments the pressure drop over the entire length of the artery by 76%.

The inherent weakness in the 1-D model formulation is that WSS is derived from the velocity profile, which is unknown and thus approximations need to be made. An overview of the different approaches can be found in Reymond et al. (2009) (Reymond, Merenda et al. 2009) and in the review article by van de Vosse and Stergiopulos (van de Vosse and Stergiopulos 2011). In general, three main approaches are followed. In the first approach the velocity profile is written as the product of a radius dependent profile function, independent of time, times the mean velocity that depends on the time. The assumed velocity profile included flat, Poisseuille, power laws (Hughes and Lubliner 1973; Wilmink, Pleumeekers et al. 1998; Wan, Steele et al. 2002) or an assumed boundary layer (Olufsen, Peskin et al. 2000), all of which lacked the inertial effects yielding a phase shift between mean velocity and shear stress. The second approach involves the use of time periodic profiles based on Womesley's theory, which includes the inertial effects (Azer and Peskin 2007; Reymond, Merenda et al. 2009). A third approach, followed by Bessems et al. (Bessems, Rutten et al. 2007), is based on asymptotic solutions of the Stokes boundary layer. Clearly, all approaches no matter how elaborate in capturing the inertial effects, are limited to developed flows in straight tubes and cannot estimate the effects of three dimensional flow patterns on wall shear.

Different approaches were utilized for arterial bifurcation models. Continuity of total pressure, such that the energy inequality is satisfied, has been used in Azer and Peskin (Azer and Peskin 2007), Alastruey et al. (Alastruey, Parker et al. 2007), Formaggia et al. (Formaggia, Lamponi et al. 2006), Sherwin et al. (Sherwin, Franke et al. 2003). Simple pressure continuity without any losses across the bifurcation was used in Wan, Taylor et al. (Wan, Steele et al. 2002), Olufsen & Peskin (Olufsen, Peskin

et al. 2000), Stergiopulos et al. (Stergiopulos, Young et al. 1992), Papapanayotou (Papapanayotou, Cherruault et al. 1990), Hillen, Zagzoule and Marc-Vergnes (Zagzoule and Marc-Vergnes 1986), Raines et al. (Raines, Jaffrin et al. 1974), Schaaf and Abbrecht (Schaaf and Abbrecht 1972). Some authors implemented simple models for the pressure drop across bifurcations (Huo and Kassab (Huo and Kassab 2007), Meister (Meister 1983)). However Formaggia et al. (Formaggia, Lamponi et al. 2003) reported that the different approaches to model the continuity at bifurcation (pressure, total pressure) have a minor impact on the predicted pressures (<1%). Matthys et al. (Matthys, Alastruey et al. 2007) have implemented energy los considerations at bifurcations in a 1-D model and also reported minor effects in large arteries and less than 0.5% differences in the mean pressures. Losses at bifurcations which are not fully accounted in the 1D model are thus regarded as not important contributors to the mean pressure drop.

1-D model simulation was run considering arterial wall viscoelasticity. This additional source of energy loss, which is not considered in the 3-D CFD simulation, needs to be quantified in order to make a fair comparison. An additional simulation with the 1-D model, considering elastic arterial wall, was run and the pressure drop along the 3 centerlines computed (results not shown). The difference in the pressure drops with and without viscoelasticity was quantified. The maximum relative RMSD in the LMCA was less than 0.2%, which is not significant. We have thus concluded that viscoelasticity does not affect our main conclusions regarding the mean pressure drop.

CONCLUSIONS

We evaluated, on a patient-specific arterial tree, the mean pressure drop from central arteries to the periphery in an attempt to evaluate the underestimations by the 1D model simulations due to poor approximations in the frictional terms. To accomplish that, we ran an unsteady 1-D and a steady 3-D simulation of flow in an extended patient-specific arterial tree obtained from angiography MRI in a young healthy adult. We also assessed the level of error in pressure drops comparing a distributed 1-D model to a 3-D CFD model. Pressure drops are small in central arteries and well reproduced by the 1-D model. In smaller peripheral and specifically in precerebral and cerebral arteries, the losses are more significant and are only partially reproduced by the 1-D model. Three-dimensional flow effects attributed to the 3-D geometry lead to an increase wall shear stress, which in the 1-D model is consistently underestimated. In consequence, the 1-D model overestimates mean pressure in peripheral arteries and this overestimation maybe substantial in certain applications, especially when modeling cerebral arterial flow.

ACKNOWLEDGMENTS

This work was supported in part by the European Commission integrated program IST-027703 (@neurIST Project) and by the Center for Biomedical Imaging (CIBM) of the Geneva-Lausanne Universities, the EPFL and the University Hospitals of Geneva and Lausanne. We acknowledge also the support of Strokelab SA for parts of the 3-D computational work.

PAPER IV PHYSIOLOGICAL ASPECTS OF FLUID STRUCTURE INTERACTION AND ITS EFFECT ON BLOOD FLOW IN A PATIENT-SPECIFIC AORTA

Philippe Reymond[1], Paolo Crosetto[2], Simone Deparis[2],
Alfio Quarteroni [2, 3] and Nikos Stergiopulos[1]

[1] Laboratory of Hemodynamics and Cardiovascular Technology
Ecole Polytechnique Fédérale de Lausanne, Switzerland
[2] CMCS-MATHICSE, Ecole Polytechnique Fédérale de Lausanne, Switzerland
[3] MOX, Department of Mathematics, Politecnico di Milano, Italy

INTRODUCTION

Patient-specific models of the circulation are increasingly used, as better representations of clinically relevant models (Perktold and Rappitsch 1995; Gerbeau and Chapelle 2005; Quarteroni, Formaggia et al. 2009; Taylor and Figueroa 2009). They are for instance utilized to assess the aneurysm risk of rupture, to plan a surgical procedure, to predict the outcome of a treatment, to mention a few. The reproducibility of patient-specific hemodynamic simulations has been advocated in the literature (Radaelli, Augsburger et al. 2008), with the authors claiming confidence in results provided by numerical simulation of cerebral aneurysms. Such patient-specific approaches may lead in the future to novel diagnostic and treatment planning tools.

To date, the different approaches to study arterial blood flow in-silico include lumped models, 1-D models, 3-D CFD (rigid vessels) and 3-D FSI (compliant vessels) models. They are all complementary and chosen according to the required level of detail, the extension of the region to consider, etc. For instance, lumped or 1-D models are still the models of choice to study pressure and flow wave propagation in extensive regions of the circulatory tree. Even though 1-D models do not model detailed flow patterns, they have been shown to produce good quantitative and qualitative predictions of pressure and flow rate waveforms at most of the locations of the arterial tree (Reymond, Merenda et al. 2009). They are also easier to couple with other zero-order models, like left ventricle models or models for distal vasculature.

In contrast to 1-D models where gross features of flow (i.e., pressure and flow) are studied, 3-D CFD models are used to obtain details of the flow patterns in specific arterial locations of particular physiological or pathological interest, such as at bifurcations (Taylor, Hughes et al. 1998), at the aortic arch, abdominal aorta (Taylor, Hughes et al. 1998), in abdominal aneurisms or cerebral aneurisms (Cebral, Castro et al. 2005) to name a few. In the majority of these studies the wall is considered as rigid, solving thus only the 3-D fluid problem and assuming that the wall motion does not affect the flow field significantly. This assumption simplifies the numerical approach and is fully justifiable only in the cases where the wall motion is relatively small. However, when important arterial wall deformations are encountered during the heart cycle, such as in the order of 10-15% for the aorta, it becomes essential to consider the deformation of the arterial wall. A fluid-structure interaction (FSI) approach is necessary to address this issue. FSI modeling for a patient-specific vasculature is still a very complex task to handle and is computationally expensive. However, the development of the automated meshing processes in conjunction with the use of more efficient parallel algorithms (Crosetto) renders the FSI approach applicable in the research or even clinical framework.

In the present study, we constructed a 3-D FSI model of a patient-specific aorta and its main branches. Fluid mechanics equations surrounded by a deformable arterial wall are solved utilizing the open source finite element parallel library LifeV (http://www.lifev.org).

The results of the FSI simulations are compared to its CFD (rigid walls) counterpart. We discuss how relevant is the elasticity of the wall to predict parameters of clinical importance, such as the wall shear stress (WSS). We also assess the differences between the 1-D and the 3-D FSI models in terms of their predictions of wave propagation characteristics along the aortic trunk.

METHODS

Mathematical formulation and numerical methods related to the solver are detailed in (Crosetto, Reymond et al. 2010) Blood is considered as a Newtonian fluid, a commonly accepted assumption for aorta flows (Quarteroni, Formaggia et al. 2009) with a density of 1'000 (kg m^{-3}) and a dynamic viscosity of 0.0035 (Pa s).

Angiography

To obtain a 3-D representation of the arterial lumen (interface between arterial wall and the blood), we performed MRI Time of Flight acquisition on a 3T MRI scanner (Siemens Trio-Tim 3T System). Details on the sequences utilized are given in (Reymond, Bohraus et al. 2011).

Geometry segmentation

The arterial tree geometry was reconstructed in 3-D from the raw dicom medical images (ITK Snap). After pre-processing of the dicom images, using gradient diffusion, a growing region based on contrast threshold was obtained. This served as a starting surface for an improved segmentation using an edge detection method based on intensity gradients.

Meshing of arterial wall geometry

We first created a surface of the lumen from the geometric surface that we previously segmented using ICEM CFD 11 (ANSYS Inc., Canonsburg, PA). The inlet and outlet surfaces were defined (Fig. 1). MRI imaging does not yield arterial wall thickness. We based our estimates of aortic wall thickness on human ex-vivo measurements carried out by Langewouters et al. (Langewouters 1982), who performed thickness, h, and outer diameter, D_e, measurements on human thoracic aortas and reported thickness to arterial diameter ratio as a function of age and location:

$$\frac{h}{D_e} = a + b \cdot age = c \tag{1}$$

The thickness varies spatially and is proportional to the local lumen diameter. The reported value of this ratio (c) is 0.054 for the thoracic aorta and 0.070 for the abdominal aorta for a 30 yrs old male. We used the mean value of these two aortic locations for the whole simulation domain, i.e. we assumed that ratio remains constant. Therefore the thickness to lumen diameter that we assumed for the entire aorta in the model was

$$\frac{h}{D_{lumen}} = \frac{c}{1-2c} \approx 0.071 \tag{2}$$

.

The lumen diameter, D_{lumen}, was deduced from the local distance between vessel centerline and arterial lumen mesh elements. The thickness was set locally in the normal direction, varies spatially and decreases when moving downstream, following the variation of the diameter.

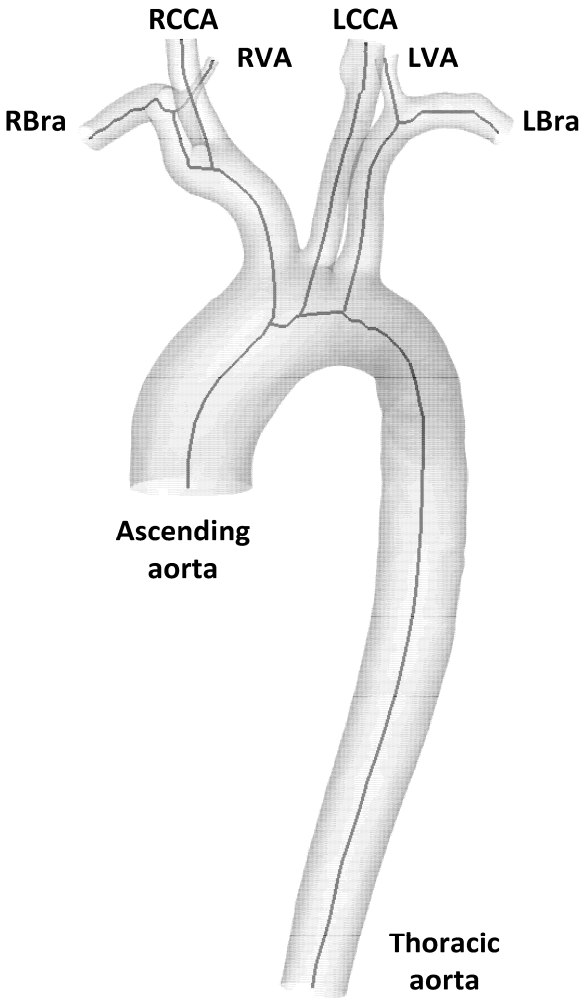

Figure 1. 3-D representation of the lumen of the aortic arch and its principal branches. It consists of 1 inlet (ascending aorta root) and 7 outlets (Common Carotid Artery CCA, Vertebral Artery VA, Thoracic aorta and Bra that stands for distal subclavian, axillary and brachial arteries region). The centerlines of the vessels used for the estimation of arterial diameter and wall thickness are also shown.

The centerline of the arterial tree was computed using the Aneufuse software developed within the framework of the EU Project @neurIST. For the arterial wall, a script in Matlab (Mathworks, Natick, Massachusetts) was developed to build a variable thickness solid mesh growing from the lumen interface surface. The mesh was constituted of 3 layers of prismatic elements (Fig. 2). Prismatic elements were further transformed to tetrahedral elements to meet the requirements of the solver. An unstructured tetrahedral mesh was then generated for the fluid region using Gambit (Fluent, ANSYS Inc.). The nodes of the solid and fluid regions were matching at the interface.

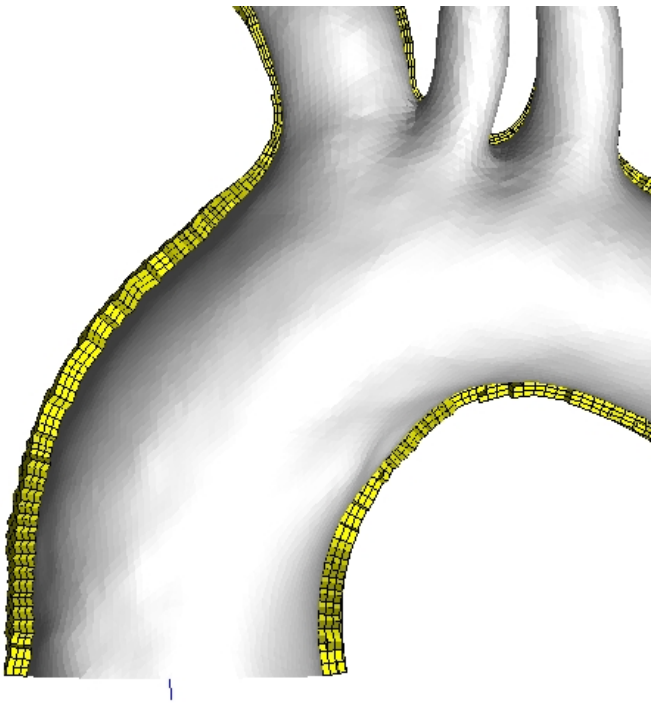

Figure 2. Arterial wall mesh cut representation. The mesh has a variable thickness, proportional to the local lumen diameter of the vessel. In this example, the mesh contains 3 layers of prismatic elements, which are later replaced by tetrahedral elements, in order to be compatible with the LifeV solver.

Boundary conditions

Pressure waveforms at the ascending aorta are usually not available non-invasively and flow waveforms were not available for all the outlet locations, we obtained the required inlet and outlet boundary waveforms from the 1-D model. This simulation solves the one-dimensional form of the fluid-structure equations modeling the entire arterial tree (Reymond, Merenda et al. 2009). It includes the main systemic arteries as well as a detailed description of the cerebral circulation. A non-linear viscoelastic constitutive law for the arterial wall was considered. The 1-D model has been validated qualitatively and quantitatively on the same person (Reymond, Bohraus et al. 2011). Mean flow rates at each inlet and outlet are summarized in table 1.

Table 1. Mean flow rate over a heart cycle, they are given for all the inlet and outlets of the 3-D domain.

	Segment	Mean flow rate (ml/s)		Segment	Mean flow rate (ml/s)
Ascending aorta	1	100.78	R Brachial	7	5.47
Thoracic aorta	27	76.60	LCCA	15	5.18
RCCA	5	5.58	LVA	20	1.14
RVA	6	1.23	L Brachial	21	5.57

Arterial outer wall constraint

To mimic the mechanical effect of surrounding tissue, we implemented a constitutive relation that relates the stress, σ^s, on the outer arterial wall surface to the displacement ds,

$$p_0 n + \sigma^s \cdot n + \alpha d_s = 0 , \quad (3)$$

where n is the outward normal vector and the coefficient α was adapted empirically to obtain physiological arterial wall displacements. More details are reported in (Crosetto, Reymond et al. 2010).

Arterial wall elastic properties

The arterial wall constitutive relation is linear elastic and isotropic. Although this seems a quite restrictive assumption, it is appropriate for the range of physiological intra arterial pressures (Quarteroni, Formaggia et al. 2009). A more detailed discussion on that specific point is reported in Crosetto et al (Crosetto, Reymond et al. 2010). We use a constant Young modulus of 0.4 MPa. According to the adapted Moens-Korteweg equation, the relationship between the incremental elastic modulus, E_{inc}, and the pulse wave velocity PWV (McDonald, Nichols et al. 1990) is given by:

$$PWV = \sqrt{\frac{E_{inc} h}{\rho D (1 - \sigma^2)}} \quad (4)$$

where σ = 0.5 is the Poisson coefficient of the arterial wall. We obtained PWV that are in the range of 5-6 m/s, which are typical values for young person aortas.

Analysis and model comparison

The temporal variation of the WSS along the cardiac cycle, at pathologically relevant locations, was compared for both FSI and CFD approaches. Indeed aortic arch region, subject to perturbed flow patterns, is prone to atherosclerotic plaques formation (Cheng, Tempel et al. 2006). A region in the more straight thoracic aorta, with less secondary flows, was considered as a control case in our study. A comparison of pressure and flow waveforms with the specific 1-D model is presented as well. The number of consecutive heart cycles simulated is a compromise between the high computational cost and periodical criteria of convergence. 3-D FSI simulations were run for 3 consecutive heart cycles (8h per cycle using 64 MPI processes on the Cray XT4 UK National Supercomputing Service HECToR) with a time step of 1 ms.

RESULTS

Compliant vs. rigid vessels comparison

We performed a rigid wall simulation with the same geometry imposing the same physiological boundary conditions as in FSI. Pressure waveform was imposed at the inlet and flow waveforms at all the outlets. Figures 3.A and 3.B present the WSS patterns at 3 different representative instants during the cardiac cycle for CFD and FSI, respectively. The range of WSS obtained was 20 dyn/cm^2 for CFD and 14 for FSI.

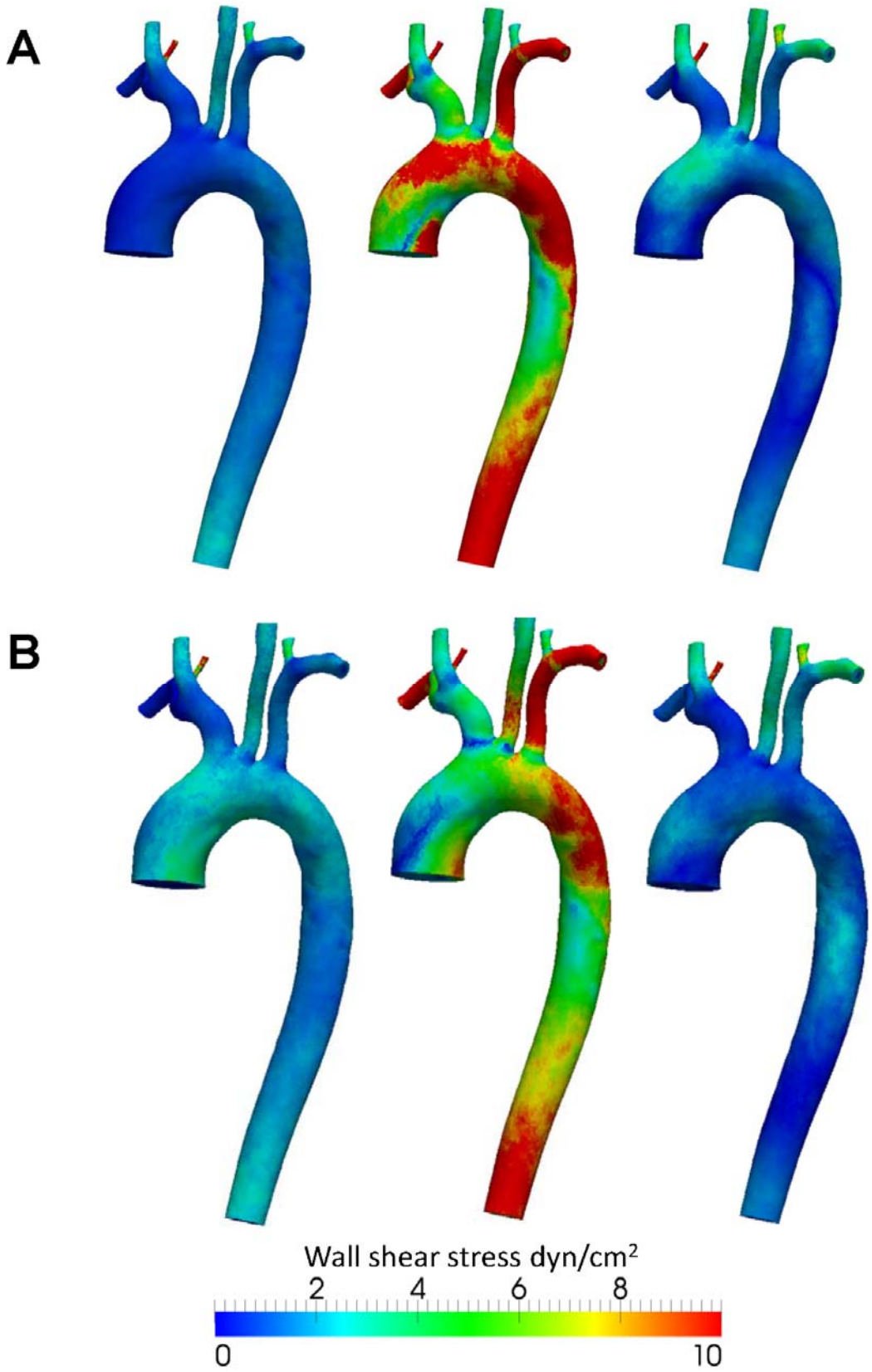

Figure 3. Wall shear stress magnitudes predicted by CFD with rigid walls (A) and FSI (B) simulations. 3 different instants along the cardiac cycle representative of end diastole, mid systole and mid diastole phases are chosen, at 80, 290 and 550ms respectively (fig. 5).

Because of the importance of the temporal variation of the WSS in endothelial function, atherogenesis and stability of plaques (DePaola, Gimbrone et al. 1992; White, Haidekker et al. 2001; Gambillara, Montorzi et al. 2005), we compared the WSS waveform along the cardiac cycle, as predicted by FSI and CFD simulations (Fig. 4). WSS is locally averaged in different regions of clinical interest. Indeed, the aortic cross where high vorticity flow and low WSS are present is more prone to atherosclerotic plaque formation (Cheng, Tempel et al. 2006). The 2 regions at the thoracic aorta level with less pronounced secondary flows and higher WSS are considered as control cases. Time-averaged values of the WSS of the different regions are reported in Table 2.

Table 2. Time averaged of WSS (dyn/cm^2) at different regions of the aorta. Values are reported for fluid structure interaction (FSI) and computational fluid dynamic (rigid walls) simulations.

	Aortic arch			Thoracic aorta	
	Lower	Middle	Upper	Interior	Exterior
Rigid walls CFD	2.4	3.7	2.6	3.7	4.3
FSI	2.7	2.2	1.9	3.5	3.3

We observe large differences in both the wave shape and in magnitude of WSS in the aortic arch region (Fig. 4, top figures). The largest difference in terms of peak WSS is found on the anterior lateral side of the aortic arch (Fig. 4, top mid figure), where CFD with rigid walls overestimates the peak WSS with respect to FSI by +135%.

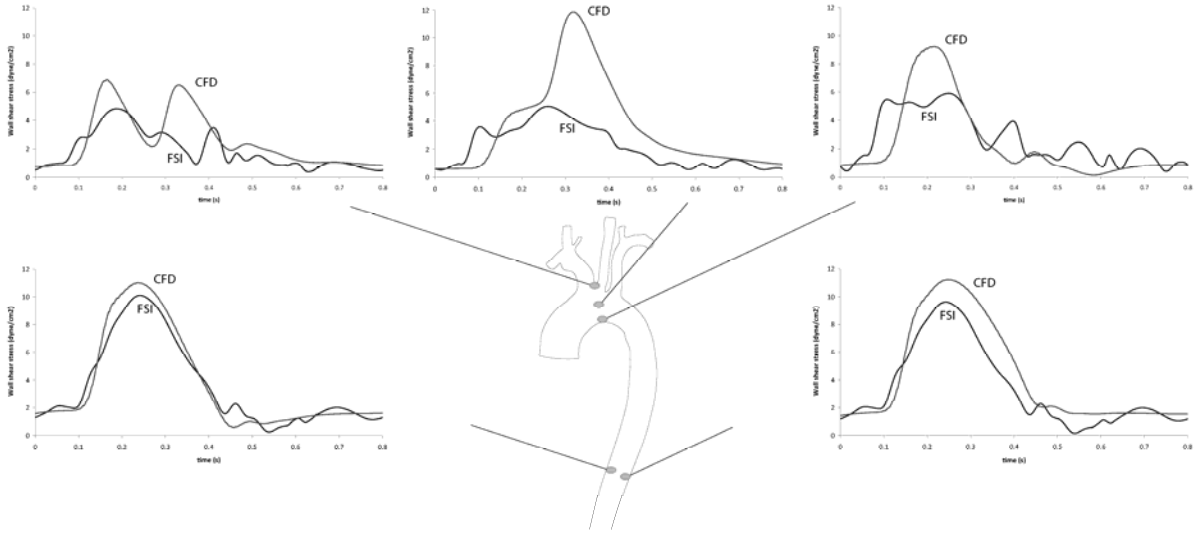

Figure 4. The temporal evolution of wall shear stress (dyn/cm2) is presented along the cardiac cycle at different locations, as predicted by FSI and CFD simulations. The region of interest at the aortic arch is in a cross section at the brachiocephalic-left common carotid bifurcation level (top) and in the thoracic aorta region (bottom).

FSI and 1-D model pressure and flow waveforms comparison

Another comparison that is certainly quite interesting, from a modeling point of view, is the comparison between the 3-D (FSI) and 1-D wave propagation models. In figure 5, pressure and flow waveforms obtained at 2 arterial locations, namely at the aortic arch and the thoracic aorta level, are shown and compared. The qualitative features of the pressure waveforms are in good agreement. The amplitude of the flow waveforms is slightly different, mainly in systole, at both the aortic arch and thoracic aorta level. Pressure and flow waves predicted by the FSI appear to arrive later at both the proximal and distal locations by 4-6 ms estimated by the foot-to-foot travel time method.

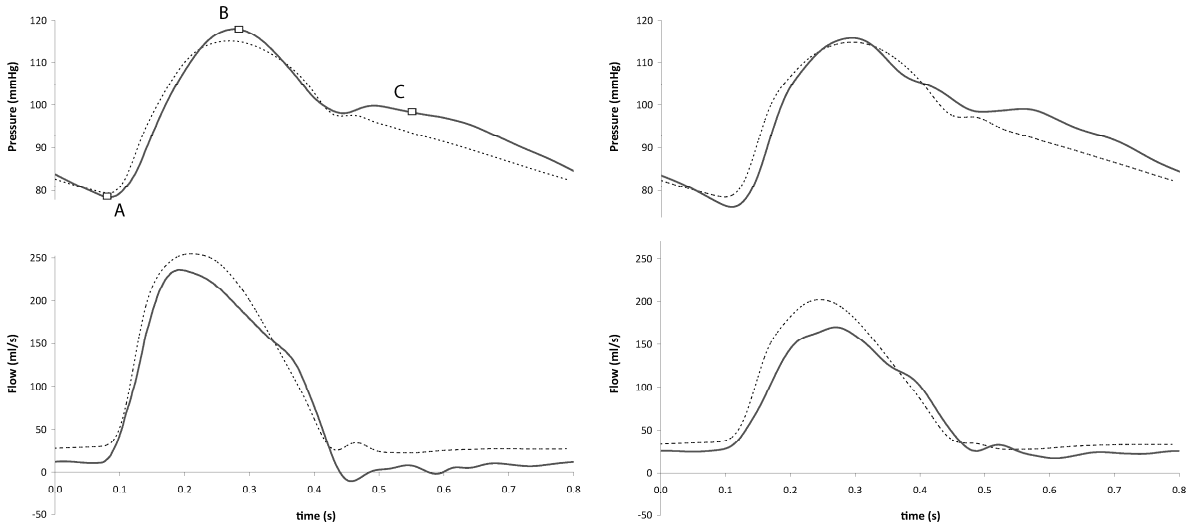

Figure 5. Pressure (top) and flow (bottom) waveforms computed by the FSI simulation (continuous line) and the 1-D model (dashed line) are presented. Locations are at the aortic arch (left) and thoracic aorta (right) and correspond to the regions drawn in figure 4. The set of boundary conditions imposed is flow for all outlets and inlet. The 3 representative instants selected for the WSS comparison are (A) late diastole 80 ms, (B) systole 290 ms and (C) mid diastole 550 ms and are distinguished in the left top panel.

DISCUSSION

We performed a fluid structure interaction simulation of blood flow circulation in a patient-specific aortic arch, imposing physiological boundary conditions. This model allows us to predict hemodynamic data of clinical interest in a real aorta geometry.

The effects or wall elasticity and the resulting fluid-wall motion coupling appear to be important, especially in the proximal aorta, where diameter expansion during the heart cycle reaches 10-15 %. CFD simulation of the same aortic geometry with rigid wall overestimates the WSS for large parts of the heart cycle (Fig. 4). Effect of wall elasticity was studied in cerebral aneurysm by (Torii, Oshima et al. 2007) and showed similar results. The wave shape of WSS is quite different between FSI and CFD simulation with rigid walls (Fig. 4), meaning that temporal gradients in WSS would be substantially different, especially in the ascending aorta. A number of studies have shown that both temporal and spatial gradients in WSS affect endothelial metabolism and maybe of importance in the predisposition of certain arterial locations to the development of endothelial dysfunction and in consequence of arterial disease (DePaola, Gimbrone et al. 1992; White, Haidekker et al. 2001; Gambillara, Montorzi et al. 2005). Figure 3 shows a spatial representation of WSS patterns at different characteristic time steps during an heart cycle. Although the patterns are qualitatively similar, visual inspection reveals that WSS patterns are substantially different in FSI and CFD with rigid wall simulations in the aortic arch region. These differences are further accentuated if spatial gradients in WSS are considered (data not shown). In contrast to the aortic arch, temporal and spatial distribution of WSS in the thoracic aorta appear to be quite similar when FSI and CFD with rigid walls are compared (Fig. 3 and 4). This is likely due to the relatively less important diameter expansion during the heart cycle in the thoracic aorta 7-10 % vs. 10-15 % in the ascending aorta, as the thoracic aorta is relatively less compliant and anatomically constraint in its radial motion by its surrounding structures.

As opposed to the CFD with rigid walls, the FSI model with the elastic wall lends itself in studying wave propagation phenomena. We compared the FSI predictions to 1-D model predictions, the latter being the gold standard in terms of wave propagation modeling in the arterial tree (van de Vosse and Stergiopulos 2011). We compared flow and pressure wave shapes and travel times at a proximal (aortic arch) and distal (thoracic aorta) site. FSI seems to predict a travel time at proximal and distal location close to the 1-D model, however the time shift is probably due to a difference in the location of the proximal boundary condition. Overall, FSI predicts pressure and flow wave shapes similar to those of the 1-D model. The largest discrepancies occur mainly in the shape of flow waveform at the aortic arch and thoracic aorta levels. The observed differences in wave shapes predicted by FSI and 1-D model maybe attributed, in part at least, to differences in boundary conditions and their implicit effects in wave reflections, especially at the termination sites of the model.

The boundary conditions at the terminations of the branches can be handled using many different strategies. The goal of such boundary conditions is to simulate the continuation of the artery, and thus to correctly treat the pressure waves reaching the artery termination effectively attenuating numerical artifacts. These boundary conditions are called absorbing boundary conditions and can be devised exploiting the hyperbolic nature of the limit case leading to the 1-D model formulation.

A promising method to avoid numerical reflection is the coupling of the 3-D FSI with reduced order models, in particular 0-D and 1-D models [Ch.10] (Quarteroni, Formaggia et al. 2009).

These strategies are being developed and tested in literature for FSI simulations in e.g. (Formaggia, Gerbeau et al. 2001; Nobile and Vergara 2007; Kim, Vignon-Clementel et al. 2009), however they involve an accurate tuning of coefficients which can depend on geometrical quantities.

In most of the applications the absorbing conditions imposed to the arterial terminations are assigned to the fluid problem, while homogeneous Neumann conditions are imposed to the structure.

In our computation we did not impose absorbing boundary conditions since the boundary integrated quantities (flow rate and pressure) were already available from measurements or from an independent 1-D simulation. We imposed fluxes as defective boundary conditions at all the terminations and Neumann homogeneous boundary condition on the vessel wall terminations. We did not observe numerical reflections with this choice.
Other physiological simulations were reported in the literature. For instance Kim et al. (Kim, Vignon-Clementel et al. 2009) utilized the coupled momentum method. They coupled a 3-D domain to a lumped model of the heart and terminated with Windkessel models. The arterial wall was modeled as a membrane with constant thickness and 6 cardiac cycles were required to meet convergence.
This approach has the advantage of being less computationally expensive; however it may reach limitations when arterial wall displacement becomes important.
The influence of using 2 different sets of physiological boundary conditions was done in (Crosetto, Reymond et al. 2010). The sets differ by the type of BC prescribed at the inlet. Either a pressure waveform, obtained through the 1-D model, or flow waveforms obtained from pc-MRI were imposed. A comparison with literature data, especially the pulse wave velocity (PWV), the arterial wall deformation and wall shear stress (WSS) shows good agreement between simulation results and physiological situation.

Limitations:
Boundary conditions of pressure or flows for the FSI model are prescribed from measurements or from the 1-D simulation. This approach may lead to non-physiological wave reflections arising from distal locations. An interesting alternative would be the use of the Windkessel model at each outlet (Kim, Vignon-Clementel et al. 2009). The material behavior of the arterial wall is currently linear elastic and isotropic. A nonlinear behavior may be of interest when simulating pathological situations. Model coefficients for the constitutive constraint on the outer arterial wall were tuned empirically. Coefficients directly derived from soft tissue mechanical properties should be envisaged. Only a region of the systemic arterial tree has been considered in this study. A more extensive region of the arterial tree may be considered in the future, especially to avoid non-physiological wave reflections.

CONCLUSION

A fluid structure interaction simulation, with physiological boundary conditions, has been performed on a patient-specific aorta. Clinical parameters of importance, like the wall shear stress, have been reported. Significant differences, compared to a simulation with rigid walls, are found. A comparison to an equivalent 1-D model shows that pressure and flow waveforms are in good agreement. This justifies the interest and relevance of an FSI approach in the clinical context, even though, at the time being, some difficulties, like complex geometry preparation, boundary condition imposition and long computational times, have to be overcome.

Acknowledgments

This work was supported by the by the European Commission contract no. IST-027703 @neurIST Project, by the Center for Biomedical Imaging (CIBM) of the Geneva-Lausanne Universities, the EPFL and the University Hospitals of Geneva and Lausanne. We acknowledge the support provided by the Swiss National Science Foundation under grant 200020-117587 and the European Research Council Advanced Grant "Mathcard, Mathematical Modelling and Simulation of the Cardiovascular System" Project ERC-2008AdG 227058. Support has also been provided by the VPH2 project FP7 224635, and by the DEISA Consortium (www.deisa.eu), co-funded through the EU FP7 project RI-222919, under the DEISA Science Community support programme.

PAPER V SYSTOLIC HYPERTENSION MECHANISMS: EFFECT OF GLOBAL AND LOCAL PROXIMAL AORTA STIFFENING ON PULSE PRESSURE

Philippe Reymond[1], N. Westerhof[2] and Nikos Stergiopulos[1]

[1] Laboratory of Hemodynamics and Cardiovascular Technology
Ecole Polytechnique Fédérale de Lausanne, Switzerland

[2] Dept. of Physiology, VU University Medical Center
Amsterdam, The Netherlands

INTRODUCTION

Loss in total systemic compliance leads to an increase in pulse pressure (PP) and, in consequence, to an augmentation of systolic pressure. This was proven by a large number of studies in animals (Randall, van den Bos et al. 1984; Ioannou, Stergiopulos et al. 2003) and in the human (Chemla, Hebert et al. 1998). The increase in PP, when compliance decreases, can be attributed to loss in windkessel function (Chemla et al., Stergiopulos et al. 1994; Stergiopulos et al. 1995; Stergiopulos and Westerhof, 1998). The windkessel model, however, does not account for wave propagation phenomena, which play also an important role in the development of systolic hypertension following arterial stiffening. The prevailing theory is that aortic stiffening leads to an increase in wave speed and in the amplitude of the reflected wave. The augmented reflected wave will therefore arrive at the ascending aorta earlier, during late systole, and it will be added to forward running wave leading to a substantial increase in systolic pressure (O'Rourke and Nichols 2005). This mechanism is evidenced by the characteristic change in the shape of the proximal aortic wave (Type A in stiff/aged aortas vs. type A in young/elastic aortas, see Murgo et al. (Murgo, Westerhof et al. 1980) and by an increase in the augmentation index (AI), which is non-dimensional wave shape index reflecting the relative contribution of the reflected waves on the pulse pressure. Numerous clinical studies have shown an increase in AI in presence of aortic stiffening and in aging.

A second mechanism by which aortic stiffening contributes to systolic hypertension has been proposed (Mitchell, Conlin et al. 2008). The underlying theory is that aortic stiffening would lead to an increase in the characteristic impedance of the proximal aorta, which means a proportional increase in the forward running pressure wave, if cardiac output is maintained. The characteristic impedance of the proximal aorta is estimated as $Z_c = \rho.c/A$, where ρ is blood density, c the local wave speed and A the local cross sectional area of the aorta. Hence, an increase in characteristic impedance of the proximal aorta can result from aortic stiffening (increase in wave speed c) but also from lower aortic diameter; hence arterial geometry is also thought to be a determining factor.

The two aforementioned mechanisms are distinctly different. The former is focusing on the effects of the reflected waves, whereas the latter is based on the augmentation of the forward wave. A careful look at the respective mechanisms shows that the former is sensitive to the increase in wave speed along the entire aortic trunk, whereas the latter it is based principally on the amplification of the forward pressure wave as the heart injects into a stiff proximal aorta. The goal of our present work is to analyze the two mechanisms by simulating the effects of aortic stiffening on aortic pressure using a 1-D model of the arterial tree. In order to do so we have considered aortic stiffening in two distinctly different manners: first, aorta is stiffened only locally in the proximal aorta region, thereby increasing the characteristic impedance of the aorta while at the same time decreasing total arterial compliance and, second, by stiffening uniformly the entire arterial tree.

METHODS

Brief description of the 1-D model of the arterial circulation

The 1-D model of blood flow in the arterial trees solves the integrated form of the momentum and continuity equations applied over each arterial segment. A non-linear viscoelastic constitutive law for the arterial wall was considered. The intimal shear stress and nonlinear convective acceleration terms are modeled using the Witzig-Womersley theory. All distal vessels are terminated with three-element Windkessel models to account for the resistance, R_T, and compliance, C_T, of the distal vascular beds. A detailed description of the mathematical formulation including governing equations and boundary conditions is presented in Reymond et al. (Reymond, Merenda et al. 2009).
This generic arterial tree model has been validated quantitatively with in-vivo measurements on a group of subjects. In a second study involving the same 1-D formulation, a patient-specific model was validated, giving further proof that the 1-D models can provide accurate predictions of pressure and flow in the entire systemic circulation.

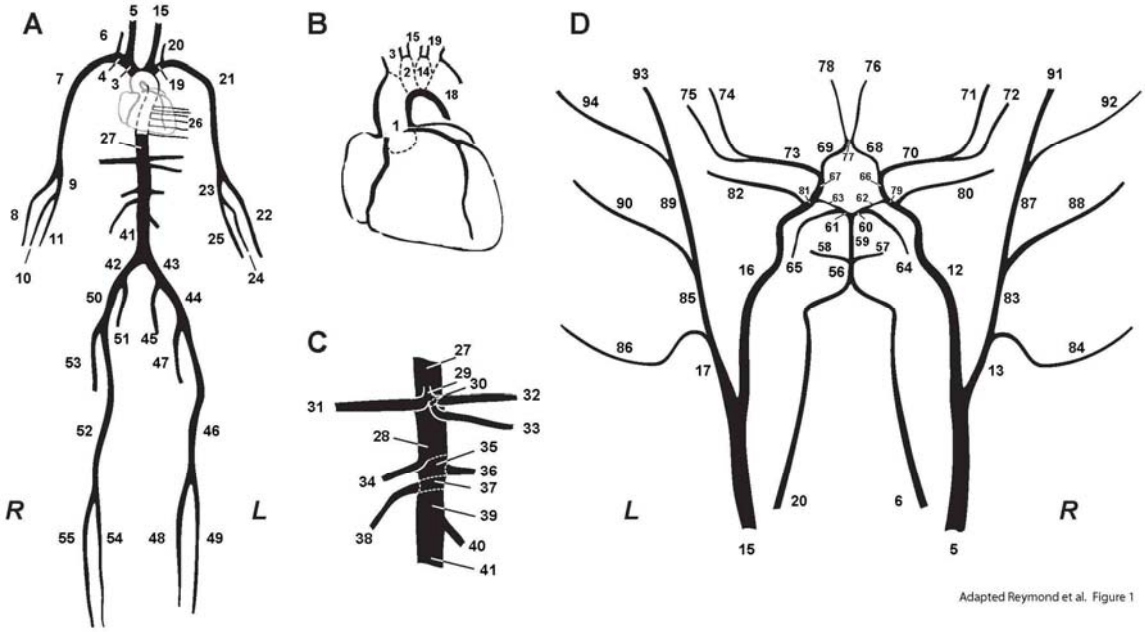

Figure 1 Schematic representation of the arterial tree, adapted from Reymond et al. (Reymond, Merenda et al. 2009). (A) Main systemic arterial tree, (B) Detail of the aortic arch. C) Detail of the principal abdominal aorta branches. (D) Schematic of the detailed cerebral arterial tree, which is connected via the carotids (segments 5 and 15) and the vertebrals (segments 6 and 20) to the main arterial tree shown in (A).

At its proximal end (root of the ascending aorta), the arterial tree was coupled to a model of the left ventricle based on the varying elastance model (VEM) (Fitchett 1991; Formaggia, Lamponi et al. 2006). Same varying elastance model parameters (normalized elastance curve, maximum elastance and time to reach maximum elastance were utilized for all simulations.

Local proximal aorta stiffening

The characteristic impedance, Zc, characterize the proportionality of pressure, P, to the flow, Q, in the early systole and in absence of wave reflection (McDonald, Nichols et al. 1990):

$$Z_c = \frac{\Delta P}{\Delta Q} \tag{1}$$

Zc may be estimated from the local area compliance C_A

$$Z_c = \sqrt{\frac{\rho}{A\,C_A}} \tag{2}$$

where ρ is the blood density, and A the cross-sectional area of the lumen.

We chose to increase the characteristic impedance by decreasing only the distensibility, $D_w=C_A/A$ of the proximal aorta (segments 1-95-2-14-18-27 Fig. 1) without changing the aortic dimensions. The remaining arterial tree segments kept the same elastic properties as the generic tree (control case). Terminal compliances, C_T, at distal ends were also conserved. Distal resistances, R_T, however, were increased by +21 % to obtain the same diastole pressure as the control case. This was done in accordance to the results of in vivo studies, where acute decrease in compliance were always accompanied by increase in peripheral resistance as to preserve diastolic pressure and, in consequence, coronary perfusion (Ioannou, Stergiopulos et al. 2003; Ioannou, Morel et al. 2009).

Global stiffening of the arterial tree

Global stiffening was achieved by decreasing distensibility of all arterial segments by 40 %. The level of decrease in distensibility was found by trial and error, the criterion being the same proximal aorta pulse pressure as the one obtained with local stiffening. Distal Windkessel compliances, C_T, were decreased in proportion to keep their relative contribution to the total compliance the same as for the control case. Distal resistances, R_T, were also adapted to keep diastolic at control levels, as was done for the case of local stiffening.

Analysis

The characteristic impedance at the root of the ascending aorta is estimated as the average value of the modulus of the input impedance in the frequency range of 4-10 Hz. **Total** pressure waves were separated into forward, P_f, and backward (reflected), P_b, wave components using the formulas (Westerhof, Sipkema et al. 1972):

$$P_f = \frac{P + Z_c Q}{2}, \tag{3}$$

$$P_b = \frac{P - Z_c Q}{2} \tag{4}$$

RESULTS

Figure 2 shows pressure and flow waveforms at the proximal ascending aorta for the control case as well as for the case of local and global stiffening. We observe that although both types of stiffening lead to the same increase in PP, the shapes are different.

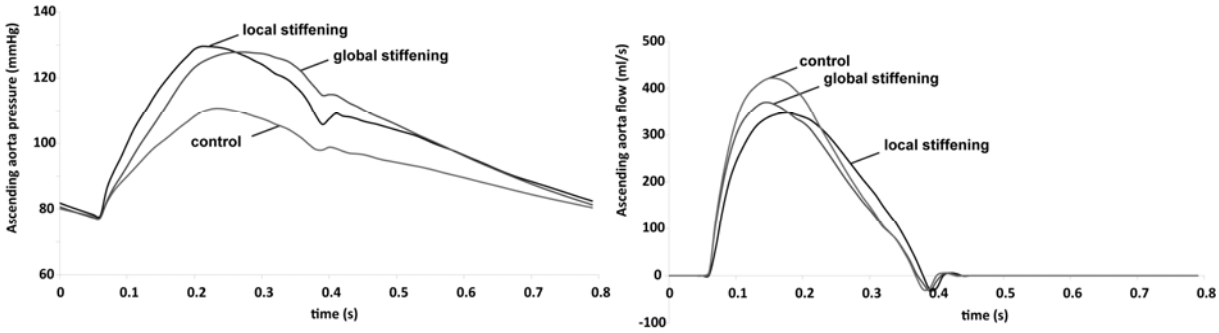

Figure 2 Pressure (left) and flow (right) waveforms at the proximal ascending aorta level. They are drawn for the control case, local and global stiffening of the arterial tree.

Important hemodynamic parameters are given in Table 1. Cardiac output, systolic, mean and pulse pressure at the root of the ascending aorta are reported. Total compliance is the sum of volume compliance of the arterial segments included in the 1-D model and the compliance of the terminal Windkessel.

Table 1 Hemodynamic values of the 1-D model simulations for the control case, local aortic stiffening and global arterial tree stiffening.

	Original arterial tree (control)	LOCAL proximal aorta stiffening	GLOBAL arterial tree stiffening
PP (mmHg)	33	52 (+ 58 %)	51
MAP (mmHg)	94	103.6 (+ 10 %)	103.3
$PP_{forward}$ (mmHg)	22	42 (+ 91 %)	31 (+ 41 %)
$PP_{backward}$ (mmHg)	12	16 (+ 33 %)	22 (+ 83 %)
$PP_{backward}$ / $PP_{forward}$ (-)	0.55	0.38	0.71 (+ 30 %)
Cardiac Output (ml/s)	98.5	90.8	88.3
Total compliance (ml/mmHg)	1.33	0.76 (- 43 %)	0.70 (- 47 %)
Arterial compliance (ml/mmHg)	1.04	0.47	0.55
Distal compliance (ml/mmHg)	0.29 (+ 22 %)*	0.29 (+ 38 %)*	0.15 (+ 21 %)*
Zc (mmHg s/ml)	0.034	0.10 (+ 194 %)	0.042 (+ 24 %)

PP: pulse pressure, MAP: mean arterial pressure, Zc: characteristic impedance. Relative differences are referred to the control. Distal compliance is the compliance of all the distal small arteries, arterioles that are modeled with Windkessel and (*) is the relative contribution of distal compliance to total compliance.

Effects of local stiffening of the aortic arch

Pulse pressure increased by 58 % in presence of a stiff proximal aorta. To keep the same diastole pressure as the control case, distal resistances, R_T, were increased by +21 %. MAP was increased by 11 %. Total compliance decreased by 43 %. Distal compliance was the same as for the control case in absolute value, however, due to the decrease of the arterial compliance, its contribution to the total compliance increased. Characteristic impedance presents the highest change and reached almost 3 times the control value.

Global stiffening of the arterial tree

To keep the same diastole pressure as the control case, distal resistances, RT, were increased by +25 %. MAP increased by almost the same amount as for local stiffening. On the same token, global stiffening lead to similar decrease in total arterial compliance as for local stiffening (-47 % vs. -43 %, respectively), which is an expected result since both stiffening approaches were forced to yield the same pulse pressure and the cardiac output did not very much (90.8 ml/s for local stiffening vs. 88.3 ml/s for global stiffening). Compared to the control case, distal compliance was decreased by almost a factor 2 (0.29 to 0.15 ml/mmHg), to keep its contribution to the total compliance around 21-22 % as it was in the control simulation. In contrast to local stiffening, characteristic impedance increased moderately (+ 24 %) compare to the control value.

Analysis of forward and backward (reflected) waves

The forward and backward components are presented in Figure 3, for the control case as well as the case of local and global stiffening. In presence of a locally stiff proximal aorta, it is the forward wave that is substantially amplified (amplitude of forward wave 42 mmHg, vs. 22 for control, Figure 3, left). In contrast, the reflected wave is not amplified in proportion to the forward wave (amplitude of reflected wave 16 mmHg vs. 12 in control, Figure 3, right). Furthermore, the time of arrival of the reflected wave is practically unaltered and its contribution to early systolic pressure is essentially the same as in control (compare ascending part of the reflected wave between control and local stiffening, Figure 3, right). Hence, it is quite clear that the main reason for the increase in PP in presence of local stiffening of the ascending aorta is the amplification of the forward wave.
The picture is quite different in presence of global aortic stiffening. As clearly seen in Figure 3, the forward wave is amplified by 41 % but at the same time the reflected wave is also amplified by 83 % with respect to control. Furthermore, as seen in Figure 3 (right), the amplified reflected wave arrives in the root of the ascending aorta earlier, thereby contributing more to early systolic pressure. It is therefore clear that in a globally stiff aorta the reflected wave is a major contributor to the augmentation of systolic and pulse pressure.

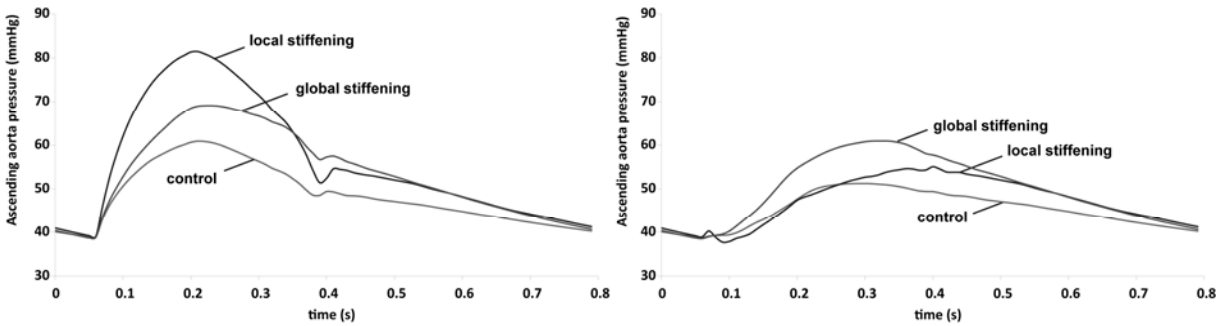

Figure 3 Forward (left) and backward (right) pressure wave components at the root of the ascending aorta level.

DISCUSSION

The fact that arterial stiffening, as a result of ageing or arterial disease, leads to increase in pulse pressure and systolic hypertension is widely accept and support by numerous clinical studies. The exact mechanism by which this happens is still a controversial topic (Vasan 2008). Perhaps the most widely accepted line of thinking is that arterial stiffening increases wave speed and thus reflected waves, often larger in amplitude, arrive earlier in systole adding themselves to the forward wave, thereby augmenting pulse pressure and systolic pressure (O'Rourke and Nichols 2005). The presence of a significant reflected wave in early systole is often seen in pressure recordings as a pronounced late systolic peak, usually quantified by means of the Augmentation Index (AI), defined as the ratio of the amplitude of the late systolic peak to pulse pressure. A large number of studies have shown the link between arterial stiffness and AI, contributing thus to a wider use of AI as a useful non-dimensional index relating systolic hypertension to arterial properties (stiffening) and to physiological (i.e., ageing) or pathological (i.e., hypertension, arteriosclerosis) processes affecting wave speed and reflections.

A different line of thinking has been recently proposed, according to which systolic hypertension could be primarily due to amplification of forward waves when the heart ejects into a stiff proximal aorta, rather than to augmentation and earlier arrival of reflected waves. Mitchell et al. (Mitchell, Conlin et al. 2008) performed noninvasive pressure and flow measurements on subjects with systolic hypertension, and concluded that systolic hypertension is primarily due to an increase in wall stiffness and reduced aortic diameter rather than early wave reflection. Indeed, an increase in ascending aortic stiffness or a decrease in its diameter would both lead to an increase in characteristic impedance, in accordance to $Z_c = \rho.c/A$, c being the local wave velocity. By definition, characteristic impedance is equal to the ratio of pulsatile pressure to pulsatile flow in absence of reflection ($Z_c = \Delta p/\Delta Q$). Hence in early systole, where reflections have not yet arrived from the periphery, the pressure increase Δp in the early systolic phase will be essential equal to Δp of the forward wave and by virtue of the equation defining characteristic impedance $\Delta p = Z_c * \Delta Q$. If cardiac output is maintained so that ΔQ is no affected by stiffening, then the up rise in pressure in early systole will be proportional to the increase in characteristic impedance and a major contributor to systolic hypertension.

We find that both mechanisms have their merit because they are based on physically sound principles. We hypothesized that the relative importance of each mechanism depends on the "topology" of arterial stiffening or geometrical alterations taking place in ageing or disease. To elucidate this point we have considered and simulated using a realistic model of the arterial tree two rather extreme cases: one in which arterial stiffening is uniformly applied to all arterial segments and peripheral beds (global stiffening) and one in which stiffening is applied only to the proximal aorta region (local stiffening). The simulations and analysis of the results showed in a rather clear and direct way the anticipated differences in the two mechanisms contributing to systolic hypertension. Under global stiffening, both the forward and backward running waves are augmented in amplitude. The relative increase in the amplitude of the forward wave is 41 %, which, in part at least, is due to the increase in characteristic impedance of the proximal aorta (+ 24 %). The amplitude of reflected wave is increased by 83 %, indicating an increase in wave reflection coefficient by 30 %. The arrival of reflected waves earlier in systole is clearly shown in Figure 3 (right). As seen in Figure 3 and concluded earlier, in presence of global stiffening the reflected waves do contribute to systolic hypertension, although the amplification of the forward wave is also an important contributor as well.

When we stiffened the proximal aorta only in a manner as to attain the same pulse pressure as for global stiffening, the amplitude of forward wave was amplified by 91 %, whereas the amplitude of the reflected wave was increased only by 33 %, indicating a ratio of backward to forward wave amplitude of 0.38, which is actually lower than control (0.55). It is likely that reflected waves traveling backwards along the thoracic aorta are re-reflected at the distal end of the stiff aortic arch, thus never reaching the root of the ascending aorta.

In our numerical simulations, stiffening of the proximal aorta led to a 3-fold increase in characteristic impedance, a 43 % decrease in total compliance and a 58 % increase in pulse pressure. These results agree well, at least in a qualitative sense, with the in vivo experiments by Ioannou et al. (Ioannou, Stergiopulos et al. 2003; Ioannou, Morel et al. 2009). Ioannou et al. placed a non-compliant Dacron sleeve around the aortic arch of swines, thereby decreasing substantially the local aortic compliance. Two days after the operation, they reported an increase in PP by 86 % and a decrease in total arterial compliance by 50 % while the characteristic impedance of the proximal aorta increased to 2.5 times its control value. Ioannou et al also showed that the increase in pulse pressure was mainly attributed to the large increase (+96%) in the forward wave. Both studies confirm that stiffening of the proximal aorta only has a major impact on the total arterial compliance, providing further support on the commonly accepted fact that most of the total systemic compliance resides in the proximal aorta region (Stergiopulos, Segers et al. 1999).

It is of interest to note that in both local and global stiffening a similar decrease in total arterial compliance (- 43 % in local vs. -47 % in global stiffening) led to a similar increase in PP (52 % in local vs. 51 % in global stiffening). So despite distinctly different effects on the forward and back running wave components the loss in compliance appears to lead to the same level of PP increase. This seems to suggest that, overall and by enlarge, what determines the increase in PP is the loss in compliance and the exact topology defining where the decrease in compliance takes place (local vs. uniformly distributed along the entire arterial network) plays a secondary role. In other words, the windkessel effect prevails and defines PP for a given ejection volume. This was exactly the finding of (Chemla, Hebert et al. 1998) and the conclusion of (Stergiopulos and Westerhof 1998). Stergiopulos and Westerhof showed that, for a given ejection volume, PP can be completely and very precisely determined by only two arterial parameters: total arterial resistance, R, and total arterial compliance, C. The explanation is the PP is primarily determined by the low frequency components of the pulse (first 3 to 4 harmonics) and for these frequencies the 2-element windkessel provides and very faithful description of the input impedance of the arterial system (Stergiopulos, Meister et al. 1994). This seems to be a paradoxical finding, because the windkessel model neglects wave phenomena, which apparently play an important role in shaping aortic pressure and augmenting systolic pressure in presence of stiffening, yet the windkessel model predict PP in a very precise manner and that in presence or absence of strong reflections (Stergiopulos and Westerhof 1998).

We have limited our simulations to changes in arterial compliance and we have not touched upon changes in geometry. From a theoretical standpoint, changes in geometry will also impact on wave transmission properties and will affect wave speed and characteristic impedances. Mitchell et al. have pointed out the possibility that systolic hypertension in ageing may very well be due to an increase in characteristic impedance not only because of stiffening but also due to decreased aortic diameter (Mitchell 2007; Mitchell, Conlin et al. 2008). Arterial dimensions affect also wave reflections. An increase of reflection coefficient that may occur with age due to mismatch of cross sectional geometries at the thoracic-abdominal location, has been suggested Langewouters et al. based on ex vivo measurements on cadaveric human aortas (Langewouters 1982). Other studies have pointed to changes in aortic dimension with ageing which entrain important changes in the wave reflection intensity and profile (Wilmink, Pleumeekers et al. 1998). The topic is of importance and warrants further investigation.

In summary, the impact of local stiffening of the proximal aorta and global uniform stiffening of the arterial tree was modeled and analyzed by means of a 1-D model of the human systemic circulation. When proximal aorta and global stiffening led to the same reduction in total arterial compliance then the increase in aortic pulse pressure was also similar, however, the mechanisms by which this increase in pulse pressure took place are different. Local proximal aorta stiffening induces an increase in the characteristic impedance and, in consequence, an increase in the amplitude of the forward pressure wave. Global stiffening increased the amplitude and reduced the travel time of the reflected waves, which by arriving back to the ascending aorta in early systole become major contributors to the increase in systolic pressure. We believe that the two mechanisms coexist and their importance in ageing and in presence of different pathologies needs to be carefully addressed in future studies.

ACKNOWLEDGMENTS

This work was supported in part by the European Commission integrated program IST-027703 (@neurIST Project).

CONCLUSION

A 1-D wave propagation model of the systemic arterial tree has been developed and utilized to obtain blood pressure and flow waveforms throughout the vasculature including the distal cerebral arteries. This model was coupled to a model of the left ventricle of the heart.

A generic arterial tree, representative of a group of young healthy volunteers, was built and validated with in vivo non invasive measurements. Flow was visualized with PC-MRI and transcranial Doppler, while superficial arterial pressure measured by applanation tonometry. Qualitative agreement between the in vivo measurements and 1-D model encouraged the development of a patient-specific model based on arterial geometry. This model was validated with non-invasive measurements performed on the same person.

The patient-specific model predicted pressure and flow waveform shape and wave features at systemic circulation locations with a high qualitative and quantitative agreement compared to in vivo measurements. Overall, the 1-D patient-specific model was suitable to predict pressure and flow waves in the entire systemic arterial tree including the cerebral circulation.

On the 1-D patient-specific model we assessed the blood pressure drop from central arteries to the periphery. The results were compared with steady 3-D simulation with rigid walls to evaluate the underestimation of pressure drop in the 1-D model. In the central arteries pressure drop was small and well reproduced by the 1-D model. However in peripheral cerebral arteries losses were more significant and only partially reproduced by the 1-D model. This difference may be substantial in certain applications such as when modeling distal cerebral arterial flow.

To obtain more detailed information on blood flow a 3-D fluid structure interaction simulation was performed for the patient-specific geometry in the proximal aorta and its main branches where atherosclerotic plaque is known to develop. Clinical parameters of importance such as wall shear stress were quantified and significant differences were present compared to a 3-D rigid wall simulation. In terms of pressure and flow waveforms, an equivalent 1-D model showed similar results.

Finally, the impact of local stiffening of the proximal aorta and global uniform stiffening of the arterial tree was analyzed by means of the 1-D model, to help better understand of systolic hypertension. When proximal aorta and global stiffening led to the same reduction in total arterial compliance then the increase in aortic pulse pressure was also similar, however, the mechanisms by which this increase in pulse pressure took place are different. Local proximal aorta stiffening induces an increase in the amplitude of the forward pressure wave. Global stiffening increased the amplitude of the reflected waves. We believe that the two mechanisms coexist and their importance in ageing and in presence of different pathologies needs to be carefully addressed in future studies.

All of the patient-specific models have potential to be used in a clinical environment and could be useful for providing better diagnostic and treatment planning in the near future.

PERSPECTIVES

A number of limitations are present in the current model that can be gradually removed. For instance, the autoregulation phenomenon, in response to hemodynamical stimuli, which is an important issue in cerebral blood flow mechanisms, was not considered and could be included in the future.

The interaction between arterial blood flow and cerebrospinal fluid was only partially taken into account, and seems to play an important role in some cerebral spinal fluid related pathologies.

We considered only the main cerebral collateral circulation, but probably other collateral circulation could be important in certain pathologies.

Small distal vessels such as arterioles, capillaries, venules and veins were not modeled directly and may need to be investigated in detail. Addition of the pulmonary circulation could also “close the circulation loop” and make an even more useful model.

A 1-D model validated for other groups of people or patients could also be useful for research and clinical outcome analysis.

REFERENCES

Aaslid, R., S. R. Lash, et al. (2003). "Dynamic pressure--flow velocity relationships in the human cerebral circulation." Stroke **34**(7): 1645-1649.

Alastruey, J., K. H. Parker, et al. (2007). "Modelling the circle of Willis to assess the effects of anatomical variations and occlusions on cerebral flows." J Biomech **40**(8): 1794-1805.

Avolio, A. P. (1980). "Multi-branched model of the human arterial system." Med Biol Eng Comput **18**(6): 709-718.

Azer, K. and C. S. Peskin (2007). "A One-dimensional Model of Blood Flow in Arteries with Friction and Convection Based on the Womersley Velocity Profile." Cardiovasc Eng.

Baguet, J. P., B. A. Kingwell, et al. (2003). "Analysis of the regional pulse wave velocity by Doppler: methodology and reproducibility." J Hum Hypertens **17**(6): 407-412.

Bergel, D. H. (1961). "The dynamic elastic properties of the arterial wall." J Physiol **156**(3): 458-469.

Bessems, D., M. Rutten, et al. (2007). "A wave propagation model of blood flow in large vessels using an approximate velocity profile function." Journal of Fluid Mechanics **580**: 145-168.

Buijs, P. C., M. J. Krabbe-Hartkamp, et al. (1998). "Effect of age on cerebral blood flow: measurement with ungated two-dimensional phase-contrast MR angiography in 250 adults." Radiology **209**(3): 667-674.

Campbell, K. B., J. A. Ringo, et al. (1982). "Internal capacitance and resistance allow prediction of right ventricle outflow." Am J Physiol **243**(1): H99-112.

Cassot, F., V. Vergeur, et al. (1995). "Effects of anterior communicating artery diameter on cerebral hemodynamics in internal carotid artery disease. A model study." Circulation **92**(10): 3122-3131.

Cassot, F., M. Zagzoule, et al. (2000). "Hemodynamic role of the circle of Willis in stenoses of internal carotid arteries. An analytical solution of a linear model." J Biomech **33**(4): 395-405.

Cebral, J. R., M. A. Castro, et al. (2005). "Efficient pipeline for image-based patient-specific analysis of cerebral aneurysm hemodynamics: technique and sensitivity." IEEE Trans Med Imaging **24**(4): 457-467.

Cebral, J. R., M. A. Castro, et al. (2005). "Characterization of cerebral aneurysms for assessing risk of rupture by using patient-specific computational hemodynamics models." AJNR Am J Neuroradiol **26**(10): 2550-2559.

Chemla, D., J. L. Hebert, et al. (1998). "Total arterial compliance estimated by stroke volume-to-aortic pulse pressure ratio in humans." Am J Physiol **274**(2 Pt 2): H500-505.

Cheng, C., F. Helderman, et al. (2007). "Large variations in absolute wall shear stress levels within one species and between species." Atherosclerosis **195**(2): 225-235.

Cheng, C., D. Tempel, et al. (2006). "Atherosclerotic lesion size and vulnerability are determined by patterns of fluid shear stress." Circulation **113**(23): 2744-2753.

Crosetto, P. "Parallel solvers and preconditioners for fluid-structure interaction problems arising in haemodynamics." Submitted.

Crosetto, P., P. Reymond, et al. (2010). "Fluid Structure Interaction Simulation of Aortic Blood Flow." Computers & Fluids.

DePaola, N., M. A. Gimbrone, Jr., et al. (1992). "Vascular endothelium responds to fluid shear stress gradients." Arterioscler Thromb **12**(11): 1254-1257.

Dodge, J. T., Jr., B. G. Brown, et al. (1992). "Lumen diameter of normal human coronary arteries. Influence of age, sex, anatomic variation, and left ventricular hypertrophy or dilation." Circulation **86**(1): 232-246.

Enzmann, D. R., M. R. Ross, et al. (1994). "Blood flow in major cerebral arteries measured by phase-contrast cine MR." AJNR Am J Neuroradiol **15**(1): 123-129.

Fitchett, D. H. (1991). "LV-arterial coupling: interactive model to predict effect of wave reflections on LV energetics." Am J Physiol **261**(4 Pt 2): H1026-1033.

Ford, M. D., N. Alperin, et al. (2005). "Characterization of volumetric flow rate waveforms in the normal internal carotid and vertebral arteries." Physiol Meas **26**(4): 477-488.

Formaggia, L., J. F. Gerbeau, et al. (2001). "On the coupling of 3D and 1D Navier-Stokes equations for flow problems in compliant vessels." Computer Methods in Applied Mechanics and Engineering **191**(6-7): 561-582.

Formaggia, L., D. Lamponi, et al. (2003). "One-dimensional models for blood flow in arteries." Journal of Engineering Mathematics **47**(3-4): 251-276.

Formaggia, L., D. Lamponi, et al. (2006). "Numerical modeling of 1D arterial networks coupled with a lumped parameters description of the heart." Comput Methods Biomech Biomed Engin **9**(5): 273-288.
Fox, C., M. J. Davies, et al. (1973). "Length of left main coronary artery." Br Heart J **35**(8): 796-798.
Fung, Y. C. (1984). Biodynamics Circulation, Springer.
Gabrielsen, T. O. and T. Greitz (1970). "Normal size of the internal carotid, middle cerebral and anterior cerebral arteries." Acta Radiol Diagn (Stockh) **10**(1): 1-10.
Gambillara, V., G. Montorzi, et al. (2005). "Arterial wall response to ex vivo exposure to oscillatory shear stress." J Vasc Res **42**(6): 535-544.
Gerbeau, J. F. and D. Chapelle (2005). "[Numerical simulation of the cardiovascular system]." Med Sci (Paris) **21**(5): 530-534.
Giller, C. A. and R. Aaslid (1994). "Estimates of pulse wave velocity and measurement of pulse transit time in the human cerebral circulation." Ultrasound Med Biol **20**(2): 101-105.
Grinberg, L., E. Cheever, et al. (2011). "Modeling blood flow circulation in intracranial arterial networks: a comparative 3D/1D simulation study." Ann Biomed Eng **39**(1): 297-309.
Hayashi, K., H. Handa, et al. (1980). "Stiffness and elastic behavior of human intracranial and extracranial arteries." J Biomech **13**(2): 175-184.
Hayashi, K., S. Nagasawa, et al. (1980). "Mechanical properties of human cerebral arteries." Biorheology **17**(3): 211-218.
Hillen, B., H. W. Hoogstraten, et al. (1986). "A mathematical model of the flow in the circle of Willis." J Biomech **19**(3): 187-194.
Holdsworth, D. W., C. J. Norley, et al. (1999). "Characterization of common carotid artery blood-flow waveforms in normal human subjects." Physiol Meas **20**(3): 219-240.
Holenstein, R., P. Niederer, et al. (1980). "A viscoelastic model for use in predicting arterial pulse waves." J Biomech Eng **102**(4): 318-325.
Hughes, T. and J. Lubliner (1973). "On the one-dimensional theory of blood flow in larger vessels." Math. Biosci. **18**: 161-170.
Huo, Y. and G. S. Kassab (2007). "A hybrid one-dimensional/Womersley model of pulsatile blood flow in the entire coronary arterial tree." Am J Physiol Heart Circ Physiol **292**(6): H2623-2633.
Ioannou, C. V., D. R. Morel, et al. (2009). "Left ventricular hypertrophy induced by reduced aortic compliance." J Vasc Res **46**(5): 417-425.
Ioannou, C. V., N. Stergiopulos, et al. (2003). "Hemodynamics induced after acute reduction of proximal thoracic aorta compliance." Eur J Vasc Endovasc Surg **26**(2): 195-204.
Jegger, D., A. S. Mallik, et al. (2007). "The effect of a myocardial infarction on the normalized time-varying elastance curve." J Appl Physiol **102**(3): 1123-1129.
Kelly, R., C. Hayward, et al. (1989). "Noninvasive determination of age-related changes in the human arterial pulse." Circulation **80**(6): 1652-1659.
Kim, H. J., I. E. Vignon-Clementel, et al. (2009). "On Coupling a Lumped Parameter Heart Model and a Three-Dimensional Finite Element Aorta Model." Annals of Biomedical Engineering **37**(11): 2153-2169.
Krabbe-Hartkamp, M. J., J. van der Grond, et al. (1998). "Circle of Willis: morphologic variation on three-dimensional time-of-flight MR angiograms." Radiology **207**(1): 103-111.
Krams, R., P. Sipkema, et al. (1989). "Varying elastance concept may explain coronary systolic flow impediment." Am J Physiol **257**(5 Pt 2): H1471-1479.
Krayenbuehl and Yasargil (1982). Cerebral Angiography, Thieme Medical Publishers.
Kufahl, R. H. and M. E. Clark (1985). "A circle of Willis simulation using distensible vessels and pulsatile flow." J Biomech Eng **107**(2): 112-122.
Langewouters, G. J. (1982). Visco-elasticity of the human aorta in vitro in relation to pressure and age**:** 221.
Latham, R. D., N. Westerhof, et al. (1985). "Regional wave travel and reflections along the human aorta: a study with six simultaneous micromanometric pressures." Circulation **72**(6): 1257-1269.
Leguy, C. A., E. M. Bosboom, et al. (2010). "Estimation of distributed arterial mechanical properties using a wave propagation model in a reverse way." Med Eng Phys **32**(9): 957-967.
Luchsinger, P. C., R. E. Snell, et al. (1964). "Instanteous Pressure Distribution Along the Human Aorta." Circ Res **15**: 503-510.
Marshall, I., P. Papathanasopoulou, et al. (2004). "Carotid flow rates and flow division at the bifurcation in healthy volunteers." Physiol Meas **25**(3): 691-697.
Marzo, A., P. Singh, et al. (2011). "Computational hemodynamics in cerebral aneurysms: the effects of modeled versus measured boundary conditions." Ann Biomed Eng **39**(2): 884-896.

Matthys, K. S., J. Alastruey, et al. (2007). "Pulse wave propagation in a model human arterial network: assessment of 1-D numerical simulations against in vitro measurements." J Biomech **40**(15): 3476-3486.

McDonald, D. A., W. W. Nichols, et al. (1990). Blood Flow in Arteries, Edward Arnold.

Meister, J.-J. (1983). Mesure par échographie Doppler et modélisation théorique de l'effet de troubles cardiaques sur la pression et le débit artériels. Lausanne.

Merenda, F. (2003). Varying elastance model coupled to a distributed model of the human arterial tree, EPFL.

Mitchell, G. F. (2007). "Impedance progress: aortic diameter rears its head again?" Hypertension **49**(6): 1207-1209.

Mitchell, G. F., P. R. Conlin, et al. (2008). "Aortic diameter, wall stiffness, and wave reflection in systolic hypertension." Hypertension **51**(1): 105-111.

Murgo, J. P., N. Westerhof, et al. (1980). "Aortic input impedance in normal man: relationship to pressure wave forms." Circulation **62**(1): 105-116.

Nichols, W. W., M. F. O'Rourke, et al. (1985). "Effects of age on ventricular-vascular coupling." Am J Cardiol **55**(9): 1179-1184.

Nobile, F. and C. Vergara (2007). "An effective fluid-structure interaction formulation for vascular dynamics by generalized Robin conditions." Siam Journal on Scientific Computing **30**(2): 731-763.

Noordergraaf, A. (1956). Physical basis of ballistocardiography. s'Gravenhage, Excelsior**:** 146.

Noordergraaf, A., D. Verdouw, et al. (1963). "The use of an analog computer in a circulation model." Prog Cardiovasc Dis **5**: 419-439.

O'Rourke, M. F. and W. W. Nichols (2005). "Aortic diameter, aortic stiffness, and wave reflection increase with age and isolated systolic hypertension." Hypertension **45**(4): 652-658.

Obata, T., F. Shishido, et al. (1996). "Three-vessel study of cerebral blood flow using phase-contrast magnetic resonance imaging: effect of physical characteristics." Magn Reson Imaging **14**(10): 1143-1148.

Olufsen, M. S. (1999). "Structured tree outflow condition for blood flow in larger systemic arteries." Am J Physiol **276**(1 Pt 2): H257-268.

Olufsen, M. S., C. S. Peskin, et al. (2000). "Numerical simulation and experimental validation of blood flow in arteries with structured-tree outflow conditions." Ann Biomed Eng **28**(11): 1281-1299.

Papageorgiou, G. L., B. N. Jones, et al. (1990). "The areas ratio of normal arterial junctions and its implications in pulse wave reflections." Cardiovasc Res **24**(6): 478-484.

Papapanayotou, C. J., Y. Cherruault, et al. (1990). "A Mathematical-Model of the Circle of Willis in the Presence of an Arteriovenous Anomaly." Computers & Mathematics with Applications **20**(4-6): 199-206.

Pennell, D. J., J. Keegan, et al. (1993). "Magnetic resonance imaging of coronary arteries: technique and preliminary results." Br Heart J **70**(4): 315-326.

Perktold, K. and G. Rappitsch (1995). "Computer simulation of local blood flow and vessel mechanics in a compliant carotid artery bifurcation model." J Biomech **28**(7): 845-856.

Quarteroni, A., L. Formaggia, et al. (2009). Cardiovascular Mathematics Modeling and simulation of the circulatory system. Milan, Springer.

Radaelli, A. G., L. Augsburger, et al. (2008). "Reproducibility of haemodynamical simulations in a subject-specific stented aneurysm model--a report on the Virtual Intracranial Stenting Challenge 2007." J Biomech **41**(10): 2069-2081.

Radaelli, A. G., L. Augsburger, et al. (2008). "Reproducibility of haemodynamical simulations in a subject-specific stented aneurysm model-A report on the Virtual Intracranial Stenting Challenge 2007." J Biomech **41**(10): 2069-2081.

Raines, J. K., M. Y. Jaffrin, et al. (1974). "A computer simulation of arterial dynamics in the human leg." J Biomech **7**(1): 77-91.

Randall, O. S., G. C. van den Bos, et al. (1984). "Systemic compliance: does it play a role in the genesis of essential hypertension?" Cardiovasc Res **18**(8): 455-462.

Reymond, P., Y. Bohraus, et al. (2011). "Validation of a patient-specific 1-D model of the systemic arterial tree." Submitted to AJP.

Reymond, P., Y. Bohraus, et al. (2011). "VALIDATION OF A PATIENT-SPECIFIC 1-D MODEL OF THE SYSTEMIC ARTERIAL TREE." AJP Submitted.

Reymond, P., F. Merenda, et al. (2009). "Validation of a one-dimensional model of the systemic arterial tree." Am J Physiol Heart Circ Physiol **297**(1): H208-222.

Rogers, P. A., T. Kiyooka, et al. (2006). "Is there a need for another model on the pulsatile nature of coronary blood flow?" Am J Physiol Heart Circ Physiol **291**(3): H1034-1035.

Sagawa, K. (1988). Cardiac contraction and the pressure-volume relationship. New York ; Oxford, Oxford University Press.
Schaaf, B. W. and P. H. Abbrecht (1972). "Digital computer simulation of human systemic arterial pulse wave transmission: a nonlinear model." J Biomech **5**(4): 345-364.
Scheel, P., C. Ruge, et al. (2000). "Color duplex measurement of cerebral blood flow volume in healthy adults." Stroke **31**(1): 147-150.
Segers, P., E. Rietzschel, et al. (2005). "Carotid tonometry versus synthesized aorta pressure waves for the estimation of central systolic blood pressure and augmentation index." Am J Hypertens **18**(9 Pt 1): 1168-1173.
Segers, P., N. Stergiopulos, et al. (1997). "Assessment of distributed arterial network models." Med Biol Eng Comput **35**(6): 729-736.
Senzaki, H., C. H. Chen, et al. (1996). "Single-beat estimation of end-systolic pressure-volume relation in humans. A new method with the potential for noninvasive application." Circulation **94**(10): 2497-2506.
Sherwin, S. J., V. Franke, et al. (2003). "One-dimensional modelling of a vascular network in space-time variables." Journal of Engineering Mathematics **47**(3-4): 217-250.
Shroff, S. G., J. S. Janicki, et al. (1985). "Evidence and quantitation of left ventricular systolic resistance." Am J Physiol **249**(2 Pt 2): H358-370.
Spilt, A., F. M. Box, et al. (2002). "Reproducibility of total cerebral blood flow measurements using phase contrast magnetic resonance imaging." J Magn Reson Imaging **16**(1): 1-5.
Starling, M. R., R. A. Walsh, et al. (1987). "The relationship of various measures of end-systole to left ventricular maximum time-varying elastance in man." Circulation **76**(1): 32-43.
Steinman, D. A. (2002). "Image-based computational fluid dynamics modeling in realistic arterial geometries." Ann Biomed Eng **30**(4): 483-497.
Stergiopulos, N., J. J. Meister, et al. (1994). "Simple and accurate way for estimating total and segmental arterial compliance: the pulse pressure method." Ann Biomed Eng **22**(4): 392-397.
Stergiopulos, N., J. J. Meister, et al. (1995). "Evaluation of methods for estimation of total arterial compliance." Am J Physiol **268**(4 Pt 2): H1540-1548.
Stergiopulos, N., J. J. Meister, et al. (1995). "Scatter in input impedance spectrum may result from the elastic nonlinearity of the arterial wall." Am J Physiol **269**(4 Pt 2): H1490-1495.
Stergiopulos, N., P. Segers, et al. (1999). "Use of pulse pressure method for estimating total arterial compliance in vivo." Am J Physiol **276**(2 Pt 2): H424-428.
Stergiopulos, N., B. E. Westerhof, et al. (1998). "Physical basis of pressure transfer from periphery to aorta: a model-based study." Am J Physiol **274**(4 Pt 2): H1386-1392.
Stergiopulos, N. and N. Westerhof (1998). "Determinants of pulse pressure." Hypertension **32**(3): 556-559.
Stergiopulos, N., D. F. Young, et al. (1992). "Computer simulation of arterial flow with applications to arterial and aortic stenoses." J Biomech **25**(12): 1477-1488.
Stettler, J. C., P. Niederer, et al. (1981). "Theoretical analysis of arterial hemodynamics including the influence of bifurcations. Part I: mathematical models and prediction of normal pulse patterns." Ann Biomed Eng **9**(2): 145-164.
Stettler, J. C., P. Niederer, et al. (1981). "Theoretical analysis of arterial hemodynamics including the influence of bifurcations. Part II: critical evaluation of theoretical model and comparison with noninvasive measurements of flow patterns in normal and pathological cases." Ann Biomed Eng **9**(2): 165-175.
Stock, K. W., S. G. Wetzel, et al. (2000). "Quantification of blood flow in the middle cerebral artery with phase-contrast MR imaging." Eur Radiol **10**(11): 1795-1800.
Taylor, C. A. and C. A. Figueroa (2009). "Patient-Specific Modeling of Cardiovascular Mechanics." Annu. Rev. Biomed. Eng. **11**: 109–134.
Taylor, C. A., T. J. R. Hughes, et al. (1998). "Finite element modeling of blood flow in arteries." Computer Methods in Applied Mechanics and Engineering **158**(1-2): 155-196.
Torii, R., M. Oshima, et al. (2007). "Influence of wall elasticity in patient-specific hemodynamic simulations." Computers & Fluids **36**(1): 160-168.
Trachet, B., P. Reymond, et al. (2010). "Numerical validation of a new method to assess aortic pulse wave velocity from a single recording of a brachial artery waveform with an occluding cuff." Ann Biomed Eng **38**(3): 876-888.
van de Vosse, F. N. and N. Stergiopulos (2011). "PulseWave Propagation in the Arterial Tree." Annu. Rev. Fluid Mech. **43**: 467–499.
Vasan, R. S. (2008). "Pathogenesis of elevated peripheral pulse pressure: some reflections and thinking forward." Hypertension **51**(1): 33-36.

Vis, M. A., P. Sipkema, et al. (1995). "Modeling pressure-area relations of coronary blood vessels embedded in cardiac muscle in diastole and systole." Am J Physiol **268**(6 Pt 2): H2531-2543.
Wan, J., B. Steele, et al. (2002). "A one-dimensional finite element method for simulation-based medical planning for cardiovascular disease." Comput Methods Biomech Biomed Engin **5**(3): 195-206.
Wemple, R. R. and L. F. Mockros (1972). "Pressure and flow in the systemic arterial system." J Biomech **5**(6): 629-641.
Westerhof, B. E., I. Guelen, et al. (2007). "Arterial pressure transfer characteristics: effects of travel time." Am J Physiol Heart Circ Physiol **292**(2): H800-807.
Westerhof, B. E., J. P. van den Wijngaard, et al. (2008). "Location of a reflection site is elusive: consequences for the calculation of aortic pulse wave velocity." Hypertension **52**(3): 478-483.
Westerhof, N., F. Bosman, et al. (1969). "Analog studies of the human systemic arterial tree." J Biomech **2**(2): 121-143.
Westerhof, N., P. Sipkema, et al. (1972). "Forward and backward waves in the arterial system." Cardiovasc Res **6**(6): 648-656.
Westerhof, N. and N. Stergiopulos (2000). "Models of the arterial tree." Stud Health Technol Inform **71**: 65-77.
White, C. R., M. Haidekker, et al. (2001). "Temporal gradients in shear, but not spatial gradients, stimulate endothelial cell proliferation." Circulation **103**(20): 2508-2513.
Wilmink, A. B., H. J. Pleumeekers, et al. (1998). "The infrarenal aortic diameter in relation to age: only part of the population in older age groups shows an increase." Eur J Vasc Endovasc Surg **16**(5): 431-437.
Witzig, K. (1914). Über erzwungene Wellenbewegungen zäher, inkommpressibler Flüssigkeiten in elastischen Röhren. Bern.
Womersley, J. R. (1955). "Method for the calculation of velocity, rate of flow and viscous drag in arteries when the pressure gradient is known." J Physiol **127**(3): 553-563.
Yasargil (1984). Microneurosurgery. Microsurgical anatomy of the basal cisterns and vessels of the brain, diagnostic studies, general operative techniques and pathological considerations of the intracranial aneurysms.
, Thieme Medical Publishers.
Yasargil, K. (1982). Cerebral Angiography.
Zagzoule, M. and J. P. Marc-Vergnes (1986). "A global mathematical model of the cerebral circulation in man." J Biomech **19**(12): 1015-1022.

PUBLICATIONS

- Crosetto P, Reymond P, Deparis S, Kontaxakis D, Stergiopulos N, Quarteroni A. Fluid Structure Interaction Simulation of Aortic Blood Flow. Computers & Fluids. 2010

- Augsburger L, Reymond P, Rufenacht DA, Stergiopulos N. Intracranial Stents Being Modeled as a Porous Medium: Flow Simulation in Stented Cerebral Aneurysms. Ann Biomed Eng. 2010 Nov

- Marzo A, Singh P, Larrabide I, Radaelli A, Coley S, Gwilliam M, Wilkinson I.D, Lawford P, Reymond P, Patel U, Frangi A, Hose R. Computational Haemodynamics in Cerebral Aneurysms: the Effects of Modelled versus Measured Boundary Conditions. Annals of Biomedical Engineering. 2010-11

- Trachet B, Reymond P, Kips J, Swillens A, De Buyzere M, Suys B, Stergiopulos N and Segers P. Numerical Validation of a New Method to Assess Aortic Pulse Wave Velocity from a Single Recording of a Brachial Artery Waveform with an Occluding Cuff. Ann Biomed Eng. 2010

- Augsburger L, Farhat M, Reymond P, Fonck E, Kulcsar Z, Stergiopulos N, Rüfenacht DA. Effect of flow diverter porosity on intraaneurysmal blood flow. Klin Neuroradiol. 2009

- Reymond P, Merenda F, Perren F, Rüfenacht DA and Stergiopulos N. Validation of a one-dimensional model of the systemic arterial tree. Am J Physiol Heart Circ Physiol. 2009

- Marzo A, Singh P, Reymond P, Stergiopulos N and Hose R. Influence of inlet boundary conditions on the local haemodynamics of intracranial aneurysms. Comput Methods Biomech Biomed Engin. 2009

- Augsburger L., Reymond P, Fonck E, Kulcsar Z, Farhat M, Ohta M, Stergiopulos N, Rüfenacht DA. Methodologies to assess blood flow in cerebral aneurysms: Current state of research and perspectives. J Neuroradiol. 2009

- Radaelli AG, Augsburger L, Cebral JR, Ohta M, Rüfenacht DA, Balossino R, Benndorf G, Hose DR, Marzo A, Metcalfe R, Mortier P, Mut F, Reymond P, Socci L, Verhegghe B, Frangi AF. Reproducibility of haemodynamical simulations in subject-specific stented aneurysm model. A report on the Virtual Intracranial Stenting Challenge 2007. J Biomech. 2008

- Augsburger L, Reymond P, Farhat M, Fonck E, Rufenacht DA, Stergiopulos N. Particle Image Velocimetry and numerical simulation: a first step to validation simulating flow in idealized models of cerebral aneurysms, Neuroradiology, 2006

CONFERENCES

2010 - Talks

- Reymond P, Bohraus Y, Perren F, Lazeyras F and Stergiopulos N. Validation of a Person Specific 1-D Model of the Systemic Arterial Tree. The XII Mediterranean Conference on Medical and Biological Engineering and Computing, Greece

- Reymond P, Bohraus Y, Perren F, Lazeyras F and Stergiopulos N. Validation of a Person Specific 1D Model of the Systemic Arterial Tree. IV International Symposium on Modeling of Physiological Flows, Sardinia, Italy

- Trachet B, Kips J, Reymond P, Swillens A, De Buyzere M, Suys B, Stergiopulos N, Segers P. ESH: Title: The Arteriograph: measuring axillo-brachial rather than aortic stiffness?, 6th World Congress of Biomechanics, Singapore

- Augsburger L, Rochette M, Penrose J, Jones I, Ouared R, Reymond P, Marchal T, Horner M, Rüfenacht DA. Abstract for FDA & NHLBI Third annual workshop on cardiovascular device modeling: The integration of nonclinical and computer models. The added-value brought by CFD in the management of Cerebral Aneurysms. USA

- (EUROMECH 518 Workshop)

- Reymond P, Bohraus Y, Perren F, Lazeyras F, Stergiopulos N. Validation of a Person Specific 1-D Model of the Systemic Arterial Tree. 6th World Congress of Biomechanics, Singapore

- Martin B, Reymond P, Loth F, Stergiopulos N. A 1-D Coupled Hydrodynamic Model of the Cardiovascular Tree and Cerebrospinal Fluid System. 6th World Congress of Biomechanics, Singapore

Posters

- B Trachet, P Reymond, J Kips, A Swillens, M De Buyzere, B Suys, N Stergiopulos, P Segers. The arteriograph: correlated to aortic stiffness, but measuring axillo-brachial artery stiffness? Artery, Verona, Italy

- Reymond P, Bohraus Y, Perren F, Lazeyras F, Rüfenacht D, Stergiopulos N. Validation of a Person Specific 1-D Model of the Systemic Arterial Tree. CSDS 19th International Conference of the Cardiovascular System Dynamics Society, Fukuoka, Japan

- Reymond P, Bohraus Y, Perren F, Lazeyras F, Stergiopulos N. Validation of a Person Specific 1-D Model of the Systemic Arterial Tree. EPFL SV- Life Science Symposium, Lausanne, Switzerland

2009 - Talks

- Reymond P, Bohraus Y, Perren F, Lazeyras F and Stergiopulos N. Validation of a person specific 1D model of the systemic arterial tree, 3rd International Meeting of the French Society of Hypertension, Paris, France

- Reymond P, Bohraus Y, Perren F, Rüfenacht DA and Stergiopulos N. Validation of a Person Specific 1D Model of the Systemic Arterial Tree. Bioengineering, Oxford, UK

- Vardoulis O, Kontaxakis D, Roy S, Reymond P, Stergiopoulos N. Simulation of the outflow pathway in the human eye, World Congress on Medical Physics and Biomedical Engineering, Münich, Germany

- Reymond P, Bohraus Y, Perren F and Stergiopulos N. Validation of a Person Specific 1D Model of the Systemic Arterial Tree SJB, Engelberg

- Reymond P, Bohraus Y, Perren F, Augsburger L, Rüfenacht DA and Stergiopulos N. Validation of a person specific 1D model of the systemic arterial tree. 6th Intracranial Stent Meeting, Sendai, Japan

- Augsburger L, Reymond P, Ouared R, Brina O, Mendes Pereira V, Stergiopulos N, Rüfenacht DA. Influence of segementation on aneurysm morphology and intracranial aneurysms flow patterns.6th Intracranial Stent Meeting, Sendai, Japan

- Augsburger L, Reymond P, Rüfenacht DA, Stergiopulos N. 6th intracranial stent meeting VISC'09 Session "the 3rd Virtual Intracranial Stenting Challenge", Sendai, Japan

- Reymond P, Bohraus Y, Perren F, Rüfenacht DA and Stergiopulos N. Validation of a person specific 1D model of the systemic arterial tree. ECCOMAS and IACM Special Interest Conference "2nd South-East European Conference on Computational Mechanics (SEECCM)", Rhodes, Greece

- Reymond P, Bohraus Y, Perren F and Stergiopulos N. Validation of a person specific 1D model of the systemic arterial tree. Summer Bioengineering Conference, Lake Tahoe, California, USA

- Reymond P, Perren F, Rüfenacht DA and Stergiopulos N. Validation of a one dimensional model of the arterial cerebral circulation using ultrasound. AAN 61st annual meeting of the American Academy of Neurology, Seattle, USA

Posters
- Vardoulis O, Kontaxakis D, Roy S, Reymond P, Stergiopoulos N. Simulation of the fibrosis effect after a sub-scleral glaucoma drainage device implantation, SJB, Engelberg

2008 – Talks
- BMES 08 Biomedical Engineering Society

- CSDS 08 Cardiovascular System Dynamics Society

- Reymond P, Merenda F, Perren F, Rüfenacht DA and Stergiopulos N. Validation of a 1D Model of the Systemic Arterial Tree Including the Cerebral Circulation. MBEC, 4th European Congress of the International Federation for Medical and Biological Engineering, Antwerp

- Reymond P, Merenda F, Perren F, Rüfenacht DA and Stergiopulos N. Validation of a 1D Model of the Systemic Arterial Tree Including the Cerebral Circulation. Imperial College, bioengineering conference 08, London, UK

- Reymond P, Merenda F, Perren F, Rüfenacht DA and Stergiopulos N. Validation Of 1D Model Of The Systemic Arterial Tree Including The Cerebral Circulation. Summer Bioengineering Conference, Marco Island, Florida, USA

- Reymond P, Merenda F, Perren F, Rüfenacht DA and Stergiopulos N. Validation of a one-dimensional model of the arterial cerebral circulation. 6th European Symposium on Biomedical Engineering, Chania, Crete Island, Greece

- Reymond P, Perren F, Rüfenacht DA and Stergiopulos N. Validation of a one-dimensional model of the arterial cerebral circulation. 13th Meeting of the European Society of Neurosonology and Cerebral Hemodynamics ESNCH, Genova, Italy

- Reymond P, Merenda F, Perren F, Rüfenacht DA and Stergiopulos N. Validation of 1D model of the systemic arterial tree including the cerebral circulation. 16th Congress of the European Society of Biomechanics, Luzern

- Augsburger L, Farhat M, Reymond P, Fonck E, Stergiopulos N, Rufenacht DA. Effects of flow diverter's porosity on intra-aneurysmal blood flow in cerebral aneurysm silicone models using particle image velocimetry. 5th intracranial stent meeting, Ankara, Turkey

Posters
- Reymond P, Perren F, Rüfenacht DA and Stergiopulos N. Validation of a one-dimensional model of the arterial cerebral circulation. Centenary of the Swiss Society of Neurology, Neurosurgery and Neuroradiology, Montreux

- Reymond P, Merenda F, Perren F, Rüfenacht DA and Stergiopulos N. Validation of 1D model of the systemic arterial tree including the cerebral circulation. Union of the Swiss Societies for Experimental Biology USGEB, Annual Conference, Lausanne

2007 - Talks

- Reymond P, Merenda F, Perren F, Rüfenacht DA and Stergiopulos N. One dimensional model of the systemic Arterial Tree including Cerebral Circulation. 4th Intracranial Stent Meeting, Kyoto, Japan

- Augsburger L, Reymond P, Fonck EE, Farhat M, Rüfenacht DA, Stergiopulos N. Assessment of blood flow changes due to the insertion of a stent in cerebral aneurysm silicone replicas using Particle Image Velocimetry (PIV). SSBE, Swiss Society for Biomedical Engineering, Neuchâtel

-Augsburger L, Reymond P, Fonck EE, Farhat M, Rüfenacht DA, Stergiopulos N. Assessment of blood flow changes due to the insertion of a stent in cerebral aneurysm silicone replicas using Particle Image Velocimetry (PIV)" BMES, Biomedical Engineering Society, Lausanne

- Augsburger L, Fonck EE, Reymond P, Ohta M, Rüfenacht DA, Stergiopulos N. Research presentation for William COOK Europe, "Methodologies developed for the assessment of hemodynamical changes due to the insertion of a stent in cerebral aneurysms", Copenhagen

- Augsburger L, Fonck EE, Reymond P, Ohta M, Rüfenacht DA, Stergiopulos N. Assessment of Blood Flow in Idealized Cerebral Aneurysms Replicas using Particle Image Velocimetry in presence of an endovascular device. ICS07, 4th Intracranial Stent meeting, Kyoto, Japan

- Augsburger L, Long J, Fonck EE, Reymond P, Rüfenacht DA, Stergiopulos N. Assessment of Flow in Cerebral Aneurysms Silicone Models using Particle Image Velocimetry (PIV)", WIFTN, World Federation of Interventional and Therapeutic Neuroradiology, Beijing, China

Posters

- Reymond P, Merenda F, Perren F, Rüfenacht DA and Stergiopulos N. One dimensional model of the systemic Arterial Tree including Cerebral Circulation. Summer Bioengineering Conference, Keystone, CO, USA

2006 - Talks

- Reymond P, Merenda F, Augsburger L and Stergiopulos N. 1-D model of the Arterial Tree including detailed description of Cerebral Circulation. 3rd Intracranial Stent Meeting, Geneva

- Augsburger L, Reymond P, Farhat M, Fonck E, Rüfenacht D, Stergiopulos N. Particle image velocimetry and numerical simulation: a first step to validation simulating flow in idealized models of cerebral aneurysms. 3rd Intracranial Stent Meeting, Geneva

- Augsburger L, Reymond P, Farhat M, Fonck E, Rüfenacht D, Stergiopulos N. Particle Image Velocimetry and Numerical Simulation: A first step to validation simulating flow in idealized models of cerebral aneurysms. 5th World Congress of Biomechanics, Munich

- Augsburger L, Reymond P, Fonck E, Ohta M, Rufenacht DA, Stergiopulos N. Particle Image Velocimetry and Numerical Simulation: A first step to validation simulating flow in idealized models of cerebral aneurysms. ESNR06/ICS06, 3rd Intracranial Stent meeting, Geneva

CURRICULUM VITAE

Philippe REYMOND
Swiss, August 23th, 1979
philippe.reymond@a3.epfl.ch

1242 Satigny
Geneva
Switzerland

PhD student in Life Science EPFL
Master in Science EPFL
DEA SUPAERO (F)
Engineer SUPAERO (F)
Engineer EIG

EDUCATIONAL

2005-2011 PhD student in **Life Science** EPFL
In-vivo development and validation of a 1-D model of the systemic circulation
Laboratory of Hemodynamics and Cardiovascular Technology
Doctoral school of Biotechnology and Bioengineering
Done in the frame of the @neurIST EU Project *(6th Framework Programme)* IST-027703

2002-2004 Diploma of SUPAERO, Toulouse, -The French Engineering School of Aeronautics and Space- Field option in aircrafts design and aerodynamic. Admitted based on record.

2003-2004 Diplôme d'études approfondies en génie mécanique, SUPAERO. Done in parallel.

1999-2002 Master from **Ecole Polytechnique Fédérale de Lausanne** -EPFL- in mechanical engineering and parallel diploma at SUPAERO

1994-1999 Diploma from **Ecole d'Ingénieurs de Genève** -EIG- in mechanical engineering. Diploma subject: design of an electrical brachial orthese for person suffering from myopathy

PROFESSIONAL EXPERICENCE AND PROJECTS

2005- Co-supervision of 7 Master projects *(6-10 months)* and 5 semester projects at EPFL
Teaching assistant for cardiovascular biomechanics class *(Master 4th yr EPFL, 30 students)* and fluid mechanics *(Ba 3rd yr EPFL, 60 students)*

2007- Ski design and build in our workshop
6 EPFL students have performed dynamic mechanical testing and characterization of our skis during their semester project in order to improve them.

2003 Student campaign of parabolic flights in Bordeaux under the supervision of ESA (European Space Agency). Design and build of the experiment.

2003 2nd year project at ONERA -French Aerospace Lab- in Toulouse.
Flight mechanic field: optimization of a human propulsion aircraft

2002 Assistant in thermodynamics course in 2nd year at EPFL *(60 students, 1 yr)*

2000 Development of brachial orthese designed in 1999 at l'EIG *(2 months)*

LANGUAGES

French	mother-tongue
English	B2-C1 level
German	A2 level

COMPUTER LANGUAGES

Systems	Windows, UNIX, Linux
Languages	Matlab, C, Fortran, Java, Tex
CAE software	Fluent, Ansys, CFX, Abaqus, ProEngineer, Catia, I-Deas, MS-Office

HOBBIES

Aircraft Private Pilot License PPL(A)

Ski, downhill bike, football, mountaineering

AWARDS

Clinical Neuroradiology journal: best original publication in 2009 for the article «Effect of flow diverter porosity on intraaneurysmal blood flow. Klin Neuroradiol. 2009»

Diplomas from EIG 1999: design of an electrical brachial orthese for person suffering from myopathy
- Congratulations from the jury
- Prix de l'association des anciens élèves des écoles d'ingénieurs de Genève (ATG)
- EIG award
- Institut BATTELLE de Genève award

SOCIETY

Member of the American Society of Physiology (APS) and Biomedical Engineering Society (BMES)